CZECH TECHNICAL UNIVERSITY IN PRAGUE
Faculty of Biomedical Engineering
Department of Natural Sciences

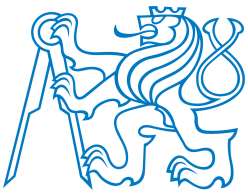

LABORATORY WATER-WINDOW MICROSCOPE BASED ON Z-PINCHING CAPILLARY DISCHARGE SOURCE FOR BIOLOGICAL IMAGING

Doctoral thesis

TOMÁŠ PARKMAN

Ph.D. Programme: Biomedical and Clinical Technology
Thesis Supervisor: Prof. Ing. Miroslava Vrbová, CSc.

Kladno, February 2021

Thesis Supervisor:

Prof. Ing. Miroslava Vrbová, CSc.

Czech Technical University in Prague
Faculty of Biomedical Engineering
Nám. Sítná 3105
272 01 Kladno
Czech Republic

Thesis Co-Supervisors:

Ing. Alexandr Jančárek, CSc.

Czech Technical University in Prague
Faculty of Nuclear Sciences and Physical Engineering
Břehova 7
115 19 Prague 1
Czech Republic

Ing. Dalibor Pánek, Ph.D.

Czech Technical University in Prague
Faculty of Biomedical Engineering
Nám. Sítná 3105
272 01 Kladno
Czech Republic

Declaration

I declare that I carried out this doctoral thesis independently, and only with the cited sources, literature and other professional sources.
I understand that my work relates to the rights and obligations under the Act No. 121/2000 Coll., the Copyright Act, as amended, in particular the fact that the Czech Technical University in Prague has the right to conclude a license agreement on the use of this work as a school work pursuant to Section 60 paragraph 1 of the Copyright Act.

Signed:

Date:

Abstract

Soft X-ray microscopy in the water-window spectral region (2.28–4.36 nm) is one of the emerging biological imaging methods with the resolution in the order of tens nanometers covering the gap between transmission electron microscopy and visible light microscopy, and providing a tool to image an intact cell in a native or near-native environment. However, soft X-ray microscopes are commonly based on large-scale facilities such as synchrotron or free-electron lasers, limiting the accessibility to this imaging technique for the broader scientific community.

In the first section this Thesis describes comparison of two table-top sources of soft X-ray radiation – laser- and discharge-produced plasma, with regards to imaging in the water-window region. The laser-produced plasma source was developed in Laser-Laboratorium Göttingen e.V., Germany, and plasma is induced by a laser pulse of Q-switched Nd:YAG laser (1064 nm, 640 mJ, 7 ns pulse) focused into nitrogen gas-puff target. The discharge-produced plasma source was developed in-house at Czech Technical University in Prague, and plasma is generated by a current discharge through the ceramic capillary filled with nitrogen gas. Both sources utilize the nitrogen spectral line $\lambda = 2.88$ nm (430 eV), corresponding to the quantum transition $1s^2$–1s2p of helium-like nitrogen ions. The discharge-produced nitrogen plasma source has a higher brightness; therefore, it was used for the microscope development. In its second section the Thesis presents a design and performance of a compact transmission water-window microscope based on the Z-pinching capillary discharge nitrogen plasma source. The emitted soft X-ray radiation is filtered by a titanium foil and focused by an ellipsoidal condenser mirror into the sample plane. A Fresnel zone plate was used to create a transmission image of the sample onto a CCD camera. To assess the resolution of the microscope, a standard sample—copper mesh—was imaged. The spatial resolution of the microscope is 75 nm at half-pitch, calculated via a 10–90% intensity knife-edge test. The applicability of the microscope is demonstrated by the imaging of green algae–*Desmodesmus communis*.

Keywords:

Soft X-ray microscopy, water-window, laser- and discharge-produced plasma source, gas-puff target, Z-pinch, 2.88 nm, Fresnel zone plate, ellipsoidal condenser mirror, *Desmodesmus communis*.

Abstrakt

Měkká rentgenová mikroskopie ve spektrální oblasti tzv. vodního okna (2,28–4,36 nm) je rozvíjející se zobrazovací metoda pro zkoumání biologických objektů. Díky svému prostorovému rozlišení v řádu desítek nanometrů jde o komplementární zobrazovací metodu k transmisní elektronové mikroskopii a optické mikroskopii, která umožňuje zobrazení celistvých buněk v jejich přirozeném prostředí. Nejčastějšími zdroji záření pro měkkou rentgenovou mikroskopii jsou rozlehlá a nákladná zařízení, jakými jsou synchrotrony a lasery na volných elektronech, což omezuje přístup širší vědecké veřejnosti k této zobrazovací metodě.

Tato doktorská práce ve své první části popisuje srovnání dvou laboratorních zdrojů měkkého rentgenového záření – laserem a výbojem generované plazma. Oba zdroje jsou charakterizovány jako potenciální zdroje záření pro měkkou rentgenovou mikroskopii ve vodním okně. Laserem generovaný plazmatický zdroj záření byl vyvinut v Laser-Laboratorium Göttingen e.V., Německo; plazma je zde indukováno laserovým pulzem Q-spínaného Nd:YAG laseru (1064 nm, 640 mJ, 7 ns) fokusovaného do dusíkového plynného terče. Výbojem generovaný plazmatický zdroj byl vyvinut na Českém vysokém učení technickém v Praze; plazma je zde generováno proudovým výbojem procházejícím dusíkem plněnou kapilárou. Oba zdroje záření využívají spektrální čáru dusíku $\lambda = 2{,}88$ nm (430 eV) odpovídající kvantovému přechodu $1s^2$–1s2p heliu podobných dusíkových iontů. Vývoj samotného mikroskopu využívající měkké rentgenové záření byl založen na výbojovém zdroji z důvodu jeho vyššího jasu. Ve své druhé části doktorská práce prezentuje uspořádání a praktické využití transmisního mikroskopu operujícího ve vodním okně, který je založen na Z-pinčujícím kapilárním výbojovém zdroji dusíkového plazmatu. Emitované měkké rentgenové záření je filtrováno titanovou folií a fokusováno eliptickým kondenzorem do roviny vzorku. K vytvoření transmisního obrazu vzorku na CCD kameru byla využita Fresnelova čočka (zónová deska). Jako standardní vzorek pro určení rozlišení mikroskopu byla zobrazena periodická měděná mřížka. Výsledná prostorová rozlišovací schopnost mikroskopu je 75 nm. Ta byla určena z obrazu měděné mřížky pomocí standardního 10–90% intenzitního testu. Potenciál mikroskopu je demonstrován zobrazením zelené řasy – *Desmodesmus communis*.

Klíčová slova:

Měkká rentgenová mikroskopie, vodní okno, laserem a výbojem generované plazma, plynný terč, Z-pinč, 2,88 nm, Fresnelova čočka, eliptický kondenzor, *Desmodesmus communis*.

Acknowledgements

This Thesis is a result of my doctoral studies at the Faculty of Biomedical Engineering at Czech Technical University in Prague. However, the work would not have been possible without the help, guidance, and support of many colleagues and friends, whom I had the luck to meet and work with during my studies. I would like to express my gratitude to all of them.

My greatest and most sincere gratitude belongs to my supervisor Miroslava Vrbová for her guidance, willingness, and patience. She always tried to support me professionally and personally, making her best to help me with funding and to overcome any problems during the years. Her knowledge helped me to get an insight into plasma physics, lasers, and many others. I would also like to thank my co-supervisor, Alexandr Jančárek, for his willingness, assistance, and discussions that contributed to the work, and for his personal attitude.

My special thanks go to my co-supervisor and friend Dalibor Pánek, who helped me many times when I was stuck in the lab. His expertise in many scientific fields is admirable. Our discussions on many different topics provided me with a new view on how to think about matters.

I was very fortunate to have worked with Petr Brůža and Michal Nevrkla, who had taught me a lot about electronics and they introduced laser- and discharge-produced plasma sources to me. It was an amazing experience to watch them in the lab.

I am honered to say thanks to my friend and mentor, Vlastimil Fidler, who has enormous insight over many scientific fields and who encouraged me to critical thinking. His lessons about advanced spectroscopy and microscopy techniques were unforgettable. I am grateful to him for the arrangement of my internship at Brown University, and I would also like to thank him and his wife for all the care they gave me during my stay in the US. I was fortunate to have worked with Christoph Rose-Petruck, whose drive, personal attitude, and passion for moving the boundaries of science were genuinely inspiring.

I would like to thank Jana Turňová for the preparation of the biological samples. Many thanks belong to my colleagues and friends at FBME CTU: Kateřina Žambochová, Lucie Drbohlavová, Šarka Salačová, Milan Tatíček; Fahad Nawaz from FNSPE CTU; Daniel DiCiccio from Brown University. Further, I would like to thank Przemyslaw Wachulak and Alfio Torrisi from the Military University of Technology in Warsaw and Klaus Mann, Matthias Müller from Laser-Laboratorium Göttingen e.V., where I had opportunities to spend my stays.

Finally, I thank to my family, for their love, patience, understanstanding, encouragement, and everlasting support.

This work was financially supported by grants: BIO-OPT-XUV Research Team Advancement at the Faculty of Biomedical Engineering, CTU in Prague, No.: MEYS ESF Project CZ.1.07/2.3.00/20.0092; Ministry of Education, Youth and Sports of the Czech Republic LTT17015 Research in the Frame of the International Center for Dense Magnetized Plasmas, and by CTU Student grant competition SGS19/084 /OHK4/1T/17.

Contents

List of Figures

List of Tables

1 | Introduction

People have always been curious about the macro- and micro-cosmos. They were trying to find and develop an instrument to see a "hidden world," providing them a capability to resolve smaller features than visible by eye alone. The early history of a "microscopy" goes back to the Ancient Greeks. The invention of what is regarded as the first compound microscope is credited to two Dutch spectacle-makers; Zacharias Jansen and his father Hans at the end of the 16th century. Nevertheless, it was not until 1625, when the term "microscope" was coined [1]. The word itself is derived from two Greek words; small and to view, and describes any instrument that increases the resolution of the human eye [2]. One of the early microscopists, who have significantly contributed to microscopy, were Robert Hooke (1635–1703) and Antony van Leeuwenhoek (1632–1726), titled as The Father of Microscopy [3]. Hooke is the author of one of the earliest book on microscopy "Micrographia" [4], published in 1665, including his famous, finely detailed illustrations of tiny living organisms, in which he coins the term "cells" when describing tissue [2]. Leeuwenhoek drew on Hooke's work to take a microscope design to a more sophisticated level; his microscopes were capable of providing magnifications of between 70 and 270× [5,6]. It took another two hundred years to formulate the mathematical theory for the limiting resolution of a light microscope; the equation was formulated by Ernst Abbe in 1873 [7,8],

$$d = \frac{\lambda}{2n \cdot \sin\alpha} \tag{1.1}$$

where d is the minimum separation between two point sources of light that can be resolved as two separate objects, λ is the wavelength of the illumination and $n \cdot \sin\alpha$ is the numerical aperture of the objective lens of the microscope.

In 1893, a robust and flexible method of illumination was proposed by August Köhler [9]. This configuration involves a combination of two lenses and two apertures to generate uniform illumination at the sample plane. This method came to be known as Köhler illumination, and has remained the mainstay of bright-field and fluorescence microscopy ever since [10]. By 1900, the theoretical limit of resolution for visible light microscopes (200 nm) had been reached. The crucial parameter for imaging is not only resolution but the contrast of the image itself.

Several contrast-enhancing techniques were developed, such as phase-contrast microscopy, introduced in 1932 by Frits Zernike [11], or fluorescence microscopy [12]. The milestone in the development of optical microscopes was the invention of confocal microscopy in 1955 [2]. This imaging technique developed by Marvin Minsky allows observing virtual slices through specimens, providing a capability of three-dimensional (3D) imaging through the optical sectioning and overcomes the Abbe barrier. The confocal scanning microscopy has been established as the standard method for high-resolution optical bio-imaging. During the last three decades, the resolution of optical microscopy has been improved beyond the diffraction limit, and many novel super-resolution techniques have been proposed and established. The resolution of current optical microscopes could be below 100 nm, which significantly supports cutting-edge research on cells and tissue for biomedical applications. For example, stimulated emission depletion microscopy (STED) [13–15], structured illumination microscopy (SIM) [10,13], and single-molecule microscopies (SMM), including methods such as photoactivated localization microscopy (PALM) [16], and stochastic optical reconstruction microscopy (STORM) [17]. However, these systems have a high-resolution imaging capability; fluorescence is an essential part of the super-resolution process [18]; hence they come up with their limitations of the requirement of fluorescence markers or staining.

The need to study smaller structures than can be resolved by using visible-light microscopy led to the use of shorter wavelengths. Louis de Broglie introduced the notion of a frequency in 1923, and hence a wavelength for particles $\lambda = h/mv$ [19]. In 1931, Max Knoll and Ernst Ruska, invented the first transmission electron microscope (TEM), and in 1933, they broke through the limit of the optical microscope for the first time [20]. In the 1940s, the first scanning electron microscope (SEM) was developed. Since that time, the resolution was improved to the atomic level ($\sim$ 50 pm) [21], and TEM and SEM have become one of the main imaging techniques in biology and life science, and material research. Although the electron-based microscopic systems provide an impressive resolution, they come up with their limitation in terms of the thickness of the specimen (in order of a few 100 nm). Key events in the history of electron microscopy are described in detail in [19]. In the 1980s, another branch of high-resolution technique arises – scanning probe microscopy, allowing specimens to be viewed at the atomic level. Namely, scanning tunneling microscopy (STM) in 1981 and atomic force microscopy (AFM) in 1986 [2]. However, these imaging techniques are primarily used to study the surface topography.

Since the discovery of a "new kind of rays" by Wilhelm Röntgen in 1895 [22], called X-ray, there has been an effort to use this part of the electromagnetic spectrum for microscopy as the wavelengths are much shorter than visible light. The early soft X-ray microscope was constructed by Paul Kirkpatrick and Albert Baez in the late

1940s [23]. However, it was during the 1970s, and 1980s when the full potential of soft X-ray microscopy was demonstrated. Full-field transmission soft X-ray microscope was pioneered by Schmahl and colleagues [24], and scanning transmission soft X-ray microscope was pioneered by Kirz and colleagues [25]. The development of soft X-ray microscopy is described in more detail in Chapter 3.3. Soft X-ray microscopy has become one of the emerging methods for cell biology, with its spatial resolution in the order of tens nm covering the gap between transmission electron microscopy (TEM) and visible light microscopy. Up to date, the microscopic images with 10 nm spatial resolution have been presented [26]. Soft X-ray (SXR) microscopes typically operate within the "water-window" spectral region, between the K-absorption edges of oxygen (2.28 nm; 543 eV) and carbon (4.36 nm; 284 eV) [27, 28] and have three advantages over light and electron microscopes. Firstly, SXR radiation penetrates biological materials much more easily than electrons, which allows specimens up to 10 µm thick to be imaged. Unlike electron microscopy, there is no need for sectioning eukaryotic cells with an ultramicrotome before imaging. Secondly, the short-wavelength allows to image cells with higher spatial resolution compared to light sources. Finally, image contrast is obtained from the absorption of X-rays by the specimen [29]; thus, there is no need to insert any fluorescence markers or other substances into the sample. This absorption is described by Beer-Lambert's Law, therefore is linear with thickness and concentration [28]. By imaging in the "water-window," organic matter containing carbon and nitrogen absorbs photons at an order of magnitude more than water, which creates inherent contrast to visualize cellular structure [30].

A major part of SXR microscopes is based on large-scale facilities like synchrotron or free-electron lasers, and their advantage is a short exposure time and high spatial resolution contrary to their vastness and the price demands (construction and operation), which does not allow the access to this imaging technique for the broader scientific community. Therefore, since the mid-1990s the first effort to develop a compact, laboratory-scale source appeared. In recent years, considerable progress has been achieved and several SXR microscopes based on table-top sources were reported. Compact SXR microscopic systems based on laser-produced plasma sources using—liquid-jet target [31–33], gaseous target [34, 35], double-stream gas target [36–38], or ultra-thin metal target [39]—were developed. The second branch of laboratory-scale SXR microscopes is based on discharge produced plasma sources using pseudo spark like electrode geometry [40], an electrode-less design (Energetiq, Inc.) [41, 42], or Z-pinching capillary discharge [43, 44]. Even though table-top sources are accessible and easy to operate, they come with their limitation in terms of exposure times and in order to get comparable spatial resolution with large-scale facilities. To improve the brilliance of the compact sources, a jet with a so-called barrel shock system was introduced [45], enhancement of the soft X-ray radiation by

inserting a low-pressure nitrogen atmosphere to increase the conversion efficiency of laser-produced plasma sources was demonstrated [46, 47]. Nevertheless, future development of laboratory-scale sources is necessary to perform a single-shot imaging experiment as the photon flux of these sources is a few orders of magnitude below the requirements for a single shot imaging micrometer-sized specimen [48]; a current perspective of a single shot imaging using compact SXR sources is discussed in [48].

1.1 Aims of the Thesis

The main goal of the Thesis is the development and construction of a laboratory, transmission table-top water-window microscope for biological imaging.

Partial objectives of the Thesis are:

1. Investigation of table-top soft X-ray sources

   To characterize the emission properties of the laser- and discharge-produced plasma soft X-ray sources, and to compare both sources as a potential table-top source for a full-field transmission soft X-ray microscope.

2. Full-field transmission water-window microscope

   To design the microscope layout and suggest suitable optical components. Construction of the table-top transmission water-window microscope. To perform imaging experiments and assess the spatial resolution of the microscope. To evaluate the SXR images qualitatively–signal-to-noise analysis. To prepare a biological specimen and perform imaging experiments with biological cell.

1.2 Thesis outline

This Thesis describes the development and demonstration of the transmission table-top water-window microscope using Z-pinching capillary discharge source for biological imaging with the spatial resolution of 75 nm. The Thesis is sectioning into a theoretic part, Chapters 2 and 3, and an experimental part in Chapters 4 and 5.

Chapter 2 describes the basics of soft X-ray physics, provides an overview of soft X-ray sources and optics used in SXR microscopy. Chapter 3 explains the image formation in SXR microscopy and gives the historical overview of the development of water-window microscopes as well as the state of the art of compact water-window microscopes. Chapter 4 presents the investigation of two table-top SXR sources in possession of CTU in Prague. Finally, Chapter 5 describes the transmission water-window microscope based on the capillary discharge source, including the demonstration of biological imaging. Chapter 6 summarizes the achieved goals and offers a future outlook.

2 | Soft X-ray, sources and optics

2.1 Soft X-ray interactions with matter

The soft X-ray region in the wavelength of about 0.3–5 nm (corresponding to 250 eV; just below the carbon K-edge, to several keV) is very well suited for X-ray microscopy studies, especially the spectral region between the K-absorption edges of oxygen (2.28 nm; 543 eV) and carbon (4.36 nm; 284 eV), called water-window [28, 49]. The reasons are that the interaction of SXR with matter is very favorable for the biological studies as SXR radiation penetrates biological materials much more easily than an electron, see Figure 2.2, providing a tool to image an intact cell in a native environment without a need of sectioning of the specimen. Due to its short wavelength provides a better resolution than other imaging techniques using visible light. Finally, the image contrast is obtained from the absorption of SXR radiation by the specimen; thus, it does not require fluorescent markers or staining that modifies the morphology of the sample. Furthermore, high-resolution X-ray optical elements can be built for this wavelength range.

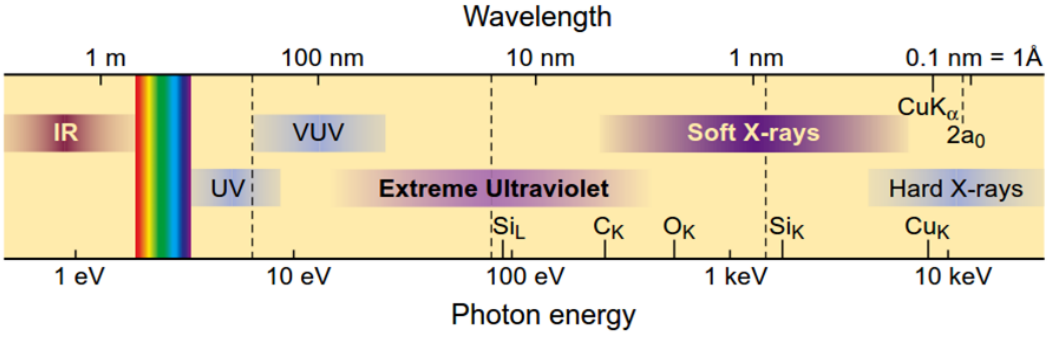

Figure 2.1: The electromagnetic spectrum from infrared to the X-ray regions. The carbon K-absorption edge at 284 eV (4.36 nm), and the oxygen K-absorption edge at 543 eV (2.28 nm) are shown [28].

The interaction of SXR with matter is dominated by elastic scattering and photoelectric absorption (see Figure 2.3), or, expressed in a different way, by a phase shift of the incoming wave and an attenuation of its amplitude [49].

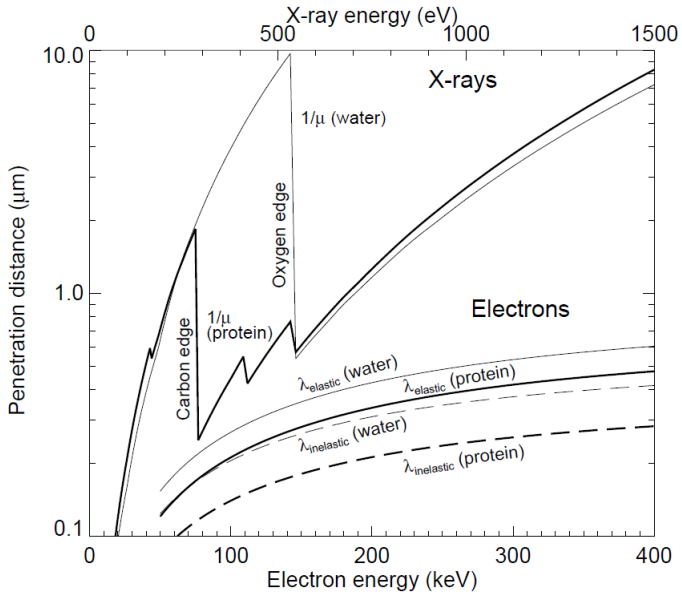

Figure 2.2: Penetration distances in water and protein for electrons and X-rays. For electrons, the mean free paths λ for elastic and inelastic scattering were obtained using the approximate expressions of Langmore and Smith [50]. For X-rays, the 1/e attenuation lengths $1/\mu$ were obtained using the data of [51]. Adapted from [52].

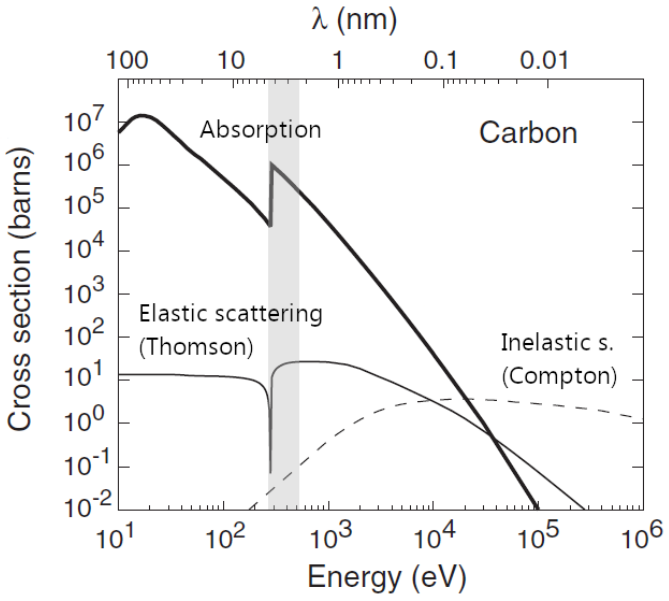

Figure 2.3: Scattering and absorption cross-section for carbon. Photoelectric absorption is the most dominant process for soft X-rays in the water-window (shaded area). All interactions decrease with energy but scattering decreases slower and therefore becomes the dominating process above ~ 20 keV. One barn corresponds to 10^{-24} cm^2. Adapted from [53].

In general, the propagation (**r**,t) of a plane wave in a material can be described as

$$\mathbf{E}(\mathbf{r},t) = \mathbf{E_0} e^{-i(\omega t - \mathbf{k}\cdot\mathbf{r})} \tag{2.1}$$

where ω is the frequency and **k** is complex propagating vector.

The interaction of soft X-ray with atoms is described by the atomic scattering factor $f = f_1 - if_2$. It is an element-specific strongly varying analytic function of photon energy, especially near electron binding energies. Its real and imaginary parts are related by the Kramers-Kronigs relation [54]. The complex index of refraction n describes the optical properties of a material and, in the case of forward scattering, it relates to the atomic scattering factor by

$$n = 1 - \delta + i\beta = 1 - \frac{n_a r_e \lambda^2}{2\pi}(f_1 - if_2) \tag{2.2}$$

where n_a is the average density of atoms, $r_e = 2.82 \times 10^{-15}$ m the electron radius and λ is the wavelength.
Thus

$$\delta = \frac{n_a r_e \lambda^2}{2\pi} f_1 \tag{2.3}$$

$$\beta = \frac{n_a r_e \lambda^2}{2\pi} f_2 \tag{2.4}$$

The complex propagating vector **k** can be expressed as

$$k = \frac{\omega}{c} n = \frac{\omega}{c}(1 - \delta + i\beta) \tag{2.5}$$

Substituting this into equation 2.1, in the propagation direction defined by $\mathbf{k}\cdot\mathbf{r} = \mathrm{kr}$, we obtain

$$\mathbf{E}(\mathbf{r},t) = \underbrace{\mathbf{E_0} e^{-i\omega(t-r/c)}}_{\text{vacuum propagation}} \cdot \underbrace{e^{-i(2\pi\delta/\lambda)r}}_{\phi\text{-shift}} \cdot \underbrace{e^{-(2\pi\beta/\lambda)r}}_{\text{decay}} \tag{2.6}$$

where the first exponential factor represents the phase advance had the wave been propagating in vacuum, the second factor represents the modified phase shift due to the medium, and the third factor represents decay of the wave amplitude.

For solid or liquid materials in the water-window δ is typically in the order of 10^{-3}, while β varies between 10^{-5} and 10^{-3} [55]. The real part of complex refractive

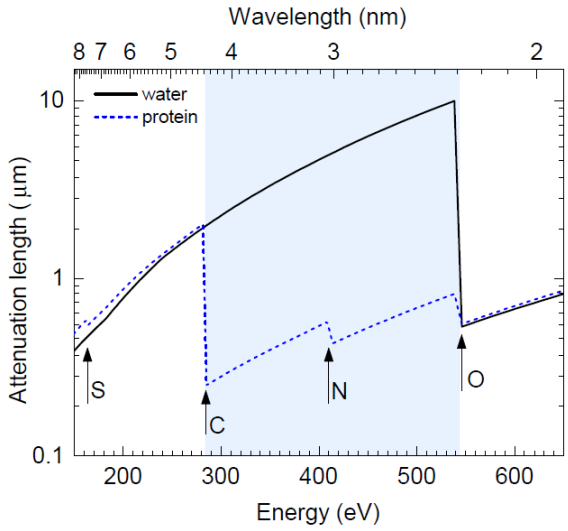

Figure 2.4: The calculated absorption length of water and typical protein in the water-window energy region. Calculations are based on the protein composition from [56] and optical data from [51, 57]. The blue area represents the water-window region. Adapted from [58].

index, $1 - \delta$, determines the phase velocity, which after a propagation distance Δr results in a phase shift given by

$$\Delta\phi = \left(\frac{2\pi\delta}{\lambda}\right)\Delta r \tag{2.7}$$

The imaginary part, β, relates to an exponential decay of the intensity I_0 according to Beer-Lambert's law

$$I(r) = I_0 exp\left(-\frac{4\pi\beta}{\lambda}r\right) = I_0 e^{-\mu r} \tag{2.8}$$

where μ is the absorption coefficient of the material.

The absorption length can be calculated from equation 2.8 as

$$l_{abs} = \frac{\lambda}{4\pi\beta} \tag{2.9}$$

The absorption length for soft X-ray in the water-window and major elements in a biological sample is depicted in Figure 2.4. The typical protein consists of 53 % carbon and 16.5 % nitrogen [59]; in this manner, the organic matter absorbs photons at an order of magnitude more than water as protein's native environment, which creates inherent contrast to visualize cellular structure.

From the f_1 and f_2 values, tabulated by Henke *et al.* [51], it follows that δ and β of the complex refraction index are much smaller than 1 in the whole range of SXR radiation. This property of X-rays causes a near absence of reflections at interfaces

and results in very clear images, even of thick specimens (up to 10 μm). On the other hand, the small δ and β values make it more difficult to build high-resolution SXR optics [49].

2.2 Contrast, dose, and radiation damage

In imaging, contrast is essential and of equal importance as the resolution of the microscope. Good contrast is particularly important when dealing with microscopies involving ionizing radiation, for contrast is directly related to the radiation dose that must be given to the specimen to record the image at a given resolution. The standard method for obtaining the contrast for X-ray imaging of biological cells has been based on calculating the real (δ) and/or imaginary (β) refractive indices for protein and water, described in equation 2.2. The contrast expected from X-ray imaging can be calculated as a function of X-ray energy. For phase contrast, both the real (δ) and imaginary (β) parts of the complex refractive index contribute, although, away from absorption edges, the real part dominates. For absorption contrast, the imaginary part contributes [60]. The modulus of the electron density can be obtained from the expression

$$\rho = 2\pi \frac{[(\delta - \delta_0)^2 + (\beta - \beta_0)^2]^{1/2}}{\lambda^2 r_e} \tag{2.10}$$

where the subscript zero refers to the background material (nucleosol or cytosol), λ is the wavelength and r_e is the classical radius of the electron.

Knowledge of the composition and density of the cellular components allows calculations of the required fluence (photons $\times$ μm^{-2}) needed to obtain a defined resolution following the procedures for imaging a protein in water [60].

The relationship between contrast and minimum exposure was established by Rose [61]. His studies of image formation resulted in the following criterion: to render an arbitrarily shaped object visible in a noisy image, the signal to noise ratio should be at least in the range of 3–5. The Rose criterion was first applied to X-ray microscopy by Sayre *et al.* [62]. If the Rose criterion is applied for imaging by absorption contrast, the signal for protein against water is

$$N_c = N_v \mid T_p - T_w \mid \tag{2.11}$$

where N_v is the number of incident photons on a voxel, T_p is the transmission for protein and T_w is the transmission for water. The corresponding standard deviation is

$$\sigma_c = \sqrt{(N_v T_p + N_v T_w)} \tag{2.12}$$

To observe the feature, it requires $N_c = k\sigma_c$ where k is the Rose criterion. This expression leads to

$$N_v = k^2 \frac{(T_p + T_w)}{\mid T_p - T_w \mid^2} \tag{2.13}$$

The required fluence is

$$N_0 = N_v/d^2 \tag{2.14}$$

and the required radiation dose D [63] is then found as the energy deposited per unit mass

$$D = \frac{\mu N_0 h\nu}{\rho} = \frac{hc}{\lambda}\frac{N_v \mu}{d^2 \rho} \tag{2.15}$$

where D is in Gray (J/kg), ρ is the density, μ is the linear absorption coefficient defined in equation 2.8, and hc/λ is the energy carried by each photon (assumed to be deposited in the specimen).

The transmission probabilities are given by equation 2.8. With absorption contrast and values of T_p and T_w near 1, the required number of photons (transmitted through a voxel) scales as d^2 due to the term $\mid T_p - T_w \mid^2$. The fluence and hence dose scales as the fourth power of the resolution [63].

Figure 2.5 illustrates radiation dose for minimal exposure, a dose about of $\sim 10^6$ Gy is required to identify a 50 nm cube of protein in a 10 μm thick water layer, while if the cube is only 10 nm in size, the dose grows to over 10^8 Gy [52]. The water-window wavelengths provide a "dose advantage" for absorption imaging as the obvious drop in dose occurs in this spectral region as demonstrated in Figure 2.5.

The relationship between radiation dose and radiation damage is what determines whether the image recorded resembles the true biological structure, or the result of changes brought about by the exposure. Typically, a water-window X-ray microscope image requires $\sim 10^6$ Gy for absorption imaging of 50 nm protein object in 10 μm of water under realistic assumptions [52, 64]. This can be lowered 0.5–1 order of magnitude by phase imaging. Dehydrated (dry) samples are stable up tp doses of $\sim 10^7$ Gy [52]. Hydrated biological samples show structural changes already at $\sim 10^4$ Gy [64]. Chemical fixation allows up to $\sim 10^6$ Gy, while cryo fixation has been shown to provide stable samples for $\sim 10^{10}$ Gy [65]. For a better imagination, a dose of 10^{10} Gy in ice corresponds to 10^{12} photons/μm^2. This is important since the typical data acquisition for three-dimensional (3D) tomographic imaging at synchrotron presently is at the $\sim 10^9$ Gy level [32].

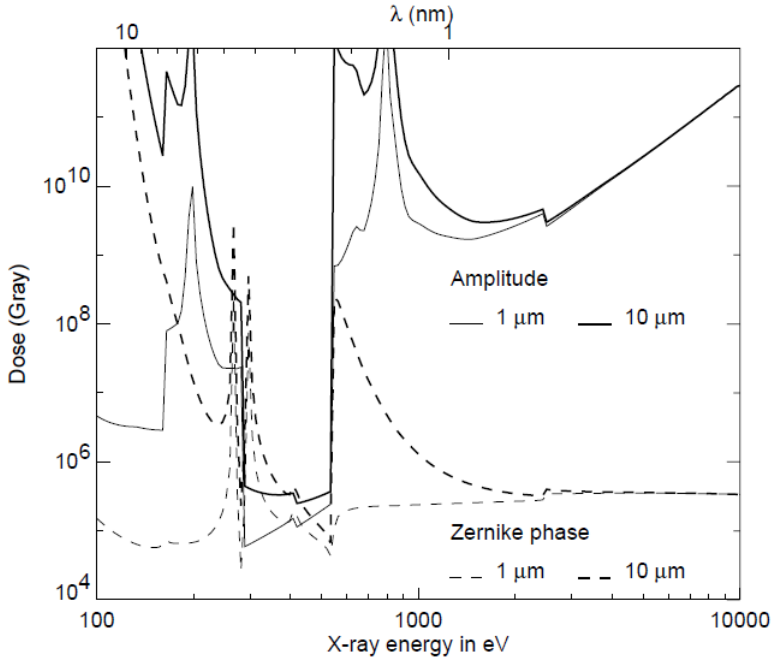

Figure 2.5: Radiation dose calculated for minimal exposure imaging (signal:noise=5:1) of 50 nm protein structures in 1 and 10 μm thick ice layers (ρ = 0.92). Both amplitude (solid lines) and Zernike phase contrast cases (3π=2 phase plate with no absorption) are shown. Adapted from [52].

It has been reported that the main radiation damage for chemically fixed samples is mass thickness loss and sample shrinkage, whereas for fully hydrated samples such doses can damage living bacteria and cause apoptosis, chromosomal aberration, DNA mutations and loss in the reproduction ability of living cells [66].

2.3 Soft X-ray sources

The soft X-ray source is the determining component in the soft X-ray microscope and can be described by the most crucial parameter in microscopy, *brilliance* or *brightness*. In the synchrotron community, it is usually defined as photons / (s $\times$ sr $\times$ μm^2 $\times$ 0.1% BW), where BW is the bandwidth. Brightness for pulsed sources is usually expressed by photons per pulse, and by photons per line in the case of the line-emitting sources. Soft X-ray sources for water-window wavelengths can be divided into two main categories; synchrotrons and free-electron lasers, and laboratory-scale sources. Nevertheless, significant progress has been made in the development of table-top sources during the last two decades; their brightness cannot be matched with the synchrotron-like sources. To have a perspective, Figure 2.6 illustrates the comparison of the spectral brightness between laboratory and synchrotron sources using for the water-window microscopy. In imaging, as it was mentioned in the previous section, contrast is of the fundamental significance, therefore for the high-

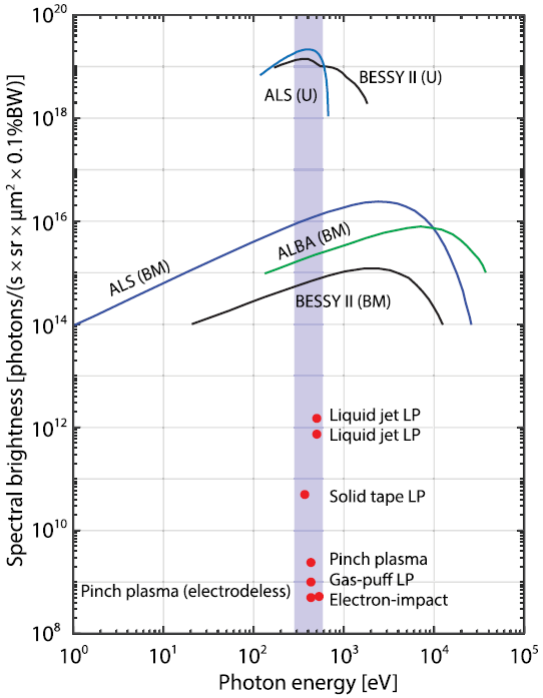

Figure 2.6: Brightness of water-window laboratory sources used for microscopy (LP, laser plasma). The water-window energy range is indicated by the blue bar. For comparison, microscopy beamlines at three synchrotrons are included (U, undulator; BM, bending magnet). Adopted from [67].

resolution images, a sufficient number of X-ray photons have to reach a small area in the specimen. Sources with higher brightness reduce the exposure time, which is the main limitation for using water-window microscopies in some laboratories. Apart from a demand for a high-brightness spectral source, the narrow-bandwidth is requested ($\lambda/\Delta\lambda > 500$).

2.3.1 Synchrotrons and free-electron lasers

As the synchrotron radiation, we understand the electromagnetic waves emitted by a charged particle (electron or positron) moving with relativistic velocity and undergoing a transverse acceleration. It is characterized by a small opening angle and a high frequency caused by the velocity of the charge being close to that of light [68]. The first observation of the synchrotron radiation was at the General Electric Research Laboratory in Schenectady, New York, in 1947 [69], initially viewed as a negative attribute in circular particle accelerators. The first accelerator dedicated to synchrotron radiation started at the Synchrotron Radiation Source in Daresbury around 1970 [70]. Since that time, synchrotron radiation has become a basis for many scientific fields, including soft X-ray microscopy. Currently, there are four cryo soft X-ray microscopes based on synchrotrons worldwide including the Advanced Light Source (ALS) in Berkeley (CA, USA), BESSY II in Berlin (Germany), ALBA in

Barcelona (Spain) and the Diamond Light Source in Didcot (UK) [71], see Figure 2.6.

Free-electron lasers (FEL) are considered to be the next generation of X-ray sources, offering coherent femtosecond X-ray pulses with extremely high peak spectral brightness [55]. The concept of FEL was introduced in 1971 by John Madey [72], and the first operation of an FEL was in 1977 [73]. Nowadays, there are two FELs operating in the soft X-ray region, FLASH [74] and Fermi [75], operating at DESY, in Germany, and Sincrotrone Trieste, in Italy, respectively, and the third is under development (Linac Coherent Light Source (LCLS-II), CA, USA).

The advantages of synchrotron and FELs facilities are high spectral brightness and tunable wavelengths from infrared to X-ray. In 2016, more than 60 synchrotron and 20 FEL light sources were operational worldwide, with others in the construction or planning phase [76]. The following paragraphs describe the uderlying theory and principle of these facilities. The more comprehensive theory for synchrotron radiation is described in [28,68,77], and the theory of FEL in [78], especially in [79].

Synchrotron radiation is generated by three types of magnetic structures: bending magnets, undulators, and wigglers. Bending magnets cause a single curved trajectory as pictured in Figure 2.7a. The result is a fan of radiation around the bend. Undulators are periodic magnetic structures with relatively weak magnetic fields. The periodicity causes the electron to experience a harmonic oscillation as it moves in the axial direction, resulting in a motion characterized by small angular excursions called undulations, as shown in Figure 2.7c. The weak magnetic fields cause the amplitude of this undulation to be small. Hence, the resultant radiation cone is narrow. In combination with a tightly confined electron beam, this leads to radiation with small angular divergence and relatively narrow spectral width, properties we generally associate with the coherence properties of lasers. Wigglers are a strong magnetic field version of undulators. Due to the stronger fields, the oscillation amplitude and concomitant radiated power are larger. The radiation cone is broader in both space and angle. The radiation spectrum is similar to that of bending magnets, but characterized by a much larger photon flux and a shift to shorter wavelengths, as seen in Figure 2.7b [28]. Wigglers and undulators, called insertion devices, are placed in the straight sections between the bending magnets [68, 80]. Current synchrotron facilities (third generation) are composed of many straight sections specially optimized to produce high brightness undulator and wiggler radiation.

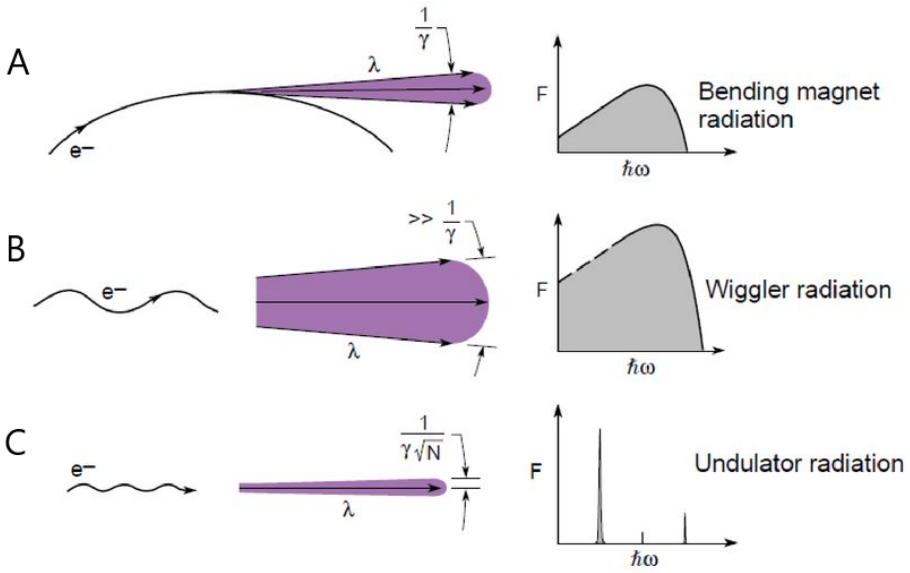

Figure 2.7: Magnetic structures commonly used to produce synchrotron radiation: **(a)** Bending magnet radiation occurs when a relativistic electron travels in a uniform magnetic field, executing a circular motion with acceleration directed toward the center. The radiation is directed tangentially outward in a narrow radiation cone. The radiation spectrum is very broad, analogous to a "white light" X-ray light bulb. The emission angle is typically $1/\gamma$, where γ is the Lorentz contraction factor. **(b)** Wiggler radiation is generated as a highly relativistic electron traverses a periodic magnet structure, in the strong magnetic field limit where in at least one plane, the angular excursions are significantly greater than the natural $(1/\gamma)$ radiation cone. Because accelerations are stronger in this limit, the radiation generated peaks at higher photon energies and is more abundant (higher photon flux and more power). The radiation spectrum is very broad, similar to that of the bending magnet. Although more power is radiated, wiggler radiation is less bright because of the substantially increased radiation cone. **(c)** Undulator radiation is also generated from a periodic magnetic field. In the undulator limit, the magnetic field is relatively weak, and the resultant angular excursions of the electron are smaller than the angular width of the natural radiation cone, $1/\gamma$, normally associated with synchrotron radiation. The frequency spread of undulator radiation can be very narrow, and the radiation can be extremely bright and partially coherent, under certain circumstances. The characteristic emission angle is narrowed by a factor $\sqrt{N}$, where N is the number of magnetic periods. Typically N is of order 100. Adopted from [28].

The narrow forward radiation cone of half angle is defined as

$$\theta \simeq \frac{1}{2\gamma} \tag{2.16}$$

where γ is Lorentz contraction factor (relativistic factor) defined as

$$\gamma \equiv 1/\sqrt{(1 - v^2/c^2)} \tag{2.17}$$

where v is the relative velocity between frames, and c is the velocity of light.

The non-dimensional magnetic strength for a periodic magnet parameter, called *magnetic deflection parameter*, is

$$K \equiv \frac{eB_0\lambda_u}{2\pi mc} = 0.9337 \cdot B_0(T)\lambda_u(cm) \tag{2.18}$$

where e is the charge of electron, B_0 is the periodic magnetic field, λ_u is the period of the magnetic structure, and m is the mass of electron.

According to the magnetic deflection parameter, for undulators is $K \leq 1$, while in the case of wigglers $K \gg 1$.

The FELs system consists of an electron accelerator, an undulator in which the electrons emit the synchrotron radiation, and an optical resonator. The operating principle of the FEL has many similarities with synchrotron sources. In FEL, a beam of relativistic electrons produced by an accelerator passes through a transverse periodic field produced by undulators and exchanges energy with an electromagnetic field. As a result of energy exchange, the electrons that gain energy begin to move ahead of the average electron, while the electrons that lose energy begin to fall behind the average. The beam then becomes bunched on the scale of the radiation wavelength, and this collective motion of the bunches radiates powerful coherent radiation. The wavelength of the emitted radiation at the resonance depends on the electron energy and the magnitude and periodicity of the undulator field according to the relation [81]

$$\lambda_0 = \frac{\lambda_u}{2\gamma^2}(1 + \frac{K^2}{2}) \tag{2.19}$$

K magnetic deflection parameter and γ reletivistic factor were defined above.

In the soft X-ray wavelength range, a high-gain FEL operates in self-amplified spontaneous emission (SASE) mode and can generate multi-gigawatt and femtosecond coherent X-ray pulses [82]. The intensity of radiation is proportional to a squared number of electron (N_e^2), rather than just N_e, as in conventional undulators where electrons radiate independently. FELs are therefore capable of producing X-ray pulses with up to 8 orders of magnitude higher peak spectral brightness compared to third-generation synchrotron sources [55, 83].

2.3.2 Compact soft X-ray sources

A desire to broaden the soft X-ray imaging technique outside the large-scale synchrotron-like facilities led to the beginning of the development of compact, laboratory-sized soft X-ray sources in the mid- 1990s. As a table-top alternative to synchrotron radiation sources, the hot, dense plasma-based sources were developed. According to

the plasma origin, the laboratory sources can be categorized into two main branches; the one where plasma is induced by a laser pulse, and the second one where plasma is generated by a current discharge.

2.3.2.1 Laser-produced plasma sources

In the laser-produced plasma (LPP) sources, hot dense plasma is formed in a small volume when a high peak-power laser ($\sim 10^{13}$ W/cm^3) is focused onto a target material such as bulk (solid) [39, 84, 85], tape targets [86], liquid or droplet targets [31–33, 87], and gas-puff targets [88–91], the target types are illustrated in Figure 2.8a. As the laser pulse hits the target, free electrons are created during the first picoseconds. The plasma is then rapidly heated by energy transfer from the incoming photons to the kinetic energy of free electrons, i.e., inverse bremsstrahlung absorption. As the plasma is heated, more free electrons are generated, and an electron density gradient arises [80], as shown in Figure 2.8b. The electron distribution oscillates at a frequency called *plasma frequency* defined by

$$\omega_p = \sqrt{\frac{e^2 n_e}{\varepsilon_0 m_e}} \tag{2.20}$$

where n_e is the electron density, e is the electron charge, m_e is the electron mass and ε_0 is the vacuum permittivity. The propagation of the incoming radiation through the plasma can occur if $\omega > \omega_p$ is satisfied [80].

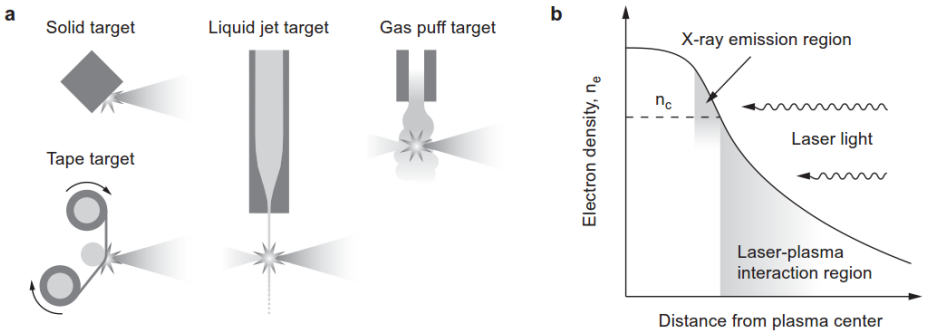

Figure 2.8: Laser plasma sources. **(a)** Target types used for soft X-ray generation [55]. **(b)** Schematic diagram of the electron density in a LPP. Light is absorbed where the density is below the critical density (dashed line). Energy transferred to the denser region causes intense emission of soft X-rays [28].

Alternatively, expressed in a different way, the laser light of wavelength λ, propagates into the material the electron density increases until it reaches the critical density

$$n_c = \frac{1.11 \cdot 10^9 \, \mu m^{-1}}{\lambda^2} \tag{2.21}$$

where the wave can no longer propagate and is instead reflected back and lost. Close to the critical electron density, the energy transfer is the most efficient, and consequently, a region of intense X-ray emission is created, as it demonstrates in Figure 2.8b [67, 92].

The properties of a laser-plasma are determined by a complex relation between laser absorption, electron and ion temperature, density, expansion rate, photon emission and re-absorption, and coupling between acoustic and electromagnetic waves [55, 93]. The properties of X-ray emission can be partly explained by considering blackbody radiation and Wien's displacement law [67],

$$\lambda_{peak} = \frac{2.898 \cdot 10^6 \, nm \cdot K}{T} \tag{2.22}$$

Therefore, soft X-rays in the water-window are emitted at the temperature in the order of 10^6 K, corresponding to the simulated value, where the ideal temperature for the emission in the water-window region is between 80-120 eV [94], (1eV = 11600 K).

The emitted spectrum consist of a broad continuum of bremsstrahlung from interactions between free electrons and ions, and narrow line emission from bound electron transitions in ionized atoms of various charge states. Bremsstrahlung dominates the spectrum from plasmas with heavy atoms. In low-atomic-number plasmas, atoms will be nearly or fully ionized, and therefore line emission will dominate. Doppler-broadening from the fast plasma expansion (order of μm/ps) results in a typical linewidth of $\lambda/\Delta\lambda \approx 500$–$1000$. The source size depends on focus size, pulse length, and target, but is typically 20–500 μm [55]; the source size is typically in the order of tens μm in the case of a liquid and solid target, and order of hundred μm in the case of a gas target. For the detailed overview of all parameters of sources used in the laboratory water-window microscopes go to section 3.4, where the source parameters are provided together with employed optics and achieved spatial resolution.

Even though the solid-target plasma sources provide the highest photon flux of LPP systems (1.3×10^{15} photons / (sr $\times$ pulse)) [95], they produce a significant amount of debris making them a difficult to use in microscopy for a longer period, especially, in combination with the sensitive optics. Whereas the liquid- and gas-target plasma sources offer a very low-debris operation. Another benefit of liquid-

and gas-target plasma source is their renewing of the target materials, as the laser pulse destroys the material. A continuous liquid jet typically operates with the velocity of 20-50 m/s [96], providing new target material at a rate that allows for laser repetition rates up to several kilohertz, which translates to high average X-ray power and brightness [67]. However, it sets high demands on the jet stability [96]. The gas-target plasma sources typically operate in a discrete mode, where pressurized gas is injected into a vacuum chamber (puff), which requires synchronization with the laser pulse. However, the main limitation is the repetition rate of the laser caused primarily by the nozzle opening. Thus, the repetition rate of gas-puff target sources is in order of a few Hz. On the other hand, the operation and maintenance of the gas-puff target source are rather easy. To increase the brilliance of the LPP sources, several improvements were introduced; Wachulak *et al.* employed a double nozzle to increase the density of the target, using nitrogen as a "working" gas, and helium as an "outer" gas to narrow the nitrogen target [88]. A jet with a so-called barrel shock system was introduced [45], and enhancement of the soft X-ray radiation by inserting a low-pressure nitrogen atmosphere to increase the conversion efficiency of laser-produced plasma sources was demonstrated [46, 47].

2.3.2.2 Discharge-produced plasma sources

The discharge sources are further laboratory-scale sources based on a hot dense plasma generated by an electric discharge. The first observation of large soft X-ray amplification in a discharge-produced plasma (even though outside the water-window range) was by Rocca *et al.* in 1994 [97]. In discharge-produced plasma (DPP) sources is plasma formed by a high current pulse (in order of kA) driving through a low-pressure gaseous target. At the beginning of the discharge, the current flowing through the gas will create a low-temperature plasma. The free charges of the plasma reduce the resistance, and the discharge current quickly increases, inducing a strong magnetic field that pulls off-axis-moving charged particles towards the central axis. This process is known as Z-pinch. Plasma is compressing or "pinching," thereby increasing the density and temperature to levels where soft X-rays are emitted [55]. The principle of pinch dynamics is illustrated in Figure 2.9.

The soft X-rays are emitted at temperatures of $\sim 10^6$ K, following the Wien's displacement law, mentioned in the previous section. The discharge-produced plasma sources have a larger source size compare to the LPP sources, from a few hundred μm up to over 1 mm. As the gaseous target nitrogen is exclusively used for its quasi-monochromatic radiation at 2.88 nm (helium-like ions). For the detailed overview of all parameters of sources used in the laboratory water-window microscopes go to section 3.4, where the source parameters are provided together with employed optics and achieved spatial resolution.

Several discharge-plasma sources were reported [41, 98–100], including pseudo-

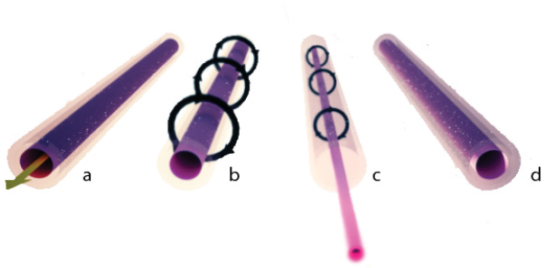

Figure 2.9: Z-pinch Dynamics. **(a)** A capillary with two electrodes at both ends is filled with a gas. A high voltage is applied rapidly and a discharge takes places, flowing current to one electrode to the other. **(b)** The Lorentz force created by the fast current compresses the plasma column inwards. **(c)** The plasma becomes hotter and denser while compressing. It will continue compressing until the plasma pressure equals the magnetic pressure (Z-pinch). **(d)** After this point the hot dense plasma is under expansion [80].

spark like electrode geometry, using a hollow cathode (or anode) [40, 101], or an electrode-less Z-pinch design developed by Energetiq, dealing with an issue of melting electrodes and producing debris by generating the pinch via magnetic inductive coupling instead of electrodes [41].

2.3.2.3 Electron-impact soft X-ray sources

Another table-top soft X-ray sources with the emission in the water-window are electron-impact sources. These systems utilize oxygen K-α emission line at 525 eV (2.36 nm). The principle is based on the interaction between electron-beam delivered by an electron gun and the target material, solid (Cr_2O_3) [102], or liquid (water-jet) [103], resulting in emission at 2.36 nm and broad-band bremsstrahlung. Nevertheless, the reported photon flux of these sources is about a few orders lower compared to laser-produced and discharge-produced sources. A higher brightness can be achieved by using a higher power electron gun; however, increased power will result in thermal instabilities of the target and will affect the lifetime of the electron gun [104]. Despite these obstacles, a water-window microscope based on an electron-impact source was demonstrated, all the parameters of the source and employed optics, as well as the spatial resolution, are listed in the overview in section 3.4.

2.4 Soft X-ray optics

The optics is of fundamental significance in microscopy and have a direct influence on the achievable resolution of the microscope. The refractive index is very close to unity in the soft X-ray region, as it was discussed in section 2.1, thus due to a strong absorption the refractive lenses known from visible-light microscope cannot be used

in X-ray microscopes (they would have impossibly long focal lengths (≥10 m), very small depths of focus (few μm), and they would absorb essentially all of the incident radiation [105]). Therefore, a reflective and diffractive optics are the only eligible optics for soft X-ray wavelengths. In the laboratory water-window microscopy, the soft X-ray optics can be sorted into two categories, the one which collects the incoming light and focuses it onto the sample (condenser optics) and the second one which create an image of the sample (objective optics). The available condenser and objective optics will be discussed in the following sections, including the description of their basic theory and working principles. The more comprehensive theory to soft X-ray optics can be found in [28, 105, 106].

2.4.1 Reflective optics

The reflectivity R at an interface between two materials is determined by their refractive indexes and is given by Fresnel's relations [107].

$$R_{\perp} = \left| \frac{n_1 \cos\theta_1 - n_2 \cos\theta_2}{n_1 \cos\theta_1 + n_2 \cos\theta_2} \right|^2 \tag{2.23}$$

$$R_{\parallel} = \left| \frac{n_2 \cos\theta_1 - n_1 \cos\theta_2}{n_2 \cos\theta_1 + n_1 \cos\theta_2} \right|^2 \tag{2.24}$$

where $\perp$ and $\parallel$ are for perpendicular and parallel polarization relative the plane of incidence, n_1 and n_2 are the refractive indexes, and θ_1 and θ_2 are the incidence angles, respectively angles of reflection.

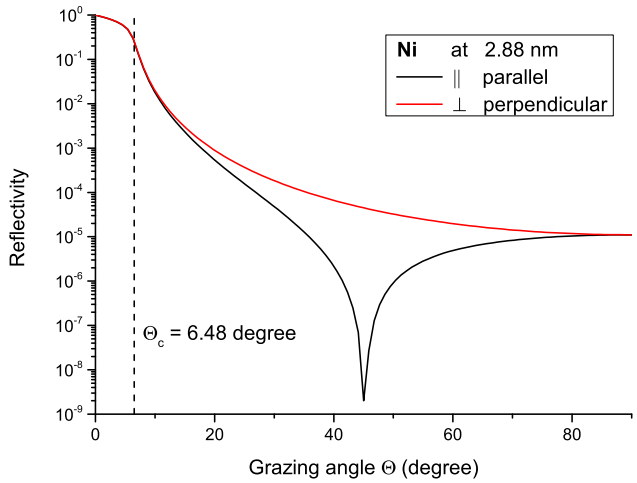

Figure 2.10: The calculated reflectivity for $\perp$ and $\parallel$ polarized soft X-ray at 2.88 nm on nickel surface. The angle is measured from the surface. Calculations are based on optical data from [51]. A dashed line represents critical angle for Nickel at 2.88 nm (430 eV).

Normal incidence reflectivities are very small for all materials over the soft X-ray range, as Figure 2.10 illustrates, which means that conventional mirrors cannot be used. This is due to the fact that the refractive index is very close to unity, so there is a little change of field amplitudes across the interface. However, there is an exception for radiation incident at a glancing angle to the material surface, far from the surface normal. Another way to enhance the reflectivity is by causing multiple reflections to interfere constructively, as in Bragg diffraction from the crystal layer.

The main difference between the grazing-incidence optics and multilayer optics is their reflectivity bandwidth. A multilayer mirror has a small bandwidth and therefore it acts as a monochromator, selecting a specific line from the source spectrum. Whereas a mirror in grazing incidence is an achromatic optic and has to be used in combination with a spectral filter if the objective requires a small bandwidth [67].

2.4.1.1 Grazing-incidence mirrors

As it was stated in the previous section, the reflectivity of a single surface at normal or near-normal incidence for soft X-rays are very small. The reflectivity dependence on the incident angle demonstrates Figure 2.10, where the reflectivity is very low except the area of few degree angles. If the incidence radiation is at a glancing angle to the material surface, radiation of any polarization experiences near-total reflection. Thus for near-glancing incidence (θ_1 near $\pi/2$) the refraction angle θ_2 can equal $\pi/2$, indicating that to first order, the refracted wave does not penetrate into the material, but rather propagates along the interface. The *critical angle for total external reflection* of X-rays and EUV radiation was first obtained by Compton [28] and can be written as

$$\theta_c = \sqrt{2\delta} \tag{2.25}$$

From equation 2.3, it means the critical angle is material- and wavelength-dependent.

The real reflectivity of the grazing-incidence mirror depends on the roughness of the mirror surface, incidence angle, and other factors and was calculated between 40 % and 70 % at grazing-incidence angles of few degrees (typically 1–3) for nickel-coated ellipsoidal mirrors [67]. The Ni-coated ellipsoidal mirrors were used in various laboratory water-window microscopes [34, 87, 108, 109]. However, this type of mirror usually has significant off-axis aberrations. To reduce the aberrations when using spherical mirrors, it is necessary to use larger grazing angles (to reduce astigmatism) and small apertures (to reduce spherical aberration and coma) or the compound systems consisting of two or more spherical or aspherical surfaces can be used [105]. There are two main types of compound system, Kirkpatrick-Baez system [110] using

two cylindrical mirrors with equal radii of curvature; thus, astigmatism is removed, or Wolter (type I) system, which consists of parabolic and hyperbolic mirrors; thus, astigmatism and spherical aberration are eliminated for this system. Several table-top water window microscopes were reported using Wolter (type I) mirror [102,111]. The nickel-coated ellipsoidal mirrors are used as a condenser optics, while Wolter (type I) mirrors can be used as a condenser or objective optics.

2.4.1.2 Multilayer mirrors

Reflectivity at non-grazing incidence angles, and in particular at normal or near-normal incidence, may be enhanced by causing multiple reflections to add in phase, in a manner analogous to Bragg reflection from a crystal [105]. At an interface between two media, the Fresnel equations can be used to calculate the reflectivities for glancing incidence angles greater than the critical angle. Typically, it is found that between 10^{-4} and 10^{-6} of the incident intensity is reflected (see Figure 2.10), i.e., the coefficient of amplitude reflection is between 10^{-2} and 10^{-3}. Thus, neglecting absorption, if reflections from about 10^2 or 10^3 interfaces can be caused to add in phase, all of the incident intensity can be reflected. In practice, because of absorption, total reflection is not possible [105].

Presume a periodical structure consist of N bilayers; then, the reflection conforms to Bragg's law

$$m\lambda = 2d\sin\theta \tag{2.26}$$

where m=1,2,3... is the Bragg number, λ is the wavelength, d is the thickness of one bilayer, and θ is the angle measured from the surface.

Thus, according to Bragg's law, for normal incidence reflection ($\theta = 90°$, m=1), individual layers are each about $\lambda/4$ thick, meaning for soft X-rays each layer is only a few atoms thick. Due to the lack of interface perfection on this spatial scale, the interference is greatly reduced. However, off-normal incidence is still possible and very useful, following Bragg's law.

Multilayer mirrors consist of a substrate onto which layers of two different materials periodically alternate, with low and high atomic number (Z). The spectral bandwidth is determined by the number of bilayers N and is of order mN. Typically, N for soft X-ray wavelengths is in order of a hundred. The illustrated cross-section of a multilayer is depicted in Figure 2.11.

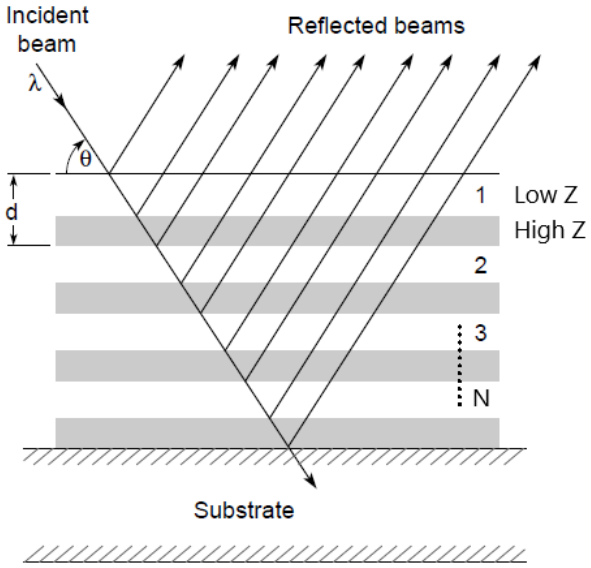

Figure 2.11: A cross-section of a multilayer mirror, with alternating low- and high-Z materials, causing a constructive interference. Adapted from [112].

The more precise form of Bragg's law for refraction in the multilayer mirror [28] is

$$m\lambda = 2d\sin\theta\sqrt{1-\frac{2\overline{\delta}}{\sin^2\theta}} \tag{2.27}$$

where $\overline{\delta}$ is the bilayer weighted real part of the refractive index.

The total reflectivity is the vector sum of the complex reflection coefficients at each interface, with the different path lengths taken into account. For the reflectivity on a single ideal boundary, for normal incidence and small δ and β can be approximated by [55]

$$R = \left|\frac{n_1 - n_2}{n_1 + n_2}\right|^2 \approx \frac{\Delta\delta^2 + \Delta\beta^2}{4} \tag{2.28}$$

where $\Delta\delta$ and $\Delta\beta$ are the differences in the real and imaginary part of the refractive indexes n_1 and n_2.

Bilayer materials used in the water-window region are W/B_4C, Cr/Sc, Co/C, Cr/V with the reflectivity between 1 and 15 % [113]. Table 2.1 shows reflection characteristics (calculations and experiment) of normal incidence multilayer mirrors. To have a comparison with EUV range; Mo/Si multilayer mirror has a measured reflectivity 70 % [114].

Table 2.1: Reflection characteristics (calculations and experiment) of normal incidence multilayer mirrors in the water-window region. Notes: d is the thickness of bilayer, R_{exp} is the measured reflectivity and R_{ideal} is the reflectivity calculated from an ideal surface.

λ (nm)	Material	d (nm)	N	$\lambda/\Delta\lambda$	R_{exp} %	R_{ideal} %	Ref
2.36	W/B_4C	1.17	500	262	0.63	18	[115]
3.14	Cr/Sc	1.56	400	263	15	46	[116]
4.47	Co/C	2.26	200	153	14.8	38	[117]
	Cr/Sc	2.21	200	186	7.5	24	[118]

Multilayer mirrors are used as a condenser optic and were used in several laboratory water-window microscopes [33, 119, 120].

2.4.2 Diffractive optics

Diffraction is generally used to describe the process whereby incident radiation is redirected into relatively well-defined directions by ordered arrays of scatters. The diffraction pattern results from positive interference in certain directions. As a *diffractive optics*, we can understand, mirrors, gratings, etc., where there are features comparable in size to the irradiating wavelength that cause radiation to propagate in directions different from those given by geometrical considerations [28]. Two types of diffractive optics are used in SXR optical systems; linear gratings, on either plane or shaped substrates, and zone plates. The diffraction gratings are used in soft X-ray monochromators and spectrometers, while the zone plates are used in the image-forming system such as microscopes and telescopes [105].

2.4.2.1 Diffraction gratings

To explain the fundamental properties of diffractive optics, one can consider a simple transmission linear grating, as illustrates in Figure 2.12. Constructive interference occurs, in a first-order, at angles where the path length is increased by one wavelength. This occurs for both positive and negative angles, giving rise to the $\pm$1st orders of the grating. Higher orders will be generating at angles θ_m, corresponding to increased path lengths $m\lambda$. For radiation incident on the grating at an angle θ_i, measured from the normal, we obtain the condition for constructive interference as [28]

$$\sin\theta_m - \sin\theta_i = \frac{m\lambda}{d} \tag{2.29}$$

where $m = 0, \pm1, \pm2, \pm3, \ldots$ is the diffraction order, and d is the grating period. This equation is known as the *grating equation*.

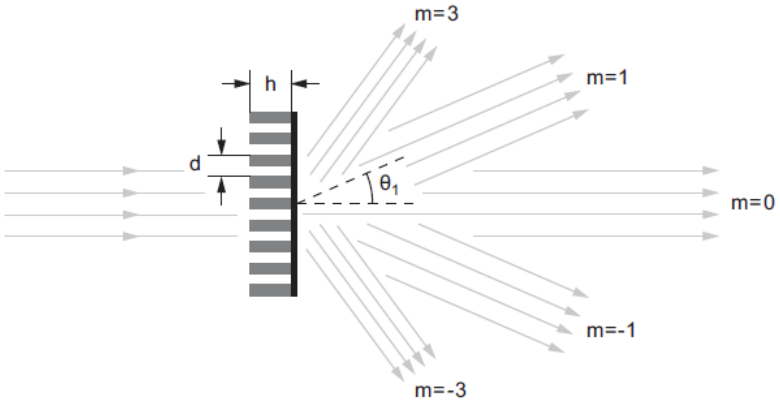

Figure 2.12: Diffraction from a transmission grating. For the clariy, only 0, $\pm 1, \pm 3$ orders are showing. Adopted from [55].

The ratio I_m/I_0 gives the efficiency for a transmission grating. In the case of a grating consisting of opaque lines of width equal to half the grating period, the diffraction efficiency η_m is

$$\eta_m = \begin{cases} 0.25 & m = 0 \\ 1/m^2\pi^2 & m \text{ odd} \\ 0 & m \text{ even} \end{cases} \tag{2.30}$$

For an opaque transmission grating of equally wide lines and spaces, 25 % of the incident energy is in the $0th$ order, approximately 10 % is diffracted to each of the $\pm$1st orders, and so forth, while the grating itself absorbs 50 % of the incident energy [28]. However, the efficiency can be significantly enhanced if the opaque lines are replaced by a translucent phase-shifting material. Ideally, this material should provide a π phase-shift and no absorption, which would increase its efficiency by up to 40 % in the first order [80]. As it is seen from equation 2.30, the efficiency is scaled as $\eta_m \sim 1/m^2$, explaining why the first order is usually used. The theoretical diffraction efficiency of the infinite grating (it includes zone plates) with rectangular zone profiles and $m \neq 0$ [121] is

$$\eta_m = \frac{\sin^2(rm\pi)}{(m\pi)^2}[\, 1 + e^{-4\pi\beta h/\lambda} - 2e^{-2\pi\beta h/\lambda}\cos(2\pi\delta h/\lambda)\,] \tag{2.31}$$

where r is the line-to-space ratio, h is the zone height, and δ and β are the real and imaginary part of the refractive index from equation 2.2.

2.4.2.2 Zone plates

Zone plate, sometimes referred to as Fresnel zone plate [28], can be considered as a circular diffraction grating with radially increasing line density. It consists of series

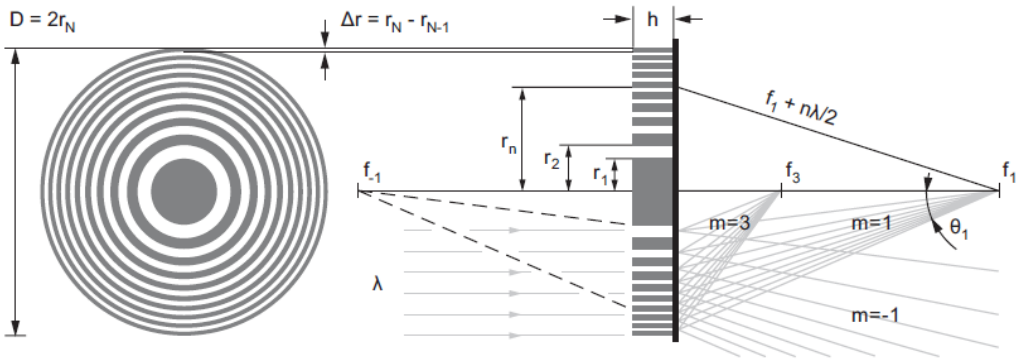

Figure 2.13: The principle of a Fresnel zone plate. Alternate zones are opaque in the simple transmission zone plate. The zone plate is characterized by a total number of zones (N), diameter (D), focal length (f), and numerical aperture (NA). The diffraction-limited resolution is determined by the width of the outermost zone (Δr). Adopted from [55].

of concentric, usually metal, rings alternating with circular slots. Typically, the rings are about equal in width to the slots and are fabricated on a thin membrane [53]. Assuming only the first diffraction order, as the most convenient for the imaging due to the highest diffraction efficiency (see equation 2.30), the constructive interference occurs when the optical path of two consecutive open zones r_n and r_{n+1} to the focal point differ by $n\lambda/2$. Here n represents the index of a zone, going from 1 to N, where N is the total number of zones, and r_n is the radius of the n^{th} zone. The principle of the Fresnel zone plate is illustrated in Figure 2.13. Applying the Pythagorean theorem, the zonal radii are given by

$$f_1^2 + r_n^2 = \left(f_1 + \frac{n\lambda}{2}\right)^2 \Rightarrow r_n = \sqrt{n\lambda f_1 + \frac{n^2\lambda^2}{4}} \tag{2.32}$$

The term $n^2\lambda^2/4$ represents spherical aberration, and f_1 is the focal length for the 1^{st} diffraction order. For the water-window wavelengths, where $f \gg n\lambda/2$ spherical aberration can be neglected and the equation 2.32 for the first diffraction order will be simplified into

$$r_n \simeq \sqrt{n\lambda f_1} \tag{2.33}$$

The diameter of a zone plate can be expressed from the previous equations as

$$D = 2r_N \simeq 4N\Delta r \tag{2.34}$$

where Δr is the width of the outermost zone ($r_N - r_{N-1}$).

From the equations 2.33 and 2.34, the focal length of a zone plate can be expressed as

$$f_1 \simeq \frac{4N(\Delta r)^2}{\lambda} \tag{2.35}$$

This relationship is very important for the design of the zone plate. The focal length will vary directly with the number of zones, with the square of the outermost zone width (which sets the resolution), and inversely with wavelength. Thus the chromatic aberration of a zone plate lens is much larger than that of a refractive lens, and to get a good focus, the zone plate needs to be illuminated by monochromatic light. The required degree of monochromaticity for the achievement of the diffraction-limited resolution is roughly given by [122]

$$\frac{\Delta\lambda}{\lambda} \leq \frac{1}{N} \tag{2.36}$$

where $\Delta\lambda$ is the spectral bandwidth, and N is the total number of zones (opaque and transmissive) in the zone plate.

The numerical aperture (NA) of a lens is defined as NA $\equiv \sin\theta$, where θ is the half angle measured from the optic axis at focus back to the lens, as illustrated in Figure 2.13. Thus the numerical aperture of a zone plate is NA $= r_N/f_1$ and can be expressed as

$$\mathrm{NA} \simeq \frac{\lambda}{2\Delta r} \tag{2.37}$$

Assuming that the number of zones N is sufficiently large that the diffraction pattern at a focus approximates to an Airy pattern, and the first null of one overlaps the peak of the other one (Rayleigh's criterion) then the *Rayleigh resolution* limit is

$$\delta_{Rayleigh} = \frac{0.61\lambda}{\mathrm{NA}} = 1.22\Delta r \tag{2.38}$$

Therefore, the diffraction-limited resolution is independent of wavelength and is determined by the width of the outermost zone. Aberrations such as astigmatism and coma can also limit resolution (this is discussed more in [28, 53]).

The depth of focus (DOF) of zone plate is defined as a distance over which the focus intensity decreases only by 20 % of its maximum [107] and is given by

$$\mathrm{DOF} = \pm\frac{\lambda}{2(\mathrm{NA})^2} = \pm\frac{2(\Delta r)^2}{\lambda} \tag{2.39}$$

Thus for zone plate with larger NA, hence capable of a better resolution, the depth of focus is rapidly decreasing, as it illustrates in Figure 2.14. In microscopes, this also limits the region of a thick sample that is in focus. The efficiency of the zone plate is determined by equation 2.31. Theoretically, efficiencies of about 20 % are reached for Nickel zone thicknesses around 200 nm. This thickness can be achieved for the outermost zone widths of 20–30 nm. Due to fabrication errors, efficiencies of real Ni zone plates are typically up to 10 %–15 % [67]. The calculated diffraction efficiency (according to equation 2.31) for zone plates made of tungsten, gold, nickel,

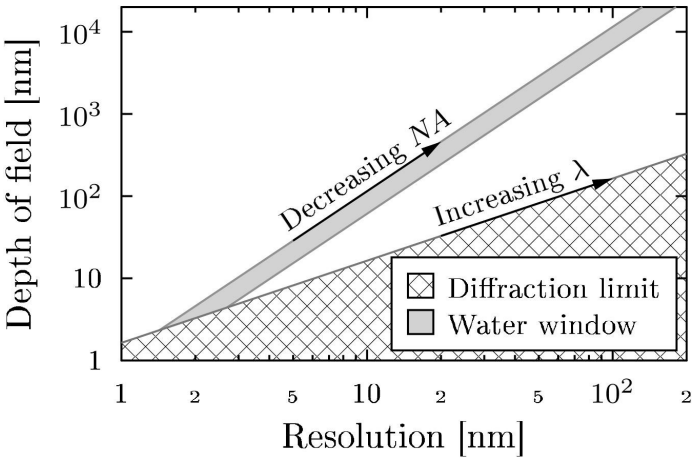

Figure 2.14: The relation between resolution and the depth of field for an ideal lens and monochromatic light. The diffraction limit shown here is defined as $0.61\lambda/NA$ for $NA = 1$. The water window shows accessible resolution and depth of field for soft X-ray energy range. Adopted from [123].

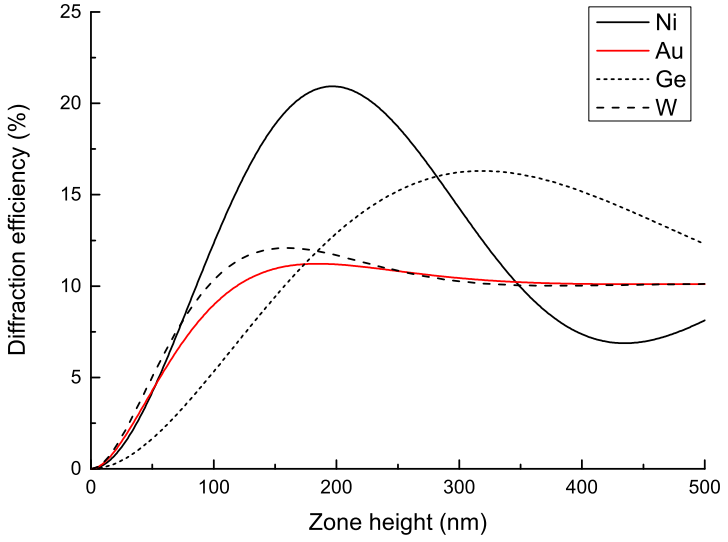

Figure 2.15: The calculated first-order diffraction efficiency depends on zone height for nickel, gold, germanium and tungsten at wavelength of 2.88 nm. Calculation are based on optical data from [51].

and germanium are shown in Figure 2.15.

Zone plates are the most common objective optics in soft X-ray microscopes; however, they were used as a condenser optic too [124], but due to the difficulties in matching the NA of the condenser and the NA of the objective, which is a common practice to achieve resolution according to Rayleigh criterion, zone plate was not used as a condenser. Also, the use of a compound Fresnel zone plate was demonstrated, combining first and third-order in focus, however, the drawback of this technique is a significant limitation of the field of view [125].

3 | Water-window microscopes

As it was discussed in the previous Chapter, soft X-ray radiation is very suitable for microscopy, especially the wavelengths within the water-window spectral region (between the carbon and the oxygen K-absorption edges, 284–543 eV, 4.37–2.28 nm, respectively) are ideal for biological imaging. The benefits of microscopy in the water-window are: 1. Natural contrast. There is no need to insert any fluorescent markers or staining the specimen since the contrast is obtained from the absorption of SXR by the specimen. In the water-window, the organic matter (carbon-rich; proteins, lipids) absorbs photons at an order of magnitude more than water, which creates the contrast. 2. Very low scattering. In the water-window, the scattering process (Compton as well as Rayleigh) are negligible compared to absorption, see Figure 2.3, and the contrast of the in-focus plane is not degraded by scattered light from the other layers of material like in optical microscopy or even in radiography [126]. 3. Penetration. A near absence of SXR reflections at interfaces results in very clear images, even of the thick specimen (up to 10 μm); unlike the electron microscopy, there is no demand for sectioning the eukaryotic cell before imaging. 4. Depth of field. The relatively large depth of focus of low numerical aperture zone plates opens the possibilities to achieve micro-tomography on whole cells [126]. Overall, the soft X-ray microscopy in the water-window with a resolution of a few tens of nm is an emerging imaging technique bridging the gap between optical and electron microscopy.

3.1 Types of soft X-ray microscopes

In this section, the two main techniques for soft X-ray microscopes will be briefly introduced, namely full-field SXR microscopy and scanning SXR microscopy. Additionally, contact SXR microscopy will be mentioned to provide a complex overview of imaging techniques utilizing the water-window wavelengths.

3.1.1 Full-field soft X-ray microscope

Full-field transmission soft X-ray microscope, sometimes abbreviated to TXM, has been pioneered by Schmahl, Rudolph, Niemann, and their colleagues [24] at George-August University in Göttingen, at first using bending magnet radiation at LURE

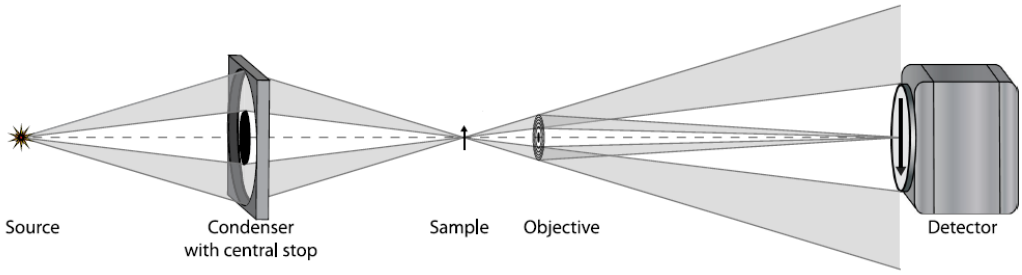

Figure 3.1: Schematic arrangement of a transmission soft X-ray microscope with its most important components: source, condenser, sample, high-resolution objective, and detector. Adopted from [67].

in France, and later at the BESSY synchrotron facility in Berlin [28].

TXMs follow the layout of conventional optical microscopes and transmission electron microscopes, i.e., a condenser focuses the radiation onto an object, the incident soft X-rays pass through the object, where they are partially absorbed with a spatial variation dependent on the atoms present, their distribution, and the wavelength. The emerging radiation is then usually diffracted by a high-resolution zone plate to form a first-order diffraction image on an SXR-sensitive detector. The schematic arrangement of a transmission soft X-ray microscope is depicted in Figure 3.1. As the condenser optics in laboratory microscopes are usually used ellipsoidal mirrors or multilayer mirrors, less frequently the Wolter (type I) mirror, while in the case of synchrotron-like-based microscopes are employed zone plates or crystals [53]. The overview of TXMs based on synchrotron-like facilities is listed in [53]. The state of the art of laboratory soft X-ray microscopes operating in the water-window, including the radiation sources, employed optics, spatial resolutions will be discussed and listed in section 3.4; therefore, it is not mentioned here.

In the TXMs, the contrast mechanisms are either absorption or phase contrast, and the TXMs arrangement does not require the spatially coherent radiation. The other advantages of full-field transmission microscope layout are the highest spatial resolution and shortest exposure time, while contrary to higher radiation dose. For that reason, the cryogenic sample preparation is necessary for 3D tomography imaging to avoid radiation damage.

3.1.2 Scanning soft X-ray microscope

Scanning transmission soft X-ray microscope, sometimes abbreviated to STXM, has been pioneered by Kirz, Rarback, Jacobsen, and colleagues [25] at SUNY Stony Brook and Brookhaven National Laboratory, at first using bending magnet and later undulator radiation at Brookhaven's National Synchrotron Light Source (NSLS) [28].

In this microscope layout, spatially coherent soft X-rays illuminate a zone plate, which forms a first order focal spot at the sample plane. The zone plate creates an Airy pattern focal spot intensity distribution, with a resolution set by the width of

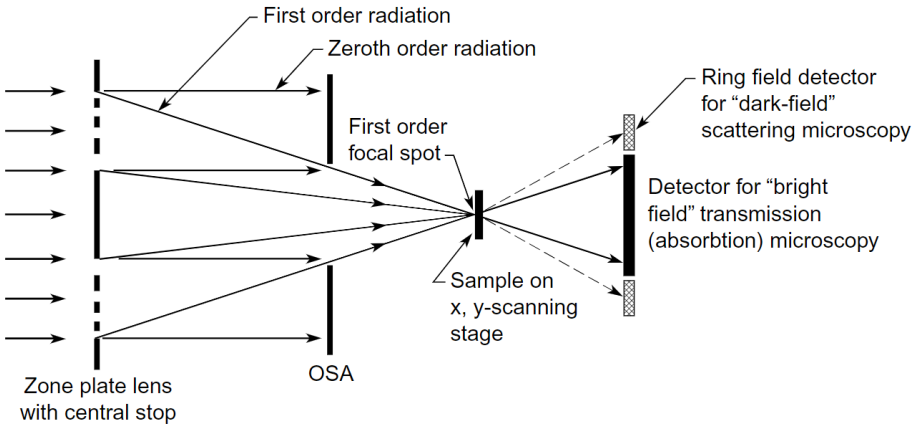

Figure 3.2: The principle of the scanning transmission soft X-ray microscope. A combination of a central zone plate stop and an order sorting aperture (OSA) block all but the first-order diffraction from reaching the sample. Adopted from [28].

the outermost zone. The zeroth and other orders are prevented from reaching the sample by a combination of a zone plate central stop and an order sorting aperture, as shown in Figure 3.2. Thus radiation dose to the sample is minimized [28]. Because of the need to mechanically scan the specimen in most present microscopes, and the need for coherent illumination, imaging times are generally longer, compared to TXMs. The undulator radiation is used as a radiation source. Even a laser-produced plasma source was reported for STXM [127] to demonstrate a proof-of-principle; nevertheless, significant improvements were required to obtain a better quality image, and no progress was reported ever since. The complex overview of STXMs based on synchrotron-like facilities is listed in [53], describing the light source, illumination, and contrast mechanism.

The STXM can operate in several modes. In the transmission mode to record sample absorption versus position, repeated at various wavelengths for elemental and chemical analyses at spectral resolution set by the monochromator. It can also be used in a fluorescence or luminescence mode in which incident radiation excites or indirectly causes the emission of radiation that reveals the chemical nature of the sample, or the presence of special molecular tags, again as a function of scanned position. The third mode of operation is that of detecting photoelectron emission as a function of position. Combining the latter with photoelectron spectroscopy, at each scanned position, provides a powerful tool for the study of surface composition and chemistry [28].

Although the STXMs provide fascinating imaging techniques, currently, they are only used at synchrotron-like facilities, as the laboratory sources do not provide sufficient brightness to allow scanning with acceptable acquisition times.

3.1.3 Contact soft X-ray microscope

Soft X-ray contact microscopy was first developed by Spiller and colleagues at the IBM Thomas J. Watson Research Center [128] and demonstrated using synchrotron radiation in Hamburg (DESY).

Contact microscopy represents the simplest imaging technique among other soft X-ray microscopies, as it requires no focusing optics for the X-rays, neither the monochromaticity of the radiation contrary to the previous types of microscopes, in which the Fresnel zone plate was employed. In contact microscopy, the sample is placed directly on or in close proximity to a high-resolution X-ray sensitive resist (e.g., PMMA; polymethyl methacrylate) and is then irradiated by soft X-rays. The radiation transmitted through the less dense areas of the sample exposes the underlying photoresist causing localized breakages of the polymer chains. This reduces the local molecular weight of the photoresist, resulting in greater solubility in organic solvents and leaving the unexposed areas relatively insoluble. The chemical development results into topography within the photoresist, corresponding to the X-ray dose absorbed by the sample [67, 129, 130]. The working principle is shown in Figure 3.3. The unity magnification image within the photoresist can be viewed by high magnification imaging methods like scanning electron microscopy (SEM) or atomic force microscopy (AFM).

Nowadays, SXR contact microscopy uses laboratory sources as well as synchrotron-like facilities. Several SXR contact microscopes operating in the water-window region were reported [39, 129, 131]. Despite of the above mentioned advantages of contact microscopy—no expensive optics required, monochromatic radiation is not necessary and the spatial resolution is limited in principle by resolution of the underlying photoresists (for PMMA $\sim$ 10 nm [130]—the main drawback of this method is the need of another high-resolution imaging technique to visualize the final imprint

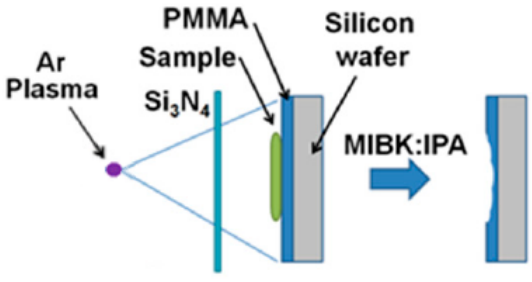

Figure 3.3: The principle of the contact SXR microscope. In this setup, Ar plasma emits SXR radiation, which is filtered by Si_3N_4 filter. After exposure, the photoresist is developed in a solution of methyl isobutyl ketone (MIBK) and isopropyl alcohol (IPA). Adapted from [130].

of the internal structure in the photoresist as well as an irreversible loss of the sample during the chemical development after the exposure. Thus this imaging method partially loses the benefits of biological imaging in the water-window region. For that reason, the contact microscopes will not be included in the state of the art of laboratory water-window microscopes in section 3.4, except one exception to provide a possibility of comparison.

3.2 Image formation

The performance of a linear optical system can be evaluated using Fourier optics. The ability of a single lens or a more complex system to reproduce an image of a (1D or 2D) object can be quantified by decomposing the object in the Fourier series. In Fourier optics, the object is considered as a sum of spatial sinusoidal waves at specific frequencies by analogy with electronics. The imaging systems are supposed to be time-invariant and linear in Fourier optics [132].

Figure 3.4 represents a generalized scheme of an optical system. The object plane is placed at a distance z_0 of the entrance pupil, i.e., the working distance, and the imaging plane at a distance z_i of the exit pupil. The exit pupil (or simply the finite circular pupil function $P(x, y)$) of the imaging system is considered in the following diffraction equations. Gauss approximations are considered, meaning that the incident angles are small and the point light sources are close to the optical axis. Furthermore, the imaging system is assumed to be free of aberration [132].

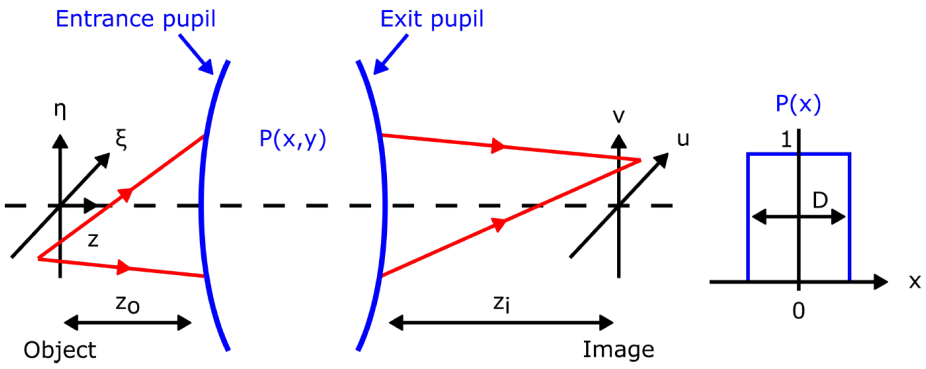

Figure 3.4: Model of an imaging system and representation of its pupil function. The electric field from the emitting point source in the object plane is transmitted by the imaging system in the image plane. The imaging system has a normalized pupil function $P(x, y)$ with a diameter D. ξ and η are the Cartesian coordinates in the object plane. x and y are the Cartesian coordinates in the principal planes of the imaging system. u and v are the Cartesian coordinates in the image plane. z is the optical axis. Adopted from [132].

In the image plane, the 2D complex amplitude distribution of the image of a point light source is represented by a superposition integral,

$$U_i(u,v) = \iint_{-\infty}^{\infty} h(u,v;\xi,\eta) \times U_0(\xi,\eta)\, d\xi d\eta, \tag{3.1}$$

where h is the amplitude at image coordinates (u, v) in response to a point-source object at (ξ,η), and U_0 is the amplitude distribution transmitted by the object. The coordinates u and v are given by $u = M\xi$ and $v = M\eta$, where M is the magnification of the imaging system. Using the convolution theorem, equation 3.1 can be rewritten:

$$U_i(u,v) = h(u,v;\xi,\eta) \otimes U_0(\xi,\eta) \tag{3.2}$$

The amplitude response $h(u,v;\xi,\eta)$ of the imaging system (also called amplitude point spread function) is defined as the Fourier transform of its pupil function $P(x,y)$.

$$h(u,v) = \frac{A}{\lambda z_i} \iint_{-\infty}^{\infty} P(x,y) \times exp\left\{-j\frac{2\pi}{\lambda z_i}(ux+vy)\right\}\, dxdy \tag{3.3}$$

where A is constant amplitude, and $P(x,y)$ is the pupil function with diameter D and is unity inside and zero outside the projected aperture.

Thus in this general case, for a diffraction-limited system, the image can be regarded as being convolution of the image predicted by geometrical optics with an impulse response that is the Fraunhofer diffraction pattern of the exit pupil [133].

In order to determine the irradiance $I_i(u,v)$ recorded by a detector placed in the image plane, the square of the image amplitude is time-averaged.

$$I_i(u,v) = \langle |U_i(u,v)|^2 \rangle \tag{3.4}$$

The comprehensive physics theory related to image formation can be found in [133, 134].

3.2.1 Coherent imaging

The coherent illumination of an object yields an imaging system linear in complex amplitude. The imaging system is found to be described by an amplitude convolution equation. By combining the equation 3.2 and 3.4, the image intensity can be defined as:

$$I_i(u,v) = \langle |h(u,v;\xi,\eta) \otimes U_0(\xi,\eta)|^2 \rangle \tag{3.5}$$

The frequency-domain irradiance is given by:

$$I_i(f_x, f_y) =\propto |P(x, y) \times \mathcal{F}\{U_0(\xi, \eta)\}|^2 \tag{3.6}$$

where f_x and f_y are spatial frequencies corresponding to the x and y coordinates, respectively.

The equation shows that the term of *normalized amplitude transfer function* $H\ (f_x, f_y)$ of the imaging system is its pupil function $P\ (x, y)$.

$$H(f_x, f_y) = \mathcal{F}\{h(u, v; \xi, \eta)\} \tag{3.7}$$

$$\propto \mathcal{F}\{\mathcal{F}\{P(x, y)\}\} \propto P(\lambda z_i f_x, \lambda z_i f_y) \tag{3.8}$$

In the fully coherent case, the frequencies of the entrance object below the cut-off frequency f_c of the imaging system are transferred without any loss of contrast, while the frequencies above the cut-off frequency of the imaging system are not transferred at all (the contrast drops to zero). The cut-off frequency f_c of a perfectly coherent imaging system is defined by:

$$f_c = \mathrm{NA}/\lambda \tag{3.9}$$

However, the value of the cut-off frequency could be slightly reduced as the illumination generated by the real optical sources, including laser, are never perfectly monochromatic [132].

3.2.2 Incoherent imaging

In an entirely incoherent case, no interference can occur, thus using an incoherent illumination, the image formation by the optical system is linear in intensity. The resulting intensity in the image plane is defined as the square of the amplitude spread function $h(u, v; \xi, \eta)$ convoluted at the object irradiance point source:

$$I_i(u, v) = |h(u, v; \xi, \eta)|^2 \otimes |U_0(\xi, \eta)|^2 \tag{3.10}$$

or,

$$I_i(u, v) = |h(u, v; \xi, \eta)|^2 \otimes |I_0(\xi, \eta)| \tag{3.11}$$

The incoherent imaging system transmits the low-frequency object signal keeping the same contrast. However, unlike in coherent imaging, when the frequency of the entrance signal is higher, the contrast of the image is decreased but still resolved by the imaging system.

The *optical transfer function* $OTF\ (f_x, f_y)$ is the normalized autocorrelation function of the amplitude transfer function defined in the incoherent case as

$$OTF(f_x, f_y) = \mathcal{F}\{|h(u, v; \xi, \eta)|^2\} \tag{3.12}$$

$$\propto \mathcal{F}\{|\mathcal{F}\{P(x, y)\}|^2\} \tag{3.13}$$

From the Fourier transform operation, a real and an imaginary parts result, leading to the *modulation transfer function* (MTF) and the *phase transfer function* (PTF).

$$MTF = |OTF| \tag{3.14}$$

$$PTF = angle\{OTF\} \tag{3.15}$$

The PTF is liable for the transversal shift of the image. Whereas, the MTF represents the contrast (or the visibility) distribution ratio between the image with the object at a given spatial frequency f_x, f_y.

The cut-off frequency f_c of the transfer function in incoherent imaging is given by:

$$f_c = 2\mathrm{NA}/\lambda \tag{3.16}$$

All the imaging systems mentioned in this section (coherent and incoherent) were assumed to be free of aberrations, i.e., a diffraction-limited optical system. Aberrations cannot increase the contrast of any spatial frequency component of the image, and in general, will lower the contrast. However, the absolute cut-off frequency remains unchanged, but severe aberrations can reduce the high-frequency portions of the OTF to such an extent that the effective cut-off is much lower than the diffraction-limited cut-off [133].

3.2.3 Partially coherent imaging

In the previous sections, the fully coherent and entirely incoherent imaging systems were described. The coherent imaging systems have higher contrast at the cost of lower resolution, while the incoherent imaging systems have higher resolution at the cost of lower contrast. In practice, most of the soft X-ray microscopes are neither coherent nor incoherent. The degree of the coherent depends on its optical design and affects how the images are formed. It relates to the imaging properties such as resolution, contrast, and depth of focus [55].

For transmission soft X-ray microscopes, the ratio between the numerical apertures of condenser and objective yields the coherence factor σ (in some literature marked by m), which quantifies the *degree of coherence* in the microscope object plane.

$$\sigma = \frac{\mathrm{NA}_{condenser}}{\mathrm{NA}_{objective}} \tag{3.17}$$

Full coherence is represented by $\sigma = 0$, and complete incoherence by $\sigma \to \infty$, although $\sigma = 1$ is usually sufficient to get close to fully incoherent behavior [122]. The cases when the degree of coherence is between 0 and 1 are described as partially

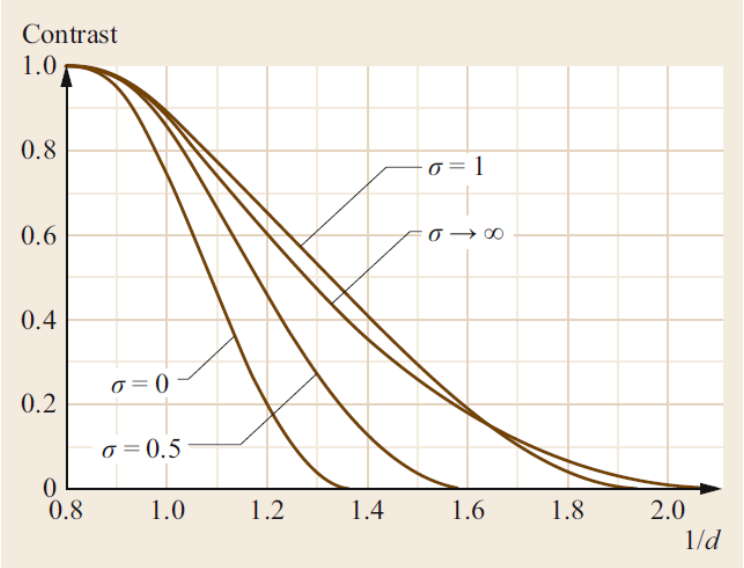

Figure 3.5: Image contrast as a function of $1/d$, where d is the point separation of a two-point object imaged by a lens with a circular pupil and coherence parameter σ equal to 0 (coherent case), 0.5, 1, and ∞ (incoherent case). d is expressed in units of λ/NA. Note that the Rayleigh resolution corresponds to 15.3% intensity contrast (defined as $(I_{max} - I_{min})/(I_{max} + I_{min})$), which is the same as 26.5% amplitude modulation. It occurs at $d = 0.61\lambda$/NA for both $\sigma = 1$ and $\sigma \to \infty$. Adopted from [122].

coherent. Figure 3.5 illustrates the influence of the degree of coherence on the image contrast in the dependence of the separation of a two-point object imaged by a lens.

The influence of coherence on the image formation is shown in Figure 3.6, proving the theory that the coherent imaging systems have higher contrast compared to the incoherent imaging systems that provide a better resolution.

Theory for the partially coherent imaging systems was enhanced in the group of Prof. Hertz. Simulation of partially coherent image formation in a compact soft X-ray microscope was in 2D introduced by Olov von Hofsten *et al.* in [135] and

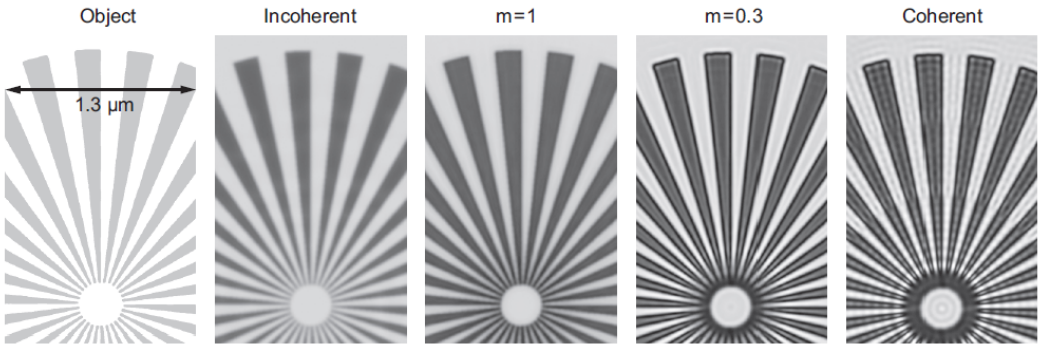

Figure 3.6: Influence of coherence on image formation. Simulated images of a 100 nm thick Ni Siemens start object with a 30 nm zone plate for different degree of coherence. The inner period corresponds to the Rayleigh resolution. Adopted from [55].

extended to thick objects by propagating the electric field through an object, but with a 2D treatment of the wave-propagation process [136]. A 3D wave-propagation-based model for the image formation process in transmission, partially coherent soft X-ray microscopes with thick 3D object, was introduced by Selin *et al.* in [137]. Their model consists of three steps: decomposition of the illumination into plane waves, propagation of each plane wave through the object, and imaging by the objective. The propagation through the sample is based on the parabolic wave equation (PWE). The validation of this model was done by comparing the simulation and experimental results with an excellent agreement. For more theory of this model, please see [137].

3.3 Development of water-window microscopy

X-ray microscopes have been used for material science research since the 1940s [29, 110]. For soft X-rays, significant progress towards nanoscale imaging began in the 1970s and 1980s with the work of Schmahl and colleagues, who pursued the development of full-field transmission X-ray microscopy [24], and Kirz and colleagues, who investigated scanning transmission X-ray microscope [138]. Both groups employed zone plate optics and synchrotron radiation. Spatial resolutions were around 100–200 nm in this early time, moving towards to 50 nm in the late 1980s [139].

Major advantages of this technique were: it provides a unique set of capabilities to cover the gap between the optical and electron microscopy [140, 141] and allowed to image a relatively thick (up to 10 μm) samples at high resolution in the wet conditions without the necessity of external contrast-enhancing agents [27, 141].

The improvement of the spatial resolution continued in the 1990s and approached to 30 nm [141]. During mid- 1990s the first effort to develop a compact laboratory-scale source, so-called "table-top" appeared, and few attempts have been made to develop a compact nonsynchrotron-based water-window transmission X-ray microscope [31]. In 2001, the first laboratory soft X-ray microscope with subvisible resolution using a liquid-jet-target laser-plasma source was introduced by Hertz and coworkers at the Royal Institute of Technology (KTH) in Stockholm [31]. In the 2000s other table-top sources based on laser-produced plasma for SXR microscopy were reported with the spatial resolution under 60 nm [87, 124].

Up to date considerable progress has been made in the field of the compact sources and SXR microscopy as well. Compact SXR microscopic systems based on laser-produced plasma sources using—liquid-jet target [31–33], gaseous target [34, 35], double-stream gas target [36–38], or ultra-thin metal target [39]—were developed. The second branch of laboratory-scale SXR microscopes is based on discharge-produced plasma sources using pseudo spark like electrode geometry [40], an electrode-less design (Energetiq, Inc.) [41, 42], or Z-pinching capillary discharge

[43, 44]. A compact transmission SXR microscope based on an electron-impact source, utilizing the oxygen K-alpha emission line at 525 eV (2.36 nm), was reported [102]. Nevertheless, the reported photon flux of these sources is about a few orders lower compare to laser-produced and discharge-produced plasma sources. Coherent laboratory sources such as plasma-based X-ray lasers (XRLs), sources based on high harmonics generation (HHG), or betatron radiation produced by laser-wakefield accelerators (LWFAs) are due to the high spatial coherence more suitable for other imaging techniques than transmission water-window microscopy, such as coherent diffraction imaging, ptychography, etc. [67]. The main limitations of using coherent sources for the transmission water-window microscopy are the huge and expensive pump lasers in the case of XRL and LWFA, and low flux in the case of HHG [142, 143]. However, a newly developed TW-class mid-infrared laser, together with a loose focusing geometry for HHG, resulted in increased photon flux, opening a new possibility for the transmission water-window imaging [144]. However, the laser-produced and discharge-produced plasma sources remain the more compact solution. The up-to-date overview of laboratory water-window X-ray microscopes is described in the section 3.4.

Even though table-top sources are accessible and easy to operate, they come with their limitation in terms of exposure times and in order to get comparable spatial resolution with large-scale facilities. To improve the brilliance of the compact sources, a jet with a so-called barrel shock system was introduced [45], enhancement of the soft X-ray radiation by inserting a low-pressure nitrogen atmosphere to increase the conversion efficiency of laser-produced plasma sources was demonstrated [46, 47]. Nevertheless, future development of laboratory-scale sources is necessary to perform a single-shot imaging experiment as the photon flux of these sources is a few orders of magnitude below the requirements for a single shot imaging micrometer-sized specimen [48]; a current perspective of a single shot imaging using compact SXR sources is discussed in [48]. At the present time, there are three cryogenic soft X-ray microscopes using table-top sources. The first two make use of a liquid-jet high-brightness laser-plasma source to acquire images with high quality in 10–30 seconds [32] (Stockholm microscope) and a few minutes in the Berlin microscope. Whereas the third one uses a Z-pinch source [41] capable of a single image acquisition in 30 seconds [145]. Even the integration of a laboratory soft X-ray microscope with a visible light microscope was introduced in 2020 [146].

Nowadays, the soft X-ray microscopic images captured by employing the Fresnel zone plate as the objective optics with 10 nm spatial resolution have been presented [26], and tomography technique is in a great interest [27, 29, 71]. There are currently four cryo soft X-ray tomography microscopes installed, operational and actively studying biological samples at synchrotrons worldwide including the Advanced Light Source (ALS) in Berkeley (CA, USA), BESSY II in Berlin (Germany),

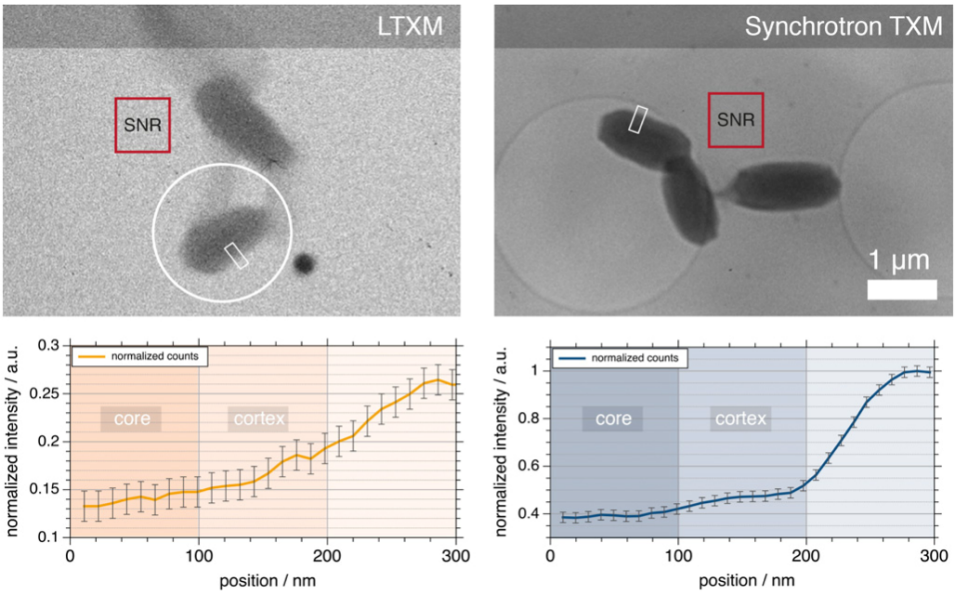

Figure 3.7: Comparison of the signal-to-noise ratio (SNR) of laboratory (left) and synchrotron (right) transmission X-ray microscopy measurements of dormant *B. subtilis* bacterial endospores. Exposure times were 8 min for the LTXM image and $\leq$ 1 s for the synchrotron image. Below each micrograph normalized intensity plots (area indicated by white rectangle) averaged over 11 pixels are shown. The area of the SNR measurement is indicated by red squares. $SNR_{LTXM} \approx 14$, $SNR_{SynchTXM} \approx 45$ [149].

ALBA in Barcelona (Spain) and the Diamond Light Source in Didcot (UK) [71]. Furthermore, three other synchrotron-based soft X-ray tomography beamlines are under construction, i.e., the Taiwan Photon Source in Hsinchu (Taiwan), the Shanghai Synchrotron Radiation Facility in Shanghai (China) and the Canadian Light Source in Saskatoon (Canada) [147]. However, as the spatial resolution increases, the depth of field (DOF) decreases. The DOF for a 10 nm objective zone plate (ZP) is in the region of 500 nm to 2 μm. This DOF is smaller than most cells, certainly almost all eukaryotic cells. But, the limitations imposed by a shallow DOF could be overcome by collecting through-focus data. Consequently, work is now underway to develop imaging acquisition and data processing strategies that permit use of enhanced resolution ZPs [148].

Figure 3.7 illustrates a difference between images of bacterial endospores of *Bacillus subtilis* taken by synchrotron and laboratory-based soft X-ray microscope in 2015. Figure 3.8 shows the progress of the dry imaging of the *Bacillus subtilis* and the image of diatoms captured by the Berlin microscope, reported in 2020. The most significant progress is the decrease of the exposure time by a factor of four.

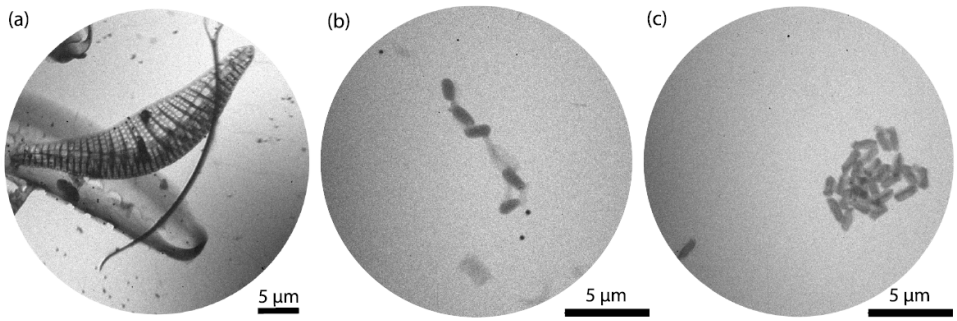

Figure 3.8: Dry imaging with laboratory soft X-ray microscope. **(a)** Diatoms, exposure time 60 s. *Bacillus subtilis* endospores **(b)** before and **(c)** after high-pressure treatment (exposure times 120 s and 180 s). Images from the Berlin microscope. Adopted from [67].

3.4 State of the art of laboratory water-window microscopes

Although the major part of soft X-ray (SXR) microscopes is based on large-scale facilities as a synchrotron, in this review, only the compact, laboratory-scale soft X-ray microscopes operating in the water-window region are taking into account. This review aims to provide information about the current state of the art of table-top water-window microscopes, including the description of their sources, employed optics, and finally, to list the achieved spatial resolution of these compact microscopic systems. In this overview, only the full-field transmission water-window microscopes are mentioned; as was discussed in the previous section (3.1), neither the scanning transmission SXR microscopes are included, as the laboratory SXR sources do not have the sufficient brightness to allow scanning with acceptable exposure times, nor the contact SXR microscopes are mentioned because of the necessity of another high-resolution imaging technique for the visualization of the sample (see 3.1.3). However, the parameters of one laboratory compact SXR microscope are listed to provide a possibility of comparison. The working principle and theory of laser-produced and discharge-produced plasma sources and electron-impact sources are described in the previous section 2.3.2. Therefore, here are presented only the parameters of these sources. As theory and working principle of the soft X-ray optics, i.e., condenser and objective optics, were discussed previously (2.4) too, thus they are not mentioned here.

Table 3.1 provides the overview of laboratory-scale soft X-ray microscopes based on laser-produced plasma (LPP) sources. The microscopes in Göttingen (Laser-Laboratorium Göttingen, Germany) and Warsaw (Military University of Technology (MUT), Poland) utilize gas-puff target, double-stream gas-puff target, respectively. While the microscope in Stockholm (Royal Institute of Technology (KTH) in Stock-

holm, Sweden) and a sister microscope in Berlin (Berlin Laboratory for Innovative X-Ray Technologies (BLiX) at the Technical University of Berlin, Germany), and in Wonkwang (Korea) use the liquid-jet target. The contact microscope based on solid-target plasma source is listed at the bottom line of Table 3.1. Even though the solid-target plasma sources provide the highest photon flux of LPP systems (1.3×10^{15} photons / (sr $\times$ pulse)) [95], they produce a significant amount of debris, making them difficult to use in microscopy for an extended period, especially in combination with sensitive optics. For that reason, no full-field SXR microscope based on a solid-target plasma source was demonstrated. On the contrary, the liquid- and gas- target plasma sources offer a very low-debris operation. The plasma is induced exclusively by the Nd:YAG laser in all full-field SXR microscopes, operating in order of a few Hz in the case of the gas-puff target (due to the necessity of an injection of pressurized gas into a vacuum chamber (i.e., puff)). In the case of the liquid-target, the repetition rate of the laser is up to several kilohertz, although it requires a high stability jet.

Table 3.2 summarizes parameters of the table-top discharge-produced plasma sources that were reported and optimized as a potential source for SXR microscopy in the water-window spectral region; however, only two laboratory microscopic systems based on this type of source were reported—Table 3.3—(except the one that is the subject of this doctoral thesis). One operating microscope is in Aachen (Fraunhofer Institute of Laser Technology, Germany), the second is located in the USA (University of California, CA, USA) based on an electrode-less Z-pinch design, the technology developed by Energetiq (MA, USA). The benefit of Energetiq source is the removal of an issue of melting electrodes and producing debris by generating the pinch via magnetic inductive coupling instead of electrodes [41]. The discharge produced plasma (DPP) sources have a larger source size than the LPP sources. As the gaseous target is exclusively used nitrogen for its quasi-monochromatic radiation at 2.88 nm.

To provide a complex overview of table-top, full-field SXR microscopes, electron-impact sources utilized for water-window microscopy are mentioned, together with parameters of the microscope based on this type of source; Table 3.4. The X-ray is generated by an electron beam from an electron gun impinging on the anode target (Cr_2O_3). Nevertheless, the spatial resolution and image contrast are insufficient for cellular level observation of bio-medical samples [102]. For that reason, it is not included in the following paragraphs.

Currently, the Fresnel zone plate is used exclusively for objective optics in all laboratory full-field SXR microscopes. The desktop SXR microscopy systems based on LPP and DPP sources offer a spatial resolution in the order of few tens of nanometers, making them suitable to study objects at the cellular level. Up to date, a cryo

stage was implemented into three laboratory water-window microscopes (Stockholm, Berlin, and USA (Energetiq)). The Stockholm microscope is capable of capturing an image with high quality in 10–30 seconds [67], the Berlin microscope in a few minutes [67] and the Energetiq microscope is capable of single image acquisition in 30 seconds [145]. These microscopes demonstrated imaging with early synchrotron-like quality and acceptable exposure times, allowing unique and relevant biological imaging.

If someone was interested in the development of Stockholm microscope see [31] (2002), [124] (2007), [32, 150] (2012), [96] (2015), [119] (2017), [151] (2019), [67] (2020), and Warsaw microscope see [88] (2010), [152] (2012), [111] (2013), [36, 108] (2015), [130] (2017), [38] (2019), [153] (2020).

Table 3.1: Parameters of laboratory water-window microscopes based on laser-produced plasma sources.

λ (nm)	Source	Target	$\lambda/\Delta\lambda$	Photon flux ph./(sr × pulse)	Source size (μm)	Ref.
2.88	Nd:YAG 1064 nm 10 ns, 600 mJ, 5 Hz	Nitrogen gas-puff	-	6.11×10^{11}	240 × 440	Göttingen [34,91,154]
2.88	Nd:YAG 1064 nm 3 ns, 7.4 J, 10 Hz	Nitrogen double stream gass-puff	-	-	310 × 470	Warsaw [108, 153]
2.88	Nd:YAG 1064 nm 800 ps, 40 mJ, 300 Hz	Nitrogen liquid jet	1000	4×10^{11}	20	Wonkwang [87]
2.48	Nd:YAG 1064 nm 500 ps, 100 mJ, 1.3 kHz	Nitrogen liquid jet	500–1000	10^{12}	18 × 45	Berlin [33,67,146]
2.48	Nd:YAG 1064 nm 500 ps, 100 mJ, 2 kHz	Nitrogen liquid jet 40-60 m/s	500–1000	10^{12}	20 × 30	Stockholm [32,67,151]
‡	Nd:glass 1053 nm 600 ps, 15 J	Au film target	-	1.3×10^{15}	50	Contact [39, 95]

Resolution (nm)	Optics	Ph. flux at sample plane ph./(μm^2× pulse)	Ref.
$\sim$ 50	ellipsoidal condenser mirror and ZP Δr = 25 nm	5.8×10^3	Göttingen [34, 154]
60	ellipsoidal condenser mirror and ZP Δr = 30 nm	5.4×10^4	Warsaw [108, 153]
sub 50	ellipsoidal condenser mirror and ZP Δr = 35 nm	-	Wonkwang [87]
26	spherical multilayer Cr/V condenser mirror and ZP Δr = 25 nm	10^6 †	Berlin [33,67,146]
25	spherical multilayer Cr/V condenser mirror and ZP Δr = 30 nm	-	Stockholm [32,67,151]
sub 100	None	4.4×10^5	Contact [39, 95]

†Photon flux at sample plane per second

‡Contact microscope (λ = 2.3 – 4.4 nm)

Table 3.2: Parameters of table-top discharge-produced plasma sources suitable for water-window microscopy.

λ (nm)	Source	Gas	$\lambda/\Delta\lambda$	Photon flux ph./(sr × pulse)	Source size (μm)	Ref.
2.88	0.48 J/pulse 3 kHz	Nitrogen	-	-	700	France [98]
2.88	0.5 J/pulse 600 Hz	Nitrogen	-	-	<1000	Chile [155, 156]
2.88	20 J/pulse 1 kHz	Nitrogen	840	4×10^{13}	1175	Aachen [157]
2.88	0.4 J/pulse 2 kHz	Nitrogen	-	-	800	Energetiq [41]
2.88	82 J/pulse 3 Hz	Nitrogen	-	5.5×10^{13}	360	Kladno [158, 159]

Table 3.3: Parameters of laboratory water-window microscopes based on discharge-produced plasma sources.

Resolution (nm)	Optics	Ph. flux at sample plane ph./($\mu m^2 \times$ s)	Ref.
40	ellipsoidal condenser mirror and ZP Δr = 30 nm	5×10^6	Aachen [157]
50	elliptical condenser mirror and ZP Δr = 25 nm	-	Energetiq [41, 42]

Table 3.4: Parameters of the electron-impact sources and laboratory water-window microscope based on that source.

λ (nm)	Source	Target	$\lambda/\Delta\lambda$	Photon flux ph./(sr × **s**)	Source size (μm)	Ref.
2.36	30 kV e-gun	water-jet	175	3.2×10^{12} *	21 × 17	Sweden [103, 104]
2.36	15 kV e-gun	Cr_2O_3	-	7×10^{10}	2 × 5 mm	Japan [102]

Resolution (nm)	Optics	Ph. flux at sample plane ph./(μm^2)	Ref.
$\sim$ 1000	Wolter type I mirror as condenser and objective	-	Japan [102]

*Note: Photon flux of the source for e-beam power 120 W (per sr per second)

4 Investigation of table-top soft X-ray sources

This Chapter describes the investigation of two compact SXR sources in possession of Czech Technical University in Prague. Both plasma sources, namely the gas-puff target source and Z-pinching capillary discharge source, are eligible for SXR microscopy in the water-window spectral region. Diagnostics measurements were performed to characterize both sources and to provide their qualitative comparison. The results of these measurements and the experimental implementation are presented in the following sections, including the description of diagnostic instruments.

4.1 Diagnostic instruments

4.1.1 Soft X-ray photodiode

The temporal profile of SXR pulse was measured with a high-speed SXR-sensitive photodiode AXUV20HS1 (Optodiode, USA) in photoconductive mode with a reverse bias of 150 V. A titanium foil (Lebow, USA) with a thickness of 500 nm was used as an SXR band-pass filter to separate the spectral line $\lambda = 2.88$ nm. An aperture with a diameter of 1 mm determines the solid angle of the SXR radiation cone. The schematic layout of the photodiode detector is depicted in the subsections "Temporal profile of the SXR emission pulse" in the sections "Gas-puff target source" and "Z-pinching capillary discharge source," respectively, as the distances between plasma source and photodiode vary for each source. The physical parameters of the photodiode assembly are shown in Figure 4.1.

Another ultra-high-speed SXR-sensitive photodiode AXUVHS6 (Optodiode, USA) was used to verify the correctness of the measurements. Again, a titanium filter with a thickness of 400 nm was employed to separate the spectral line at 2.88 nm. An aperture with a diameter of 600 μm (SPI Supplies, USA) defines the solid angle of the SXR radiation cone. The photodiode was mounted in the SMA connector with a reverse bias of 30 V delivered by a battery pack to reduce the electromagnetic noise. The photograph and the physical parameters of the photodiode detector assembly are depicted in Figure 4.2.

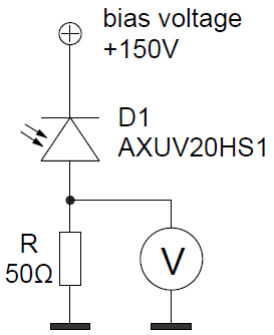

Figure 4.1: Electrical wiring diagram of the photodiode AXUV20HS1 detector.

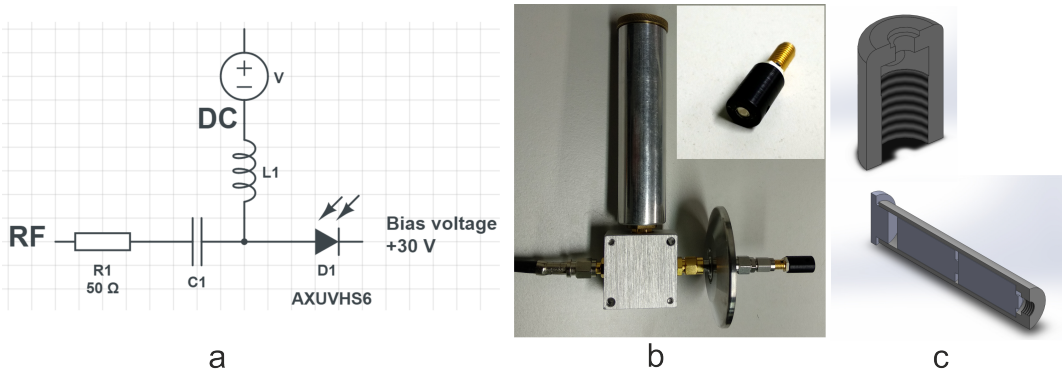

Figure 4.2: **(a)** Electrical wiring diagram of the photodiode detector AXUVHS6. **(b)** Photograph of the photodiode detector and a detail of the photodiode with a "cap". **(c)** Top: A cross-section of the "cap" where the aperture with the Ti foil is. Bottom: A cross-section of the battery holder.

4.1.2 Pinhole camera

The spatial distribution of nitrogen plasma was obtained using a 0.75× (3.7×) magnifying pinhole camera (Laser-Laboratorium Göttingen, Germany) with a 30 μm diameter pinhole and equipped with 200 nm (500 nm) thick titanium filter. The emission profile was recorded onto YAG:Ce coated CCD camera LU165M (Lumera, Canada) with resolution 1392 × 1040 pixel of size 6.45 × 6.45 μm.

4.1.3 Soft X-ray spectrometer

The emission spectra of the SXR radiation were measured by a spectrometer with a free-standing Si_3N_4 transmission grating as a dispersion element. The diffraction grating has 10.000 grooves/mm (i.e., a period of 100 nm). Time-integrated spectra were captured by an SXR-sensitive back-illuminated CCD camera (X-vision M25, Rigaku Innovative Technologies) cooled to -20 °C. The pixel size was 24 × 24 μm, and the image area dimension was 12.3 × 12.3 mm. The spectral response of the CCD is 0.05–5.0 keV, and the dynamical range 20000:1. This spectrometer was used to measure spectra from nitrogen discharge-produced plasma source. The aperture with a diameter of 75 μm was placed near the capillary exit. The distance between

the source (aperture) and the grid was 80 cm. A 80 μm slit was placed in front of the grating, which was 55 cm from the CCD chip. The CCD camera was placed behind a metallic bellow on a moving arm. The target spectral range was selected by setting an angle between the grating and the CCD perpendiculars. The measured spectra resolution was 0.03 nm.

4.2 Gas-puff target source

4.2.1 Experimental implementation

This laser-produced plasma (LPP) source was developed in Laser-Laboratorium Göttingen e.V., Germany. The plasma is formed by the inverse bremsstrahlung [160] of a pulsed IR laser (SpitLight 600, Innolas Laser GmbH, Germany) radiation in the nitrogen gas-puff target with a density of 3.7×10^{-4} g/cm^3. The gas-puff target is produced by the pulsed injection of pressurized (13 bar) gaseous nitrogen by a high-pressure piezoelectrically actuated valve (P286, PI GmbH, Germany) through a conical tungsten nozzle into the focus of the IR laser beam. The Q-switched Nd:YAG laser operates at 1064 nm wavelength with a repetition rate of 2 Hz; other parameters of the laser are listed in Table 4.1. The beam is focused onto a 60 μm diameter spot using a 100 mm focal length lens. Petr Bruza optimized the time delay between the laser pulse and the piezo-valve driving signal with regard to the highest possible photon flux and shot-to-shot stability, finding the best results with 1150 μs delay. The temporal profile of laser pulse was observed by InGaAs photodiode detector (DET01CFC, Tholabs, Germany). The schematic of the experimental setup of the source is shown in Figure 4.3 [58].

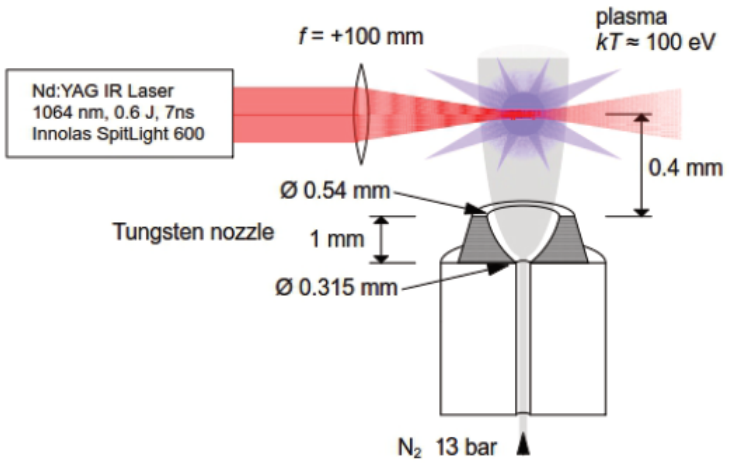

Figure 4.3: Schematic of the experimental setup of the gas-puff target laser-produced plasma soft X-ray source. Adapted from [58].

Table 4.1: Parameters of Nd:YAG laser SpitLight 600.

Parameter	Value
Wavelength	1064 nm
Output energy	640 mJ
Pulse duration (FWHM)	7 ns
Beam radius	3 mm

Series of measurements were performed to verify the nominal output energy of Nd:YAG laser. The output energy of the Nd:YAG laser was measured by the energy sensor J25LP-YAG (Coherent, USA), 7 cm away from the laser head. These experimental measurements confirmed that the nominal value corresponds to the tabulated one, as illustrated in Figure 4.4.

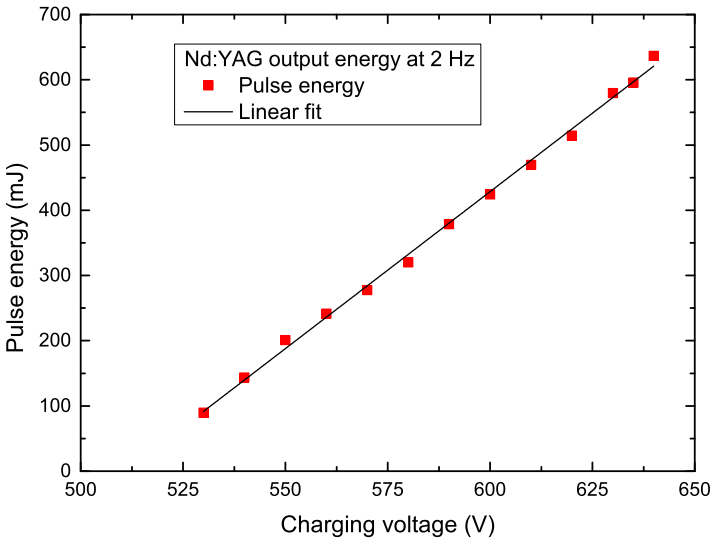

Figure 4.4: Pulse energy dependence on the charging voltage of the flash-lamp for the Nd:YAG laser with a repetition rate of 2 Hz.

Also, the pulse duration of Nd:YAG laser was verified. The experimental data show an agreement with the tabulated value, i.e. ∼7 ns (FWHM) for the flash-lamp voltage of 640 V. In general, for a higher excitation charging, the pulse duration is shorter with an exponential decrease, as demonstrated in Figure 4.5.

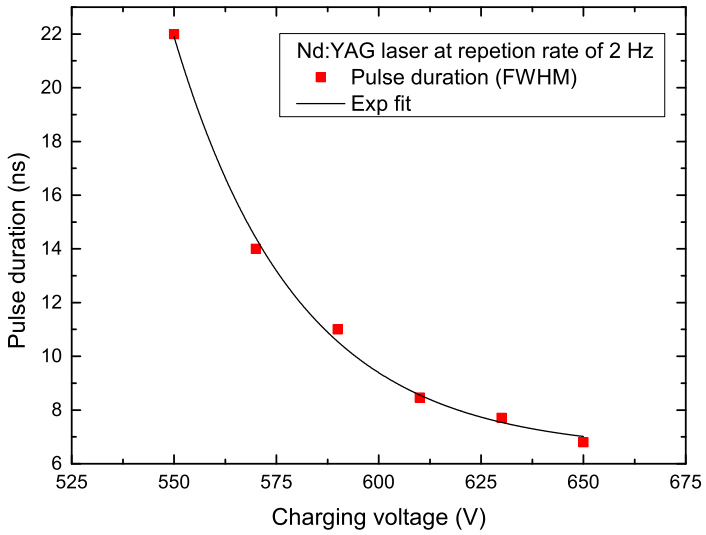

Figure 4.5: Pulse duration dependence on the charging voltage of the flash-lamp for the Nd:YAG laser with a repetition rate of 2 Hz.

4.2.2 Temporal profile of the SXR emission pulse and photon yield

The temporal profile of the soft X-ray pulse was measured with a high-speed SXR-sensitive photodiode (mentioned in detail in section 4.1). The schematic layout of the measurement is depicted in Figure 4.6. A typical temporal profile of SXR emission pulse for nitrogen laser-produced plasma source is shown in Figure 4.7.

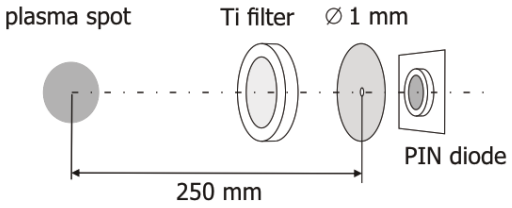

Figure 4.6: Schematic of temporal pulse profile measurement for the LPP source.

As the most crucial microscopy parameter, the photon flux of the source was calculated by numerical integration of 100 single-shot SXR pulses. Figure 4.8 represents the photon flux dependence on laser energy, and Figure 4.9 illustrates the length of the SXR pulse at FWHM in dependence on laser energy. The conditions of measurements were: 425–640 mJ Nd:YAG pulse energy, 2 Hz repetition rate, chamber pressure 10^{-1} Pa, and nitrogen pressure 13 bar.

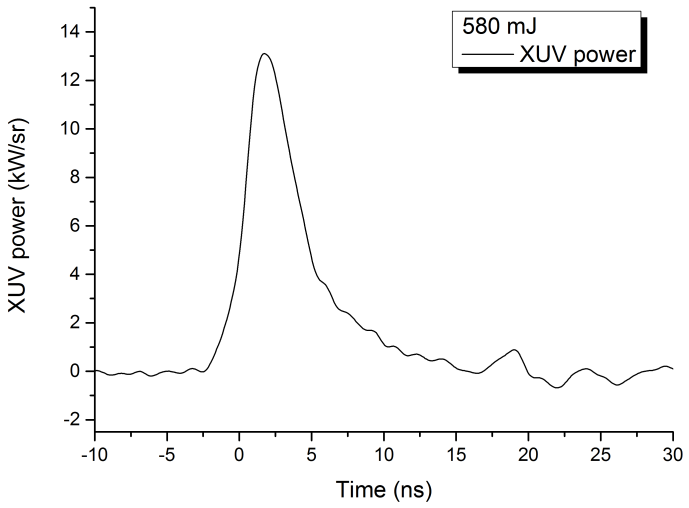

Figure 4.7: A typical temporal profile of SXR pulse of nitrogen laser-produced plasma source for Nd:YAG output energy 580 mJ.

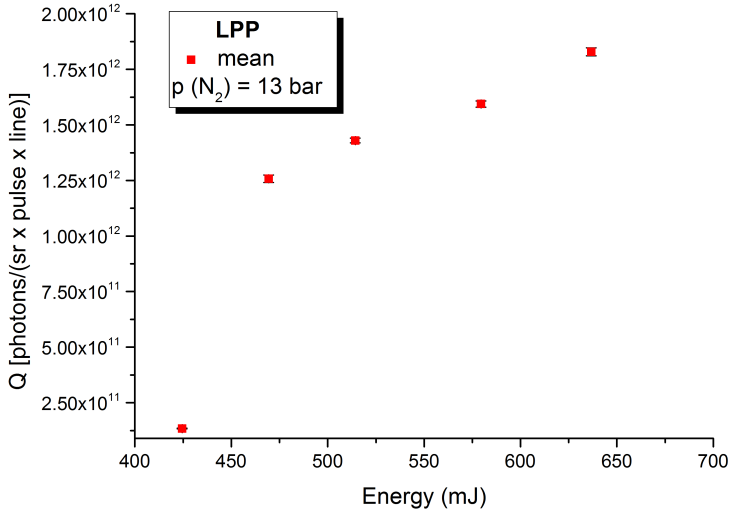

Figure 4.8: Photon flux dependence on output laser energy for nitrogen laser-produced plasma source. Nitrogen pressure: 13 bar.

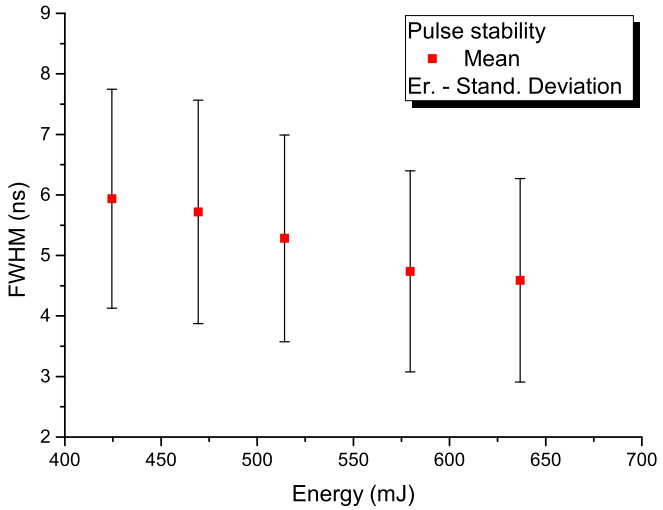

Figure 4.9: Soft X-ray pulse duration at full-width half-maximum depending on output laser energy.

The maximal photon flux of nitrogen laser-produced plasma source is 1.8×10^{12} photons per steradian per pulse, which corresponds to energy 0.12 mJ per steradian per pulse for laser output energy 640 mJ. The overview of measured parameters is shown in Table 4.2.

Table 4.2: Radiance overview of nitrogen laser-produced plasma source.

Parameter	Value
Photon flux per sr per pulse	1.8×10^{12} photons
Energy/(pulse per sr)	0.12 mJ
Source efficiency	1.875×10^{-4}
Peak power per sr	17.6 kW

4.2.3 Spatial distribution of the SXR radiance

The spatial distribution of nitrogen (N_2) SXR radiation emission is shown in Figure 4.10. The profile was acquired by the integration of 100 single-shot images. Nitrogen plasma has an elongated shape with dimensions of 0.2 × 0.4 mm. Conditions of measurement were: Nd:YAG output energy 640 mJ, 2 Hz repetition rate, chamber pressure 10^{-1} Pa, and nitrogen pressure 13 bar.

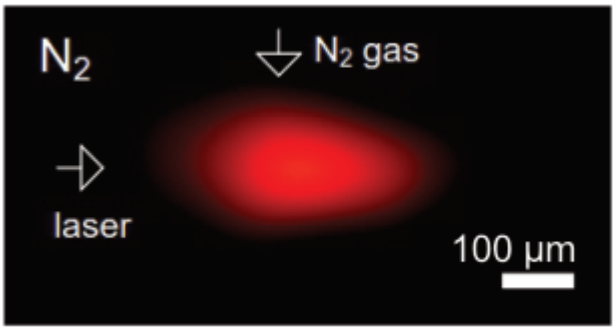

Figure 4.10: Spatial distribution of soft X-ray emission from laser-produced plasma in nitrogen gas-puff target [58].

4.3 Z-pinching capillary discharge source

4.3.1 Experimental implementation

This discharge-produced plasma (DPP) source was developed at Czech Technical University in Prague in the cooperation of the Faculty of Nuclear Sciences and Physical Engineering (FNSPE) and Faculty of Biomedical Engineering (FBME). Plasma is generated by a current discharge through a 10 cm long, 3.2 mm inner diameter ceramic capillary (Al_2O_3) filled with nitrogen gas. A ceramic capacitor bank with a maximum capacity of 21 nF is pulse charged by a two-stage Marx-Fitch generator up to 100 kV and switched by self-breakdown spark-gap. The discharge voltage is regulated by nitrogen pressure in the spark-gap and by Marx-Fitch generator charging voltage. Before the main discharge, a 20–35 A, 3 μs long current pulse pre-ionizes the gas in the capillary and prepares a uniform conducting channel. The main current has a damped sinus shape, with a half-period of 150 ns and maximum amplitude of ∼30 kA. The capillary is filled with nitrogen gas through a hollow in the electrode on its grounded side. Radiation is also emitted through this hole. An aperture, 0.8 mm in diameter, is 3 mm from the capillary exit, separating the discharge gas with a working pressure of 10–500 Pa from the vacuum with three orders lower pressure. The system is enclosed in duralumin housing in order to reduce electromagnetic noise. Biodegradable oil is used to isolate the circuit and avoid unwanted breakdowns [161]. Figure 4.11 depicts the schematic of the source and the charging circuit and Figure 4.12 shows the inner view of the charging circuit. The charging voltage was measured by a high-voltage probe (Tektronix, USA), the discharge current was measured using a Rogowski coil, and nitrogen gas pressure was monitored using a Pirani/Cold cathode transmitter (Pfeiffer Vacuum, Germany).

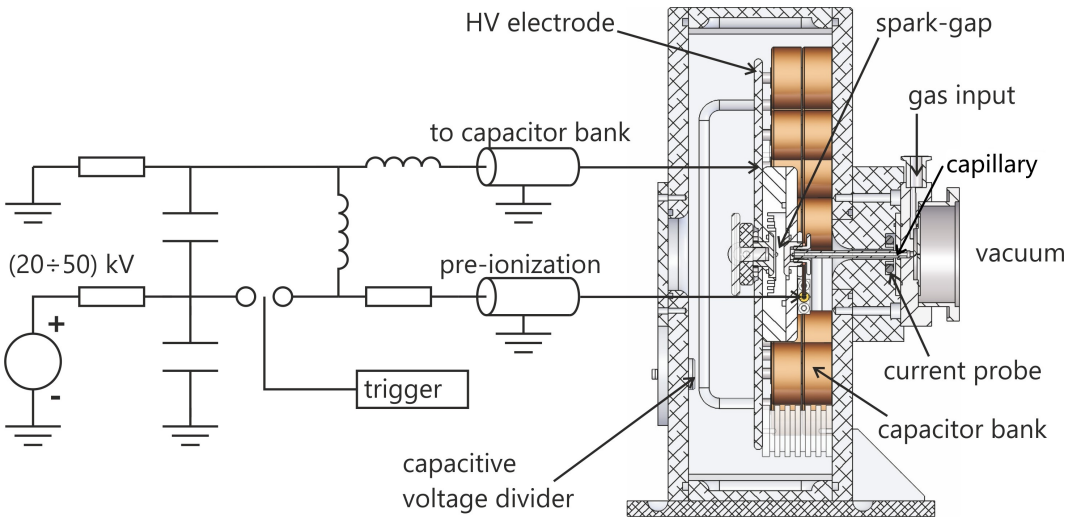

Figure 4.11: Schematic of capillary plasma driver and charging circuit [158].

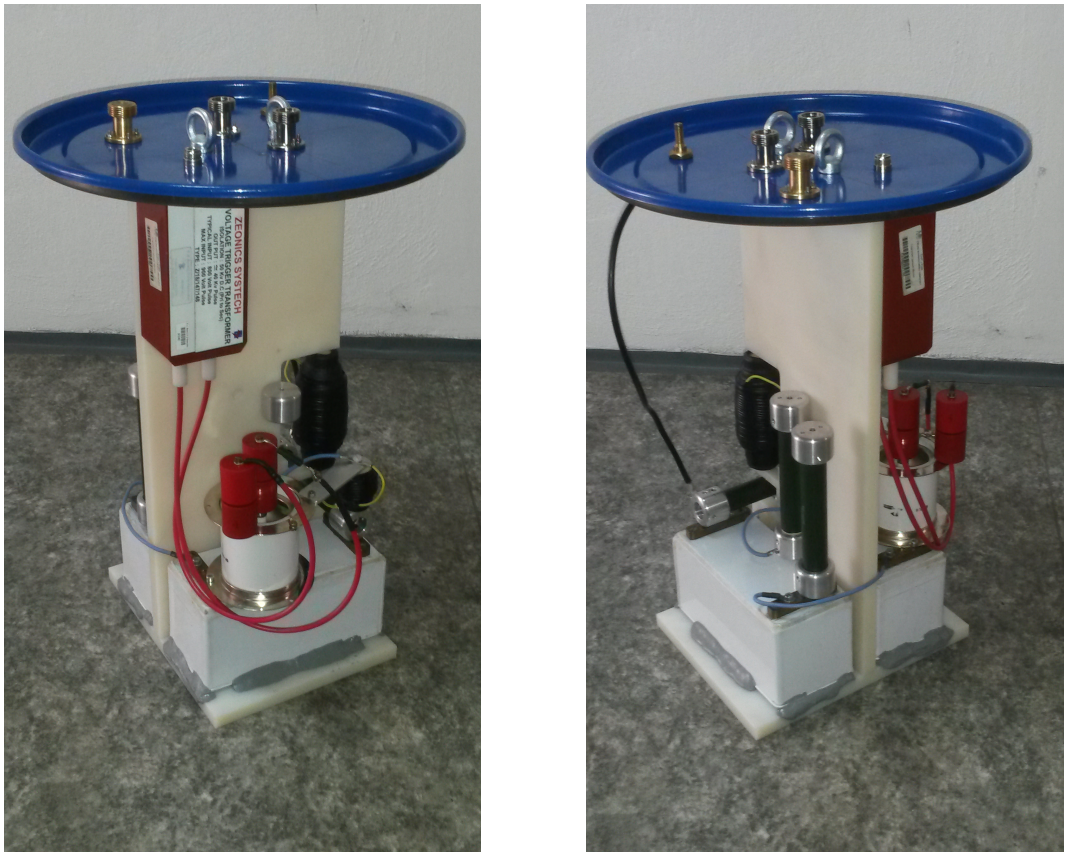

Figure 4.12: Photographs of the front and rear view of the charging circuit. While in operation, the circuit is enclosed in a barrel filled with biodegradable oil to isolate the circuit and avoid unwanted breakdowns.

4.3.2 Temporal profile of the SXR emission pulse and photon yield

The temporal profile of the soft X-ray pulse was measured with a high-speed SXR-sensitive photodiode (mentioned in detail in section 4.1)—the same photodiode used for characterization of gas-puff target laser-produced plasma source. The schematic layout of the measurement is depicted in Figure 4.13. A typical temporal profile of SXR emission pulse for nitrogen discharge-produced plasma (DPP) source is shown in Figure 4.14 including the current temporal profile measured by a Rogowski coil.

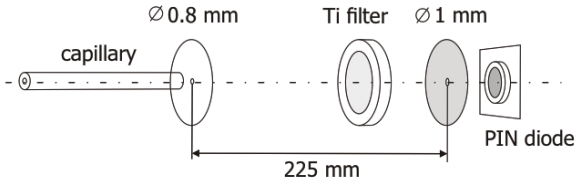

Figure 4.13: Schematic of temporal pulse profile measurement for the DPP source.

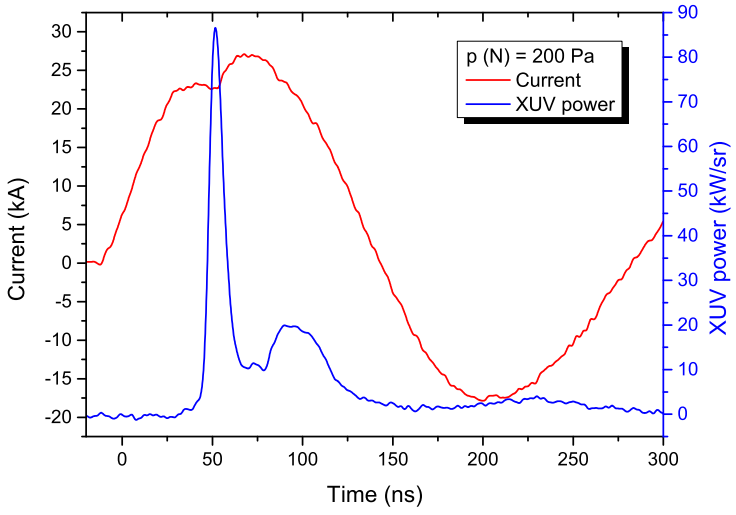

Figure 4.14: A typical temporal profile of the SXR emission pulse and current temporal profile for the nitrogen discharge-produced plasma source. Nitrogen pressure is 200 Pa. Pinch occurs at ∼50 ns indicated by a significant current "drop."

The photon flux of the DPP was calculated by numerical integration of 10 single-shot SXR pulses for each nitrogen pressure. Figure 4.15 depicts the photon flux dependence on nitrogen pressure, and Figure 4.16 illustrates the length of the SXR pulse at FWHM in dependence on nitrogen pressure. The conditions of measurements were: nitrogen pressure 10–500 Pa, vacuum chamber pressure three orders lower than nitrogen pressure, fixed discharge current 26–27.5 kA, and repetition rate of the source 2 Hz.

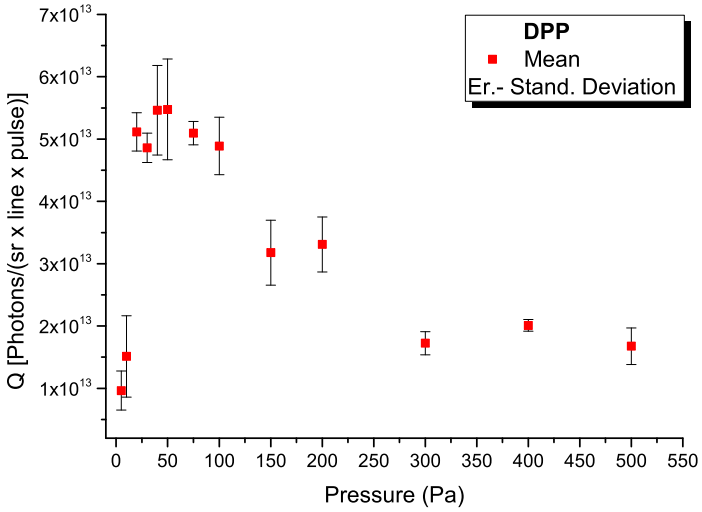

Figure 4.15: Photon flux dependence on nitrogen pressure for discharge-produced plasma source. Discharge current fixed 26–27.5 kA.

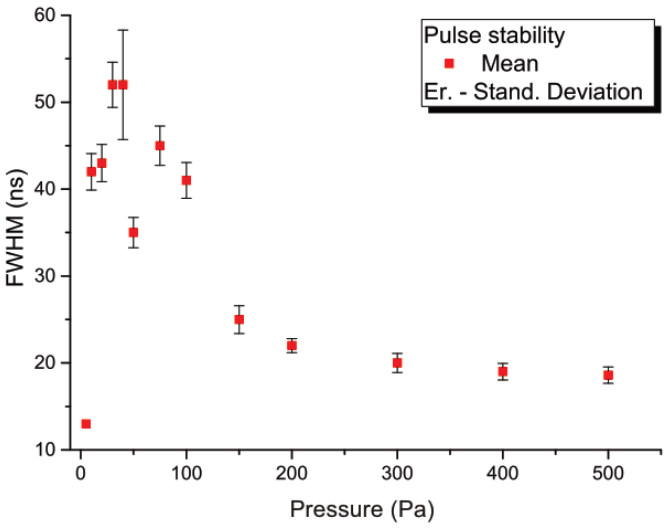

Figure 4.16: Soft X-ray pulse duration at full-width half-maximum depending on nitrogen pressure for the DPP source.

The maximal photon flux of nitrogen discharge-produced plasma source is 5.5×10^{13} photons per steradian per pulse, which corresponds to the energy of 3.8 mJ per steradian per pulse for a nitrogen pressure of 50 Pa. The overview of measured parameters is shown in Table 4.3.

Table 4.3: Radiance overview of nitrogen discharge-produced plasma source.

Parameter	Value
Photon flux per sr per pulse	5.5×10^{13} photons
Energy/(pulse per sr)	3.8 mJ
Source efficiency	4.47×10^{-5} †
Peak power per sr	87 kW

4.3.3 Spatial distribution of the SXR radiance

The spatial distribution of nitrogen (N_2) SXR radiation emission was observed using a 3.7× magnifying pinhole camera equipped with a 500 nm thick Ti foil as an SXR band-pass filter. The schematic layout for source size measurement is shown in Figure 4.18. The spatial profile of nitrogen plasma is depicted in Figure 4.17 and was acquired by the integration of ten single-shot images. Nitrogen plasma has a circular shape with a diameter of 360 μm at FWHM; in Figure 4.17, the input aperture, 0.8 mm in diameter, separating the discharge gas in the capillary from the vacuum, is visible and defined the field of view. Conditions of measurement were: nitrogen pressure 200 Pa, source repetition rate 2 Hz, current maximum 23 kA.

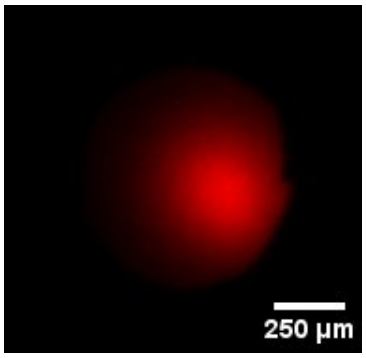

Figure 4.17: Spatial distribution of soft X-ray emission from nitrogen discharge-produced plasma source.

According to the spatial profile measurement at different positions, the beam divergence was determined to be ∼30 mrad. The spatial distribution of SXR radiation emission was recorded onto a back-illuminated CCD camera (X-vision M25, Rigaku

†The input energy is 65 J. Calculated as $E = \frac{1}{2}CU^2$, where C is the capacity of condensator, and U is voltage.

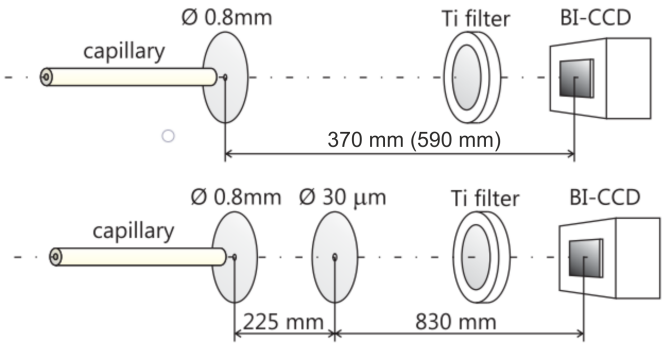

Figure 4.18: Schematic layout for beam profile (top) and source size (bottom) measurement.

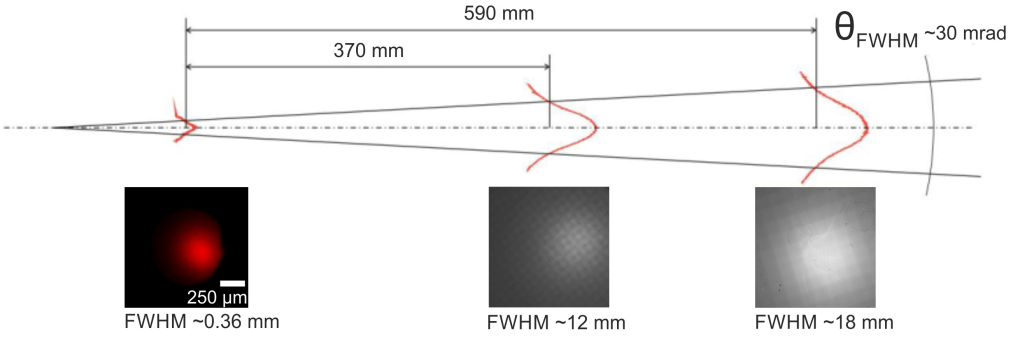

Figure 4.19: Beam divergence and spatial profile measurement. **Left**: Source pinhole image with a scale bar 250 μm. **Middle**: Spatial profile image 370 mm from the capillary exit, taken with Ti and Mylar foil. Both filters were with a supportive Ni mesh. **Right**: Spatial profile image 590 mm from the capillary exit, taken with a Ti foil with a supportive Ni mesh. Corresponding line profiles are plotted above the images, and below the images, a beam diameter at FWHM is indicated. The calculated beam divergence is ∼30 mrad.

Innovative Tech.) cooled to -20 °C at a distance of 370 mm, 590 mm, respectively, from the exit of the capillary as indicated in Figure 4.18. An 800 nm thick Ti foil was used as an SXR band-pass filter, and a 1 μm thick Mylar foil was added at a shorter distance measurement to suppress the saturation of the CCD chip. Both foils were with a supportive Ni mesh. The beam profile and spatial distribution of nitrogen plasma at different positions are shown in Figure 4.19.

4.3.4 Emission spectra of SXR plasma source

Soft X-ray microscope employing the Fresnel zone plate optics requires monochromatic radiation. Further, the monochromaticity of radiation is desired for its avoiding of chromatic aberrations during the image formation process; thus, spectral characterization is essential.

Emission spectra in the water-window spectral region were measured using a free-standing Si_3N_4 transmission grating, described in section 4.1 "Diagnostic in-

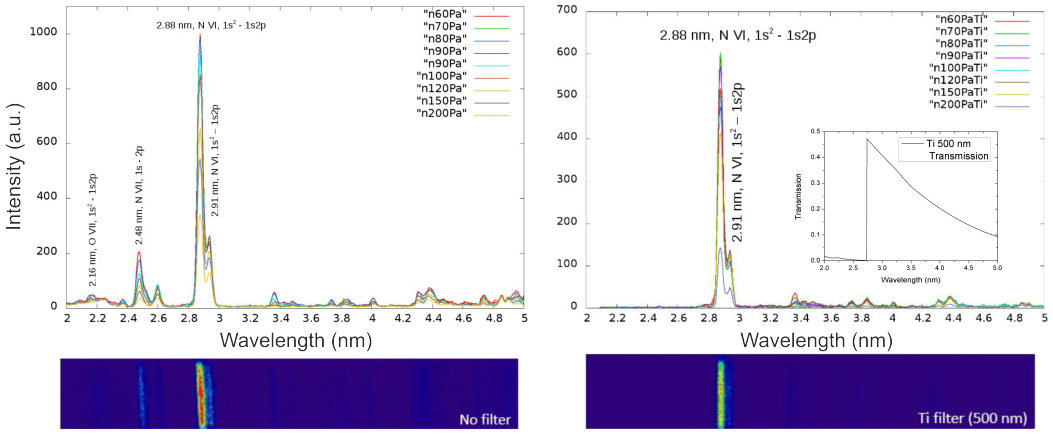

Figure 4.20: Nitrogen emission spectra without Ti filter (left image) and with Ti filter (right image) in the water-window spectral region. Transmission dependence on wavelength for a 500 nm thick Ti filter is shown in the inserted image (data obtained from the database [51]). Adapted from [43, 164].

struments" in detail. The main peak of nitrogen (N_2) plasma emission occurs at a wavelength of 2.88 nm (430 eV), corresponding to the quantum transition $1s^2$–1s2p of the helium-like nitrogen ions. The emission spectra were identified using NIST atomic spectra database [162]. Figure 4.20 shows the emission spectra in the spectral range from 2 nm to 5 nm with a resolution of 0.03 nm. The raw images of spectrally dispersed emission of nitrogen plasma were integrated with ten pulses for each nitrogen pressure. Using the titanium filter with a thickness of 500 nm, all radiation with a wavelength shorter than the transmission edge (∼2.73 nm) is excluded. The transmission of a 500 nm thick Ti filter at 2.88 nm was calculated to ∼44 % (data obtained from the database [51]). Although the spectral line 2.91 nm is still noticeable after the filtration, its intensity is significantly lower in magnitude compared to the spectral line of 2.88 nm and will have not a significant impact on the aberration effects in the image formation process. Conditions of measurements were: nitrogen pressure 60–200 Pa, vacuum chamber pressure three orders lower than nitrogen pressure, source repetition rate 2 Hz, current maximum 21 kA.

If someone was interested in the emission spectra from nitrogen Z-pinching capillary discharge source outside the water-window spectral region, we have published it in [163].

4.4 Comparison of laser- and discharge-produced plasma as a source for soft X-ray microscopy

In previous sections, two laboratory hot dense plasma sources in possession of Czech Technical University in Prague were introduced and characterized as a potential table-top source for a full-field transmission soft X-ray microscope. Both sources, i.e., laser- and discharge-produced plasma sources, utilize nitrogen plasma for its quasi-

monochromatic radiation in the water-window spectral region. The most crucial criterion for microscopy purpose is the brightness of the source. The photon flux of the discharge-produced plasma in nitrogen is 5.5×10^{13} ph./(sr $\times$ pulse $\times$ line) (see section 4.3) providing ∼30 times higher photon flux than the laser-produced plasma in nitrogen (1.8×10^{12} ph./(sr $\times$ pulse $\times$ line)), see section 4.2. The repetition rate is 2 Hz for both sources. In the case of the LPP source, the repetition rate is mainly limited by an injection of the gas, specifically the opening of a high-pressure piezoelectrically actuated valve. Whereas the main limitation for increasing the repetition rate of the DPP source is the thermal matter of cooling the capillary. DPP source can operate at 3 Hz for a short time duration, but in every-day operation, 2 Hz is maximum with regard to a long lifetime of the capillary.

Although there is a significant difference in the SXR pulse duration for each source, ∼5 ns at FWHM for the LPP source and ∼52 ns at FWHM for DPP source; this does not affect in the context of SXR microscopy as both SXR pulses are in the order of nanoseconds.

The SXR pulses emitted by the capillary discharge source are not so stable as the SXR generated by the laser-produced plasma source. However, even in the case of instability, the photon flux is much higher from the DPP source. Due to the higher brightness, the decision was made to start developing a compact soft X-ray microscope based on the nitrogen discharge-produced plasma source. The gas-puff target laser-produced plasma source is more suitable for other applications due to a short duration of SXR pulses, e.g., time-resolved luminescence spectroscopy [90]. However, the brightness of both sources can still be further optimized. Emittance of the LPP source can be enhanced by, e.g., increasing the density of the target or using a sub-ns laser pulse [91]. The brightness of the DPP source can be enhanced by an optimization of the capillary's geometry, especially decreasing the radii of the capillary, or by increasing the initial voltage, i.e., a higher current [165]. Nevertheless, the higher current leads to ablation of the capillary wall [155]. The issue of high current produced by the discharge source is solved by enclosing the charging circuit and plasma driver in duralumin housing filled with oil to isolate the circuit and to avoid unwanted breakdowns. Contrary to that, the LPP source is a "clean" system. Despite the above-mentioned, the discharge-produced plasma source is still more suitable for SXR microscopy.

5 | Full-field transmission water-window microscope

This Chapter is founded on our article "Table-Top Water-Window Microscope Using a Capillary Discharge Plasma Source with Spatial Resolution 75 nm" [44], and presents a design and imaging performance of a compact transmission water-window microscope based on the Z-pinching capillary discharge nitrogen plasma source. The microscope operates at wavelength of 2.88 nm (430 eV). With its table-top dimensions–roughly 0.5 × 2 m; depending on the actual magnification of the microscope, which is adjustable from 190× up to 400×, it provides an alternative to large-scale soft X-ray microscope systems based on synchrotrons and free-electron lasers.

5.1 Experimental layout

The sketch of the microscope is shown in Figure 5.1, and Figure 5.2 illustrates a real photograph of the microscopic system. The aforementioned discharge-produced nitrogen plasma was used as a source of pulsed soft X-ray radiation. The principle of the Z-pinching capillary discharge source in nitrogen was described in the previous Chapter (see 4.3), including the characterization of its SXR emission.

The emitted SXR radiation is filtered through a titanium filter (Lebow, USA) to achieve quasi-monochromatic radiation with wavelength $\lambda = 2.88$ nm (430 eV). The Ti foil is mounted in a custom-made holder depicted in Figure 5.3. This holder is adjusted for three Ti filters, one with a thickness of 800 nm for the setup and alignment of the optical components of the microscope. The second with a thickness of 200 nm for imaging experiments. The third titanium filter (500 nm thick) is sitting on a 600 μm aperture (SPI Inc., USA); behind that there is an SXR-sensitive photodiode—(AXUV20HS1, Optodiode, USA) with a reverse bias of 150 V—in order to monitor a temporal profile of SXR pulses. The filters holder is connected to a vacuum rotary/linear feedthrough (DS040A, Pfeiffer Vacuum, Germany) to enable changing the filters or monitoring the SXR pulses during the microscope operation.

The filtered radiation is focused by an ellipsoidal, grazing incidence, nickel-coated condenser mirror (Rigaku Inc., USA) into the sample plane. The condenser is mounted on 5-axis motorized stages consisting of three linear translation stages

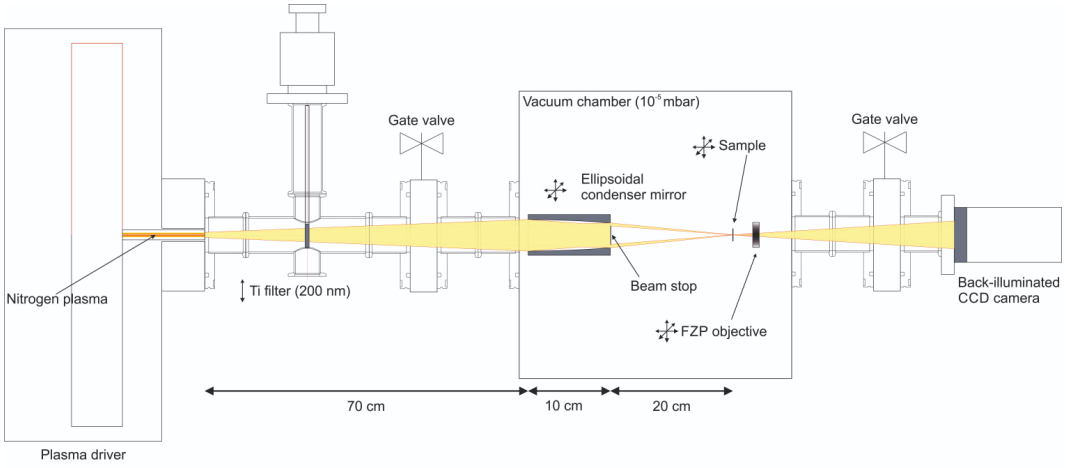

Figure 5.1: Schematic of a water-window microscope based on a nitrogen plasma capillary discharge source.

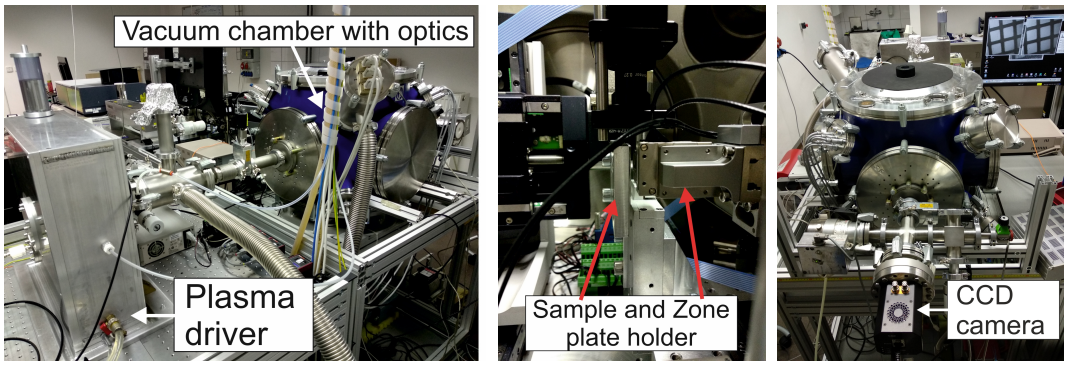

(a) (b) (c)

Figure 5.2: Photographs of the soft X-ray imaging system: **(a)** The "source" view showing plasma driver and vacuum chamber with imaging optics, **(b)** the internal photograph of a vacuum chamber with sample and zone plate holder, **(c)** photograph of the "imaging" part of the SXR microscope.

(M-405.CG, Physik Instrumente, Germany) and 2-axis motorized goniometer stage (GNL20, Thorlabs, Germany). Three linear translation stages (PT1/M-Z8, Thorlabs, Germany) making a 3-axis linear positioner were used to manipulate the sample.

A Fresnel zone plate (ZonePlates Ltd., UK) is employed to create an image of a specimen transmission on an SXR-sensitive back-illuminated CCD camera (Greateyes GmbH, Germany) cooled down to minus 30 °C to minimize its thermal noise. The Fresnel zone plate is mounted on 5-axis motorized stages consisting of a 2-axis piezo linear stage (AG-LS25V6, Newport, USA), 1-axis translation stage (PT1/M-Z8, Thorlabs, Germany), and 2-axis motorized goniometer stage (GNL20, Thorlabs, Germany). The CCD camera (CMLN-13S2M, Chameleon, Point Grey Research Inc., Canada) was used to provide real-time monitoring of the distance

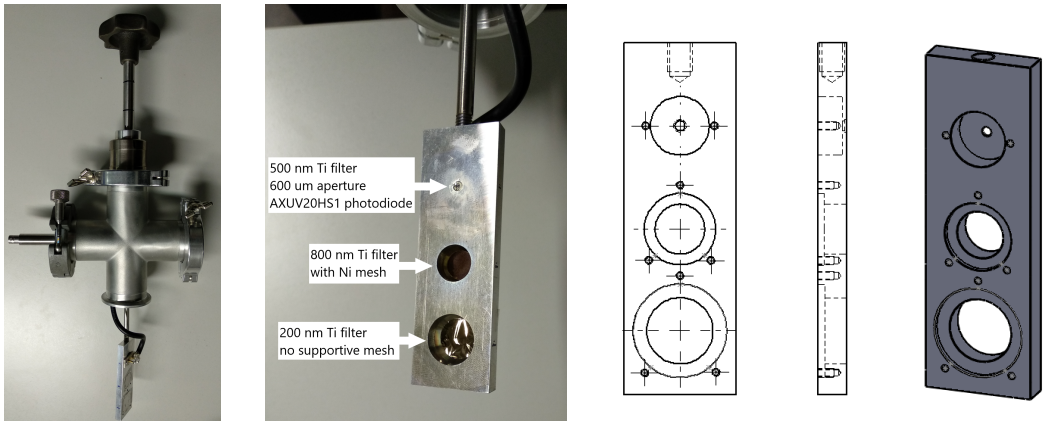

(a) (b) (c)

Figure 5.3: Photographs and design of the titanium filters holder: **(a)** The holder with Ti foils mounted on rotary/linear vacuum feedthrough, **(b)** a detail with Ti filters and AXUV photodiode, **(c)** design and a cross-section view of the holder.

between a sample and Fresnel zone plate during the alignment as well as for safety reasons during the replacement of the samples.

The whole system dimensions are roughly 0.5 × 2 m, depending on the actual magnification of the microscope, which is adjustable from 190× up to 400× by changing the distance between the zone plate and the BI-CCD camera. The microscope is sectioned into three separable sections, indicated in Figure 5.1 by a gate valve, each with independent vacuum pumping (diaphragm or scroll pump and turbopumps; Pfeiffer Vacuum, Germany), and each section is equipped with a vacuum gauge to monitor the pressure. To minimize the mechanical vibration coming from the source, the plasma driver is placed on a separate optical table and is connected to a vacuum chamber by a bellow as visible in Figure 5.2a.

5.2 Optics, sample stage, and detector

5.2.1 Ellipsoidal condenser mirror

An ellipsoidal, grazing incidence, nickel-coated condenser mirror (Rigaku Inc., USA) was used to collect the SXR radiation emitted from the nitrogen plasma. The axisymmetric condenser mirror is located at a distance of 700 mm (first focal length) from the capillary exit, as demonstrated in Figure 5.4, where the width of the SXR beam is ∼21 mm at FWHM and the input aperture of the condenser is 19.8 mm. The length of the mirror is 100 mm. The reflectivity of the condenser with nickel-coating at $\lambda = 2.88$ nm (430 eV), assuming a single layer of Ni with a thickness of 30 nm, surface roughness ∼2 nm, is over 83 % for incidence angles lower than 1.7° (∼30 mrad). However, the reflectivity of the condenser mirror is strongly dependent

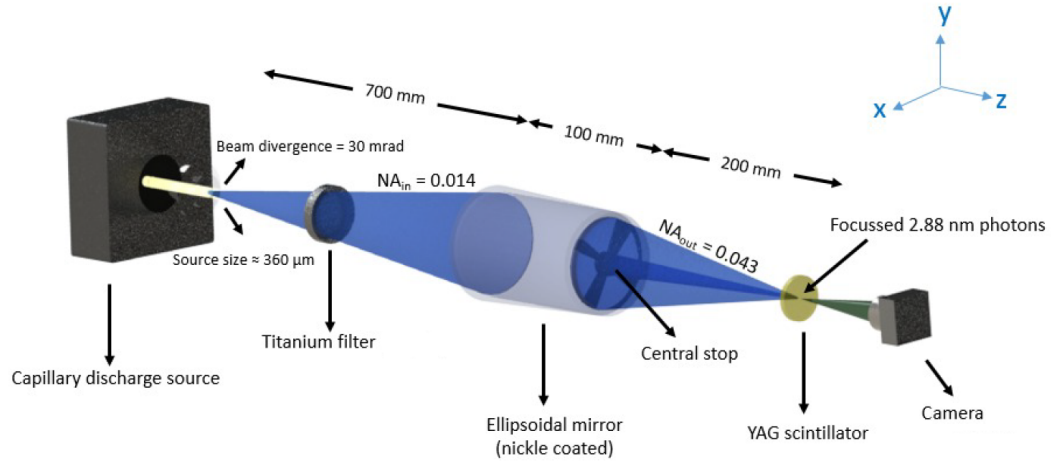

Figure 5.4: Schematic of condenser alignment. Focusing of the SXR radiation observed on the YAG:Ce scintillator. Adapted from [109].

Table 5.1: The reflectivity dependence on the surface roughness of nickel-coated condenser mirror. Calculations were done for radiation wavelength of 2.88 nm (430 eV), incidence angles lower than 1.7°, and a single layer of Ni with a thickness of 30 nm. The calculations are based on optical data from [51].

Surface roughness (nm)	Reflectivity (%)
2	>83
5	>68
8	>48
10	>35

on the surface roughness, as indicated in Table 5.1. The calculations were performed based on the optical data from [51].

To prevent the 0th order from coming through, a beam stop is placed inside the condenser. The collected radiation is focused into the sample plane (condenser second focal plane) at a distance of 200 mm. The condenser produces an image of the plasma with a magnification of $M \approx 0.3$. The complete condenser specifications are listed in Table 5.2.

The spatial distribution of SXR radiation at the condenser second focal plane (sample plane) was observed using a YAG:Ce (Yttrium aluminum garnet activated by cerium) scintillator. The observed spot was monitored by a CCD camera (CMLN-13S2M, Chameleon, Point Grey Research Inc., Canada) with resolution 1296 × 964 pixel of size 3.75 × 3.75 μm. To get the possible smallest, uniform spot, the condenser mirror is mounted on 5-axis motorized stages (three linear and two rotational positioners) with a sub-micron step motion to allow precise alignment. Likewise, the scintillator (later replaced by a sample) is mounted on 3-axis motorized stage (three

Table 5.2: The specification of an ellipsoidal, axisymmetric, nickel-coated condenser mirror.

Parameter	Value
Input numerical aperture	0.014
Input diameter	19.8 mm
First focal length	700 mm
Mirror length	100 mm
Output numerical aperture	0.043
Output diameter	17.3 mm
Second focal length	200 mm
Ellipse semi-minor axis	10.804 mm
Ellipse semi-major axis	500.1167 mm

linear positioners).

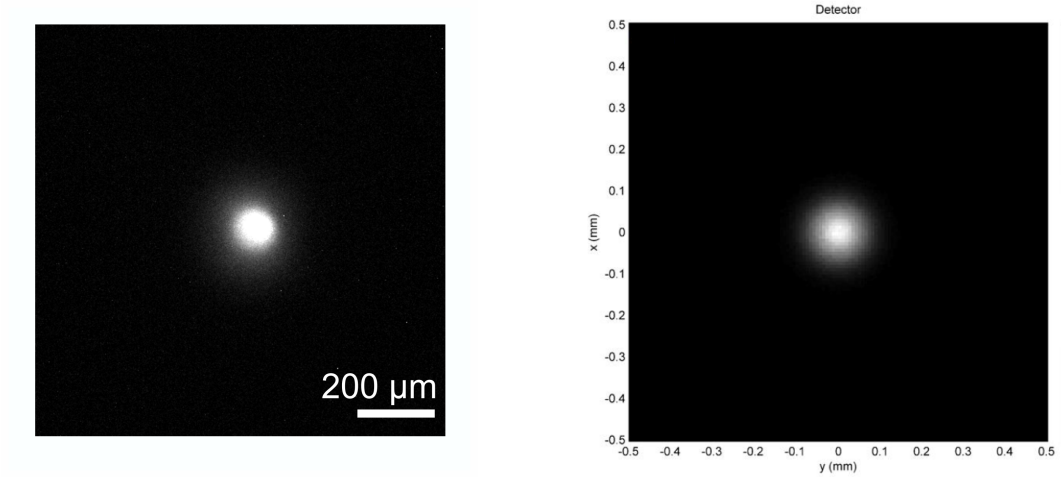

(a) (b)

Figure 5.5: Spatial distribution of SXR radiation (2.88 nm) focused by the condenser in the sample plane (condenser second focal plane): **(a)** Observed focused spot visualized by the YAG:Ce scintillator. Scale bar is 200 μm; the spot has a circular shape with a diameter of ∼130 μm at FWHM. **(b)** Theoretical focused spot, calculated from raytracing of the condenser mirror. The calculated spot is perfectly axially symmetric, having a circular shape with a diameter of ∼100 μm at FWHM. Dimensions are indicated along with the image. The calculated image (b) is reprinted from [166].

The smallest achievable spot is illustrated in Figure 5.5a, having a circular shape with a diameter of ∼130 μm at FWHM. This dimension is comparable with the theoretical value obtained from the raytracing program. The source and condenser parameters were used as input for the raytracing simulation program, supported by Rigaku. The simulation was performed with one million rays through the condenser mirror, assuming ∼85% reflectivity, 2 nm surface roughness, and a focal length of 200 mm. The theoretically focused spot is depicted in Figure 5.5b, having a perfectly

circular shape with a diameter of ∼100 μm [166]. The observed spatial distribution of SXR radiation outside the focal plane of the condenser initially has a "donut" shape, further changing into a ring-shaped profile.

5.2.2 Sample stage

The inorganic and organic samples were mounted on a holder attached to 3-axis motorized linear stages, aligned to the condenser second focal plane described in the previous section. Biological specimens were deposited onto an Si_3N_4 membrane (Norcada Inc., Canada) with a thickness in the order of tens nanometers. The transmission of 50 nm thick silicon nitride membrane is ∼71 % for radiation wavelength of 2.88 nm; the calculation is based on optical data from [51]. More details about the sample preparation are provided in the section "5.4 Biological application".

5.2.3 Fresnel zone plate

A Fresnel zone plate (NT26, ZonePlates Ltd., UK) was employed as an imaging objective to create an image of a specimen transmission on an SXR-sensitive detector. The zone plate is composed of 130 nm thick tungsten zones on a 100 nm thick Si_3N_4 membrane. Diffraction efficiency is 12 % for tungsten in the 1st order at $\lambda = 2.88$ nm (see Figure 2.15), and transmission is ∼3.5 % at 2.88 nm. The transmission of substrate, silicon nitride membrane of thickness 100 nm, is ∼50 % at a wavelength of 2.88 nm. All the calculations are based on optical data from [51]. The real images of the zone plate are illustrated in Figure 5.6, captured by a scanning electron microscope (SEM).

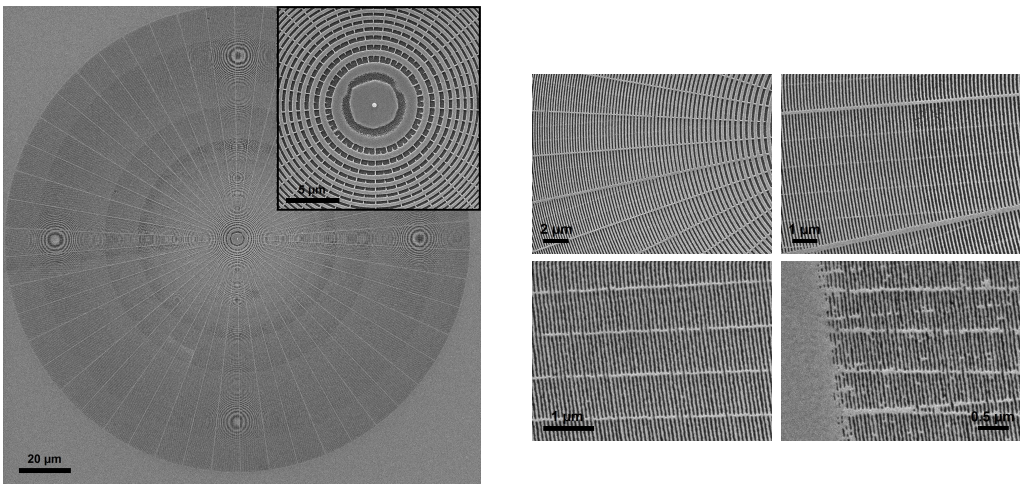

Figure 5.6: Scanning electron microscope images of the Fresnel zone plate used for imaging. **Left:** An image of the whole zone plate. The image indicated by a black square represents a zoomed view of the zone plate center. **Right:** The zone plate images of the different sections, sorted from the central part to the edge of the zone plate. The corresponding scale bar is shown in all images. Images were taken by ZonePlates Ltd., UK.

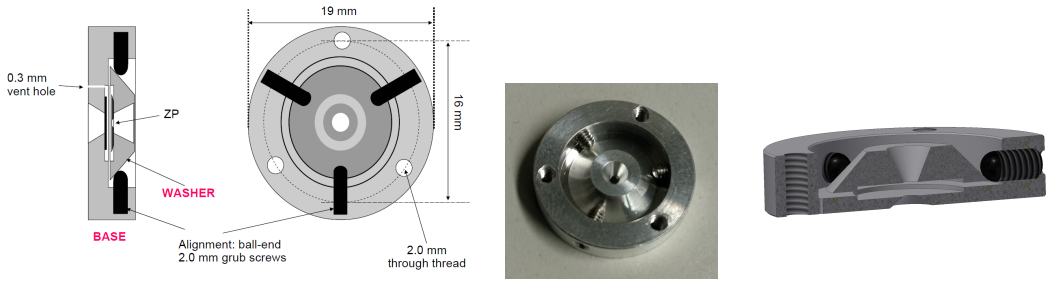

(a) (b) (c)

Figure 5.7: Zone plate alignment holder: **(a)** Schematic of a zone plate holder, **(b)** photograph of a zone plate holder made of aluminum, and **(c)** a cross-section of the 3D model.

Table 5.3: The specifications of Fresnel zone plate (NT26) composed of 130 nm tungsten deposited on 100 nm thick silicon nitride membrane. Focal length and depth of focus are related to wavelength of 2.88 nm (430 eV).

Parameter	Value
Width of the outermost zone	30 nm
Numerical aperture	0.048
Total number of zones	1500
Diameter of the zone plate	180 μm
Focal length	1.87 mm
Depth of focus	1.25 μm

The zone plate with a diameter of 180 μm was mounted into a special holder, shown in Figure 5.7, providing support and protection. The holder is attached to 5-axis motorized stages (three linear and two rotational positioners), allowing a 50 nm step motion. The zone plate is aligned to 1.87 mm away from the sample, i.e., zone plate focal length for SXR radiation with a wavelength of 2.88 nm (430 eV). The distance between a sample holder and zone plate holder was monitored in real-time by the CCD camera (Chameleon, Point Grey Research Inc., Canada). According to Rayleigh's resolution criterion, the maximal possible resolution is determined by the width of the outermost zone, being, in our case, 30 nm. Consequently, the maximal resolution with our zone plate is ∼37 nm. The numerical aperture of the zone plate is 0.048, and the output numerical aperture of the condenser is 0.043, yielding the coherence factor σ. In our case, making the *degree of coherence* of 0.9, meaning the partially coherent imaging, although it has to be noted that $\sigma = 1$ is usually sufficient to get fully incoherent behavior [122]. The influence of coherence on the image formation was discussed in the section "3.2 Image formation." In general, coherent imaging systems have higher contrast compared to the incoherent imaging systems that provide a better resolution. Table 5.3 provides a complete specification of the zone plate.

5.2.4 Back-illuminated CCD camera

The images were acquired using an SXR-sensitive back-illuminated charge-coupled device (BI-CCD) camera (GE 2048 BI, Greateyes GmbH, Germany). The camera has 2048 × 2048 pixels with a pixel size of 13.5 × 13.5 μm with ∼83% quantum efficiency at wavelength of 2.88 nm. The CCD image sensor is cooled down to minus 30 °C via a multistage thermoelectric cooler to minimize its thermal noise. The liquid cooling system is provided by a closed-looped circulation (MX07R-20-A12E, PolyScience, USA). The magnification of the microscope is adjustable from 190× up to 400× by changing the distance between the objective zone plate and the camera. The current field of view depends on the actual magnification of the microscope, and it varies between 145 μm and 70 μm for both lateral and perpendicular axes. For a lucitidy, the complete specifications of the camera are listed in Table 5.4.

Table 5.4: The specifications of back-illuminated CCD camera (GE 2048 BI). The quantum efficiency is related to wavelength of 2.88 nm.

Parameter	Value
Total number of pixels	2048 × 2048
Pixel size	13.5 × 13.5 μm
Image active area	27.6 × 27.6 mm
Quantum efficiency	83 %
Pixel readout frequency	500 kHz – 3 MHz

5.3 Microscope performance

5.3.1 Spatial resolution

The imaging experiments with a copper TEM mesh (SPI, USA) with 1000 lines/inch (bar width 6 μm, hole width 19 μm) were performed to determine the spatial resolution of the microscope. The measured and calculated magnification was around 340× for this microscope layout, and, thus, the corresponding field of view is ∼80 × 80 μm. The image of Cu mesh shown in Figure 5.8a was acquired with an exposure time of 3 min and the repetition rate of the capillary discharge source of 2 Hz, which allowed the acquisition of 360 SXR pulses. Some imperfections in the mesh are visible, one is highlighted in a red circle, and the corresponding dimension is listed. The spatial resolution was calculated via a knife-edge test across a sharp edge. It is a common resolution test relying on the response of an optical system to a sharp edge, or expressed mathematically, 2D-object with a zero transmittance for the edge material and unity transmittance elsewhere. A 10–90% intensity transition, corresponding to the Rayleigh resolution limit [28], is equal to 150 nm; a half-pitch spatial reso-

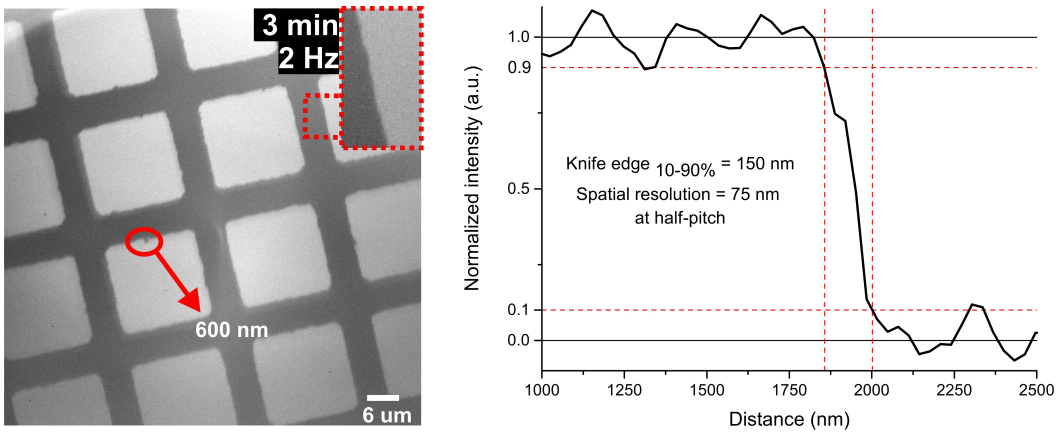

(a) (b)

Figure 5.8: **(a)** Soft X-ray image of copper mesh 1000 lines/inch acquired with 3 min exposure time (360 SXR pulses). A red, dashed rectangle highlights a sharp edge representing the place where the spatial resolution was calculated. Scale bar is 6 µm. **(b)** Knife-edge resolution test results showing normalized intensity profile across a sharp edge. A 10–90% intensity transition corresponding to Rayleigh resolution is equal to 150 nm, half-pitch spatial resolution equal to 75 nm, measured from the image of the Cu mesh.

lution is equal to 75 nm (Figure 5.8b), measured from the image of the mesh and highlighted by a red, dashed rectangle. The spatial resolution was calculated from the average of several intensity profiles along the edge to remove the effect of noise. The spatial resolution is the same for all ranges of magnification as the pixel size of the CCD camera is sufficiently small; nevertheless, with higher magnification, the exposure time is longer to provide an image of similar quality.

5.3.2 Signal-to-noise ratio

To compare the quality of soft X-ray images of Cu mesh, several images were taken with different exposure times. Figure 5.9 depicts the outcome of this experiment, demonstrating the differences among the soft X-ray images of Cu mesh taken with 10, 30, 60, and 180 SXR pulses, respectively, at a 2 Hz repetition rate of the source. Some imperfections of the Cu mesh are still visible down to a 5 s exposure time.

The signal-to-noise ratio (SNR) analysis was performed to compare the SXR images qualitatively. The approach is based on background-free single-image SNR estimation [167], i.e., together with the SXR images of Cu mesh, the corresponding background images were acquired. Subsequently, the background images were subtracted in order to obtain background-free SXR images. For soft X-ray microscopy application, the signal-to-noise ratio is calculated according to the following relation [168]:

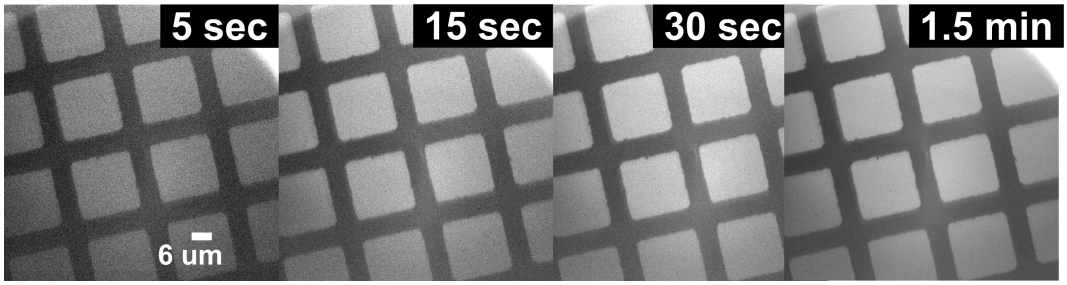

Figure 5.9: Comparison of soft X-ray images of copper mesh (1000 lines/inch) with different exposure times. The scale bar is 6 μm and is the same for each image. The magnification was 340×, resulting in ∼80 × 80 μm field of view. The repetition rate of the source was 2 Hz, allowing the acquisition of 10, 30, 60, and 180 SXR pulses, respectively.

$$SNR = 20 \log_{10} \frac{\bar{S}}{\sigma_N} \quad [\text{dB}] \tag{5.1}$$

where $\bar{S}$ is the mean value of the signal, and σ_N is the standard deviation of the noise. In SXR microscopy, there is no possibility to compare the acquired images directly with other ideal images (template), thus any correlation methods cannot be applied, and only the data available in the image itself might be used for the SNR assessment [168].

Each SXR image of Cu mesh was segmented into four areas to evaluate the signal-to-noise value statistically; the segmentation is indicated by a letter "A" in Figure 5.10a and visualized by a white rectangle. The signal value was measured inside the mesh square holes (bright areas), indicated as S1–S4 and the noise value was measured inside the mesh bars (dark areas), indicated as N1–N4. The analyzed area was equal, ∼1 × 1 μm, and at the identic location for all SXR images.

The mean value of the signal ($\bar{S}$) increases with the higher exposure times, i.e., with a higher number of SXR pulses. A part of SXR energy is deposited in the "noise region" at the image plane due to a low diffraction efficiency (∼12%) of the Fresnel zone plate. For this reason, the intensity and its standard deviation in the "noise region" only ideally are equal to zero ($\sigma_N \to 0$) [168].

The SXR images were taken with an acquisition of 1–300 SXR pulses with the repetition rate of the source of 2 Hz. The CCD sensor was cooled down to minus 30 °C, and the pixel readout frequency of the CCD chip was 3 MHz.

The measured data confirmed the theory that the signal is scaled in a linear dependence on the number of SXR pulses, while the noise is increasing by a factor proportional to a square root of the SXR pulse number. Consequently, a ratio between signal intensity and noise intensity is proportional to the square root of the SXR pulses number. Figure 5.10b represents the evaluation of SNR in dependence

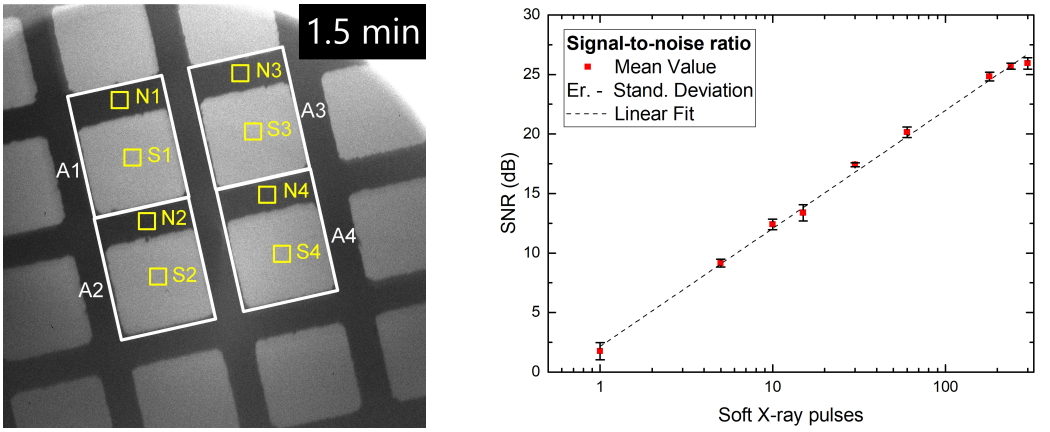

(a) (b)

Figure 5.10: Signal-to-noise ratio calculation: **(a)** An SXR image of Cu mesh with four areas indicated by a white rectangle (A1–A4), where the signal value (yellow square indicated as S1–S4, mesh holes) and the noise value (yellow square indicated as N1–N4, mesh bars) were calculated to obtain the SNR. The areas showed by the yellow squares are enlarged here for better visualization. The analyzed areas were equal and at the identical location for all nine SXR images. **(b)** SNR dependence on the number of the SXR pulses.

on the number of SXR pulses. The signal-to-noise ratio is rising in the logarithmic dependence on the number of SXR pulses and can be expressed as

$$SNR = 4.3 \ln n + 2.15 \quad [\text{dB}] \tag{5.2}$$

where the n is the number of SXR pulses. The reliability of the trendline is $R^2 = 0.997$.

The optimization of images acquired by an SXR microscope was investigated in [168] in terms of the exposure, repetition rate of the source, temperature of the CCD sensor, and the readout frequency of the CCD chip. In general, according to [168] the SNR does not significantly change in terms of the repetition rate of the source and the readout frequency of the CCD chip in the case of images acquired with ten or more SXR pulses. Also, if the CCD sensor is cooled down to minus 20 °C or below, the SNR remains coincident. However, the parameters mentioned above have a more substantial influence on the SNR of the images acquired with less than ten SXR shots, especially in single-shot imaging. To improve the SNR of single-shot images, binning, i.e., spatial integration of the pixels, is recommended. Even though binning leads to a reduction of the spatial resolution of the microscope, the increased SNR is more beneficial as the $M \times M$ spatial binning optimizes the SNR approximately by a factor of M.

5.4 Biological application

Soft X-ray microscopy has found its application in many different science and technology areas, such as biomedicine, material science, nanotechnology, and microelectronics, among others. Nevertheless, the soft X-ray microscopy in water-window spectral region is most beneficial for biological imaging, allowing high-resolution imaging of whole cells without the necessity of staining or slicing. The biological application is demonstrated here by imaging of *Desmodesmus communis*. It is a green alga (Chlorophyta) that forms in a coenobium–a colony of algae that acts as a single organism.

5.4.1 Sample preparation

A drop of the algal suspension (10 μL) was placed onto an Si_3N_4 membrane (Norcada Inc, Canada; thickness 50 nm). The sample was fixed 1:1 with the mixed solution of 2% glutaraldehyde in 0.1 M Na-cacodylate buffer and 4% paraformaldehyde in phosphate-buffered saline (PBS) for three hours. After fixation, the sample was rinsed in 0.1 M Na-cacodylate buffer in PBS for 5 min. Then, it was dehydrated in ethanol solutions of 70%, 80%, 90% for 5 min, and three times in 100% for 10 min each. After the 100% ethanol step, it was dried with a hexamethyldisilazane (HMDS) treatment: The sample was immersed in a 50:50 mixture of 100% ethanol and 100% HDMS for 5 min and twice in pure HDMS for 30 min before being dried in air.

5.4.2 Imaging of biological specimen

The applicability of the microscope is demonstrated by the imaging of green algae–*Desmodesmus communis*. The soft X-ray images (Figure 5.11a(c), 5.12a) were taken with a 390× magnification and an exposure time of 12 min with a 2 Hz repetition rate of the source. The inner structure (organelle) of the cell is visible and distinguishable. No post-processing was made with the soft X-ray images except for CCD background removal and brightness adjustment. For comparison, images of the same sample were taken with the visible light microscope (Figure 5.11b(d), 5.12b), the images were captured with a 400× magnification. The white, dashed rectangle in Figure 5.11b represents the field of view in Figure 5.11a. The SXR images exhibit a superior spatial resolution compared to visible light microscopy, owing to a much shorter wavelength beyond the capabilities of diffraction-limited visible light microscopes. Small features in the order of hundreds of nanometers can be easily observed, as demonstrated in a zoomed view in Figure 5.11a.

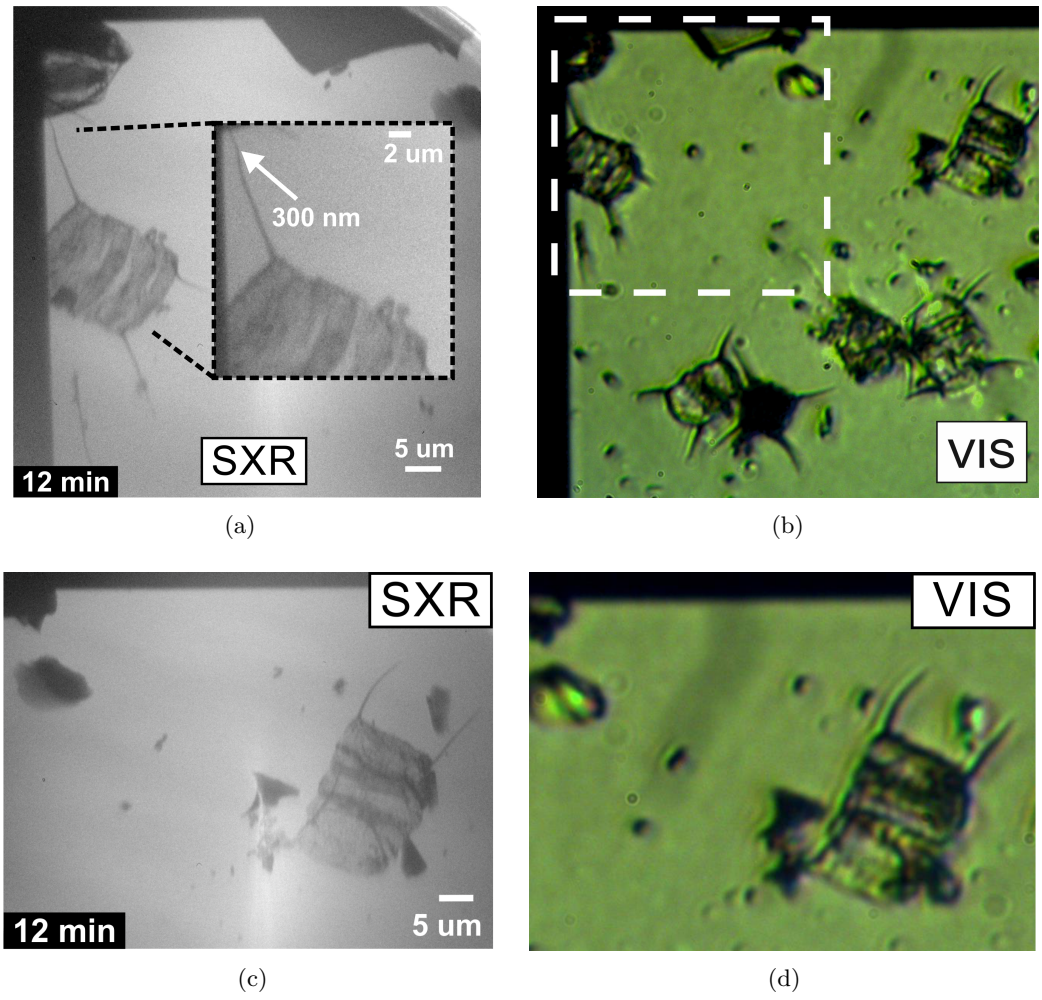

(a) (b)

(c) (d)

Figure 5.11: Comparison of the images of dried *Desmodesmus communis* deposited on a 50 nm thick Si_3N_4 membrane. **(a)** and **(c)** soft X-ray (SXR) images were acquired with 1400 SXR pulses (12 min). Scale bar is 5 μm. The black, dashed rectangle represents a zoomed area with a 2 μm scale bar. **(b)** and **(d)** the images were taken with a visible light microscope (VIS). The area marked by a white, dashed rectangle represents the field of view in image **a**.

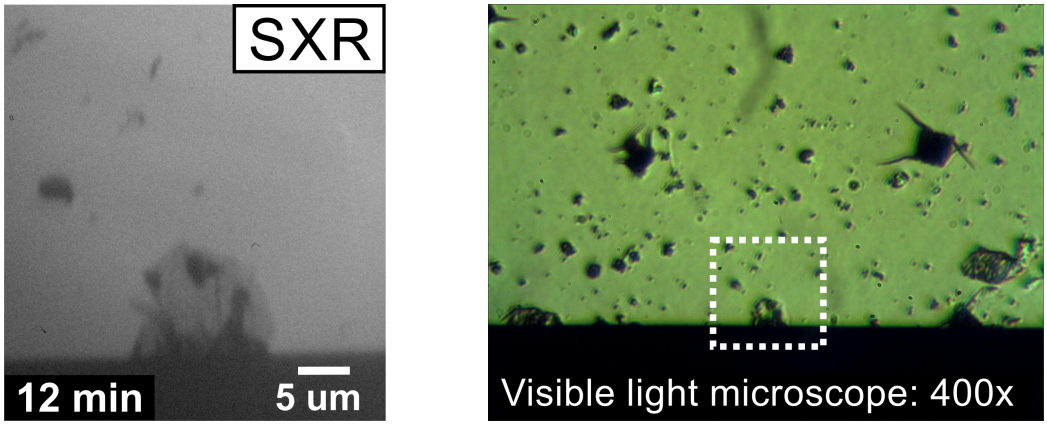

(a) (b)

Figure 5.12: Comparison of the images of deformed cell. **(a)** A soft X-ray image was acquired with 1400 SXR pulses (12 min). Scale bar is 5 μm. **(b)** The image was taken with a visible light microscope. The area marked by a white, dashed rectangle represents the field of view in image **a**.

6 | Conclusion and outlook

Besides the main goal of the doctoral thesis—the design and construction of laboratory water-window microscope with spatial resolution below 100 nm—this Thesis describes the basic principles and fundamentals of soft X-ray microscopy in water-window spectral region, as well as the basics of soft X-ray physics. It provides an overview of SXR sources and optics used in SXR microscopy and gives a short history of SXR microscopy development. It brings the image formation description and up-to-date state of the art of compact, table-top water-window microscopes.

The Thesis presents the investigation of two table-top sources in possession of Czech Technical University in Prague, namely laser-produced plasma source (gas-puff target) and discharge-produced plasma source (Z-pinching capillary source). Both sources use nitrogen as working gas for its quasi-monochromatic radiation, utilizing the spectral line $\lambda = 2.88$ nm corresponding to the quantum transition $1s^2$–1s2p of helium like nitrogen ions. The sources were fully characterized and quantitatively and qualitatively compared, i.e., the spatial distribution of SXR emission and the temporal profile of SXR emission at the wavelength of 2.88 nm. The brightness of the source is the most crucial parameter for SXR microscopy, as it directly impacts exposure times. The photon flux of the discharge-produced plasma in nitrogen is 5.5×10^{13} ph./(sr $\times$ pulse $\times$ line) providing $\sim$30 times higher photon flux than the laser-produced plasma in nitrogen (1.8×10^{12} ph./(sr $\times$ pulse $\times$ line)). Due to the higher brightness, a compact, table-top soft X-ray microscope operating in water-window region was developed based on a nitrogen discharge-produced plasma source.

A design of transmission water-window microscope based on nitrogen plasma generated by the Z-pinching capillary discharge source is presented, including the descriptions of employed optics (ellipsoidal condenser, Fresnel zone plate, and back-illuminated CCD camera). The microscope allows the capture of images of a specimen with a magnification between 190$\times$ and 400$\times$ with a 75 nm half-pitch spatial resolution. In terms of its spatial resolution, it provides a complementary imaging technique between conventional visible light microscopes and transmission electron microscopes, with the advantage of imaging relatively thick samples (up to 10 μm) without the necessity of slicing, and does not require fluorescent markers or staining that can modify the morphology of the sample. Although the spatial resolution of

this microscope cannot compete with the electron-based system, it provides a much better spatial resolution than conventional light microscopes, as it was demonstrated by the imaging of the green algae (*Desmodesmus communis*).

This microscopic system is affordable and accessible—providing an alternative to large-scale facilities—although it has a longer exposure time and lower spatial resolution by a factor of 5 compared to synchrotron-based SXR microscopes. Nevertheless, compact SXR microscopic systems have already found applications, not only in biomedicine, but also in material science, nanotechnology, and microelectronics, among others. The recent development of cost-effective table-top sources allows access to this imaging technique for the broader scientific community promising to broaden accessibility to soft X-ray imaging in other laboratories.

Our microscopic system can be further optimized and improved. The exposure time can be reduced by increasing the repetition rate of the source; however, for higher frequencies (by a factor of 3–4), active cooling of the capillary has to be implemented. The brightness of the source can be enhanced by using a higher initial voltage, i.e., higher current, although it leads to ablation of the capillary wall resulting in lower durability of the capillary, and it sets a high requirement on the quality of the capillary. The focusing optics, ellipsoidal condenser mirror, could be designed more specifically in accordance with the radiance parameter of the Z-pinching capillary discharge source. Also, using a thinner titanium filter would result in a higher transmission of SXR radiation; the transmission of 200 nm thick Ti foil (current one for imaging) and 100 nm thick Ti foil is 71 %, 84 %, respectively, for wavelength of 2.88 nm; calculation is based on [51]. However, the Ti filter with an area of 140 mm^2 without supportive mesh is very fragile. In a similar way, the specimen can be deposited on a thinner Si_3N_4 membrane; instead of a 50 nm thick silicon nitride membrane, the 30 nm thick membrane can be used, improving the transmission of the SXR radiation $\sim$10 % [51].

We would like to image an Au Siemens star as another testing pattern and a specimen prepared by the lyophilization in the near future (in progress). The next step would be imaging a wet sample and developing a pertinent preparation method (ongoing).

List of Publications

Articles in Journals

[A1] **T. Parkman**, M. Nevrkla, A. Jančárek, J. Turňová, D. Pánek, and M. Vrbová, "Table-top water-window microscope using a capillary discharge plasma source with spatial resolution 75 nm," *Applied Sciences (Switzerland)*, vol. 10, no. 18, 2020.

[A2] K. Rubešová, J. Havlíček, V. Jakeš, L. Nádherný, J. Cajzl, D. Pánek, **T. Parkman**, A. Beitlerova, R. Kučerková, F. Hájek, and M. Nikl, "Heavily Ce3+ doped $Y_3Al_5O_{12}$ thin films deposited by a polymer sol-gel method for fast scintillation detectors," *CrystEngComm*, vol. 21, no. 34, pp. 5115–5123, 2019.

[A3] J. Pejchal, J. Barta, V. Babin, A. Beitlerova, P. Prusa, R. Kucerkova, D. Panek, **T. Parkman**, C. Guguschev, L. Havlak, P. Zemenova, K. Kamada, and A. Yoshikawa, "Influence of Mg-codoping, non-stoichiometry and Ga-admixture on LuAG:Ce scintillation properties," *Optical Materials*, vol. 86, pp. 213–232, 2018.

[A4] P. Prusa, M. Kučera, V. Babin, P. Bruza, **T. Parkman**, D. Panek, A. Beitlerova, J. Mares, M. Hanus, Z. Lucenicova, M. Pokorny, and M. Nikl, "Tailoring and Optimization of LuAG:Ce Epitaxial Film Scintillation Properties by Mg Co-Doping," *Crystal Growth and Design*, vol. 18, no. 9, pp. 4998–5007, 2018.

[A5] J. Barta, V. Cuba, V. Jary, A. Beitlerova, D. Panek, **T. Parkman**, and M. Nikl, "Photoinduced Preparation of Bandgap-Engineered Garnet Powders," *IEEE Transactions on Nuclear Science*, vol. 65, no. 8, pp. 2184–2190, 2018.

[A6] P. Vrba, M. Vrbova, M. Müller, K. Mann, D. Pánek, and **T. Parkman**, "Picosecond laser krypton plasma emission in water window spectral range," *Physics of Plasmas*, vol. 24, no. 12, 2017.

[A7] P. Wachulak, A. Torrisi, M. Ayele, J. Czwartos, A. Bartnik, L. Wegrzynski, T. Fok, **T. Parkman**, S. Salačová, J. Turňová, M. Odstrčil, and H. Fiedorowicz, "Bioimaging using full field and contact EUV and SXR microscopes with

nanometer spatial resolution," *Applied Sciences (Switzerland)*, vol. 7, no. 6, 2017.

[A8] P. Prusa, M. Kucera, V. Babin, P. Bruza, D. Panek, A. Beitlerova, J. A. Mares, M. Hanus, Z. Lucenicova, M. Nikl, and **T. Parkman**, "Garnet Scintillators of Superior Timing Characteristics: Material, Engineering by Liquid Phase Epitaxy," *Advanced Optical Materials*, vol. 5, APR 2017.

[A9] A. Torrisi, P. Wachulak, L. Wegrzynski, T. Fok, A. Bartnik, **T. Parkman**, S. Vondrová, J. Turňová, B. Jankiewicz, B. Bartosewicz, and H. Fiedorowicz, "A stand-alone compact EUV microscope based on gas-puff target source," *Journal of Microscopy*, vol. 265, no. 2, pp. 251–260, 2017.

[A10] M. Nawaz, M. Nevrkla, A. Jancarek, A. Torrisi, **T. Parkman**, J. Turnova, L. Stolcova, M. Vrbova, J. Limpouch, L. Pina, and P. Wachulak, "Table-top water-window soft X-ray microscope using a Z-pinching capillary discharge source," *Journal of Instrumentation*, vol. 11, no. 7, 2016.

[A11] M. Nikl, V. Babin, J. Pejchal, V. Laguta, M. Buryi, J. Mares, K. Kamada, S. Kurosawa, A. Yoshikawa, D. Panek, **T. Parkman**, P. Bruza, K. Mann, and M. Muller, "The Stable Ce4+ Center: A New Tool to Optimize Ce-Doped Oxide Scintillators," *IEEE Transactions on Nuclear Science*, vol. 63, no. 2, pp. 433–438, 2016.

Articles in Conference Proceedings

[B12] P. Wachulak, A. Torrisi, M. Ayele, A. Bartnik, J. Czwartos, L. Wegrzynski, T. Fok, **T. Parkman**, S. Vondrová, J. Turnová, M. Odstrcil, and H. Fiedorowicz, "Soft x-ray imaging with incoherent sources," in *Proceedings of SPIE - The International Society for Optical Engineering*, vol. 10243, 2017.

[B13] L. Horáčková, **T. Parkman**, and M. Vrbová, "Characterization of a table-top "water window" soft X-ray source," in *Instruments and Methods for Biology and Medicine 2017*, pp. 45–48, Czech Technical University Publishing House, 2017.

[B14] M. Nevrkla, A. Jančárek, F. Nawaz, **T. Parkman**, and M. Vrbová, "Time-resolved EUV spectra from nitrogen Z-pinching capillary discharge," in *Proceedings of SPIE - The International Society for Optical Engineering*, vol. 9510, 2015.

Editorial Activities – Conference Proceedings

[C15] **T. Parkman** and T. Jarošíková, eds., *Instruments and Methods for Biology and Medicine 2019*, Czech Technical University Publishing House, 2019. ISBN 978-80-01-06643-0.

[C16] D. Pánek and **T. Parkman**, eds., *Instruments and Methods for Biology and Medicine 2018*, Czech Technical University Publishing House, 2018. ISBN 978-80-01-06502-0.

[C17] **T. Parkman** and K. Žambochová, eds., *Instruments and Methods for Biology and Medicine 2017*, Czech Technical University Publishing House, 2017. ISBN 978-80-01-06303-3.

Special Articles in Local Periodical – Invited

[D18] **T. Parkman** and A. Jančárek, "Mikroskop využívající měkké rentgenové záření," *Pražská Technika*, vol. 22, no. 6, 2020.

[D19] **T. Parkman**, "Mikroskopie a spektroskopie využívající SXR záření," *Pražská Technika*, vol. 21, no. 2, 2019.

Selected Presentations

Conferences, International Workshops

[E1] **T. Parkman**, M. Nevrkla, M. Nawaz, A. Jančárek, D. Pánek, J. Turňová, and M. Vrbová, "Table-Top Water-Window Microscope Using Z-Pinching Capillary Discharge Source." 2019 Source Workshop, Amsterdam, The Netherlands, Nov 4-6, 2019.

[E2] **T. Parkman**, M. Nawaz, M. Nevrkla, M. Vrbová, and A. Jančárek, "Transmission Water-Window Microscope Using Capillary Discharge Source." X-Ray Microscopy Conference 2016, Oxford, United Kingdom, Aug 15-19, 2016.

[E3] **T. Parkman**, M. Nawaz, M. Nevrkla, M. Vrbová, and A. Jančárek, "Water-Window Microscope Based on Nitrogen Plasma Capillary Discharge Source." 2015 International Workshop on EUV and Soft X-Ray Sources, Dublin, Ireland, Nov 9-11, 2015.

[E4] **T. Parkman**, J. Hübner, P. Vrba, M. Nevrkla, and A. Jančárek, "Optimization possibilities of nitrogen capillary discharge as a source of monochromatic radiation in water window region at $\lambda = 2.88$ nm." 1st International Workshop on Frontiers of X&XUV Optics and its Applications, Prague, Czech Republic, Oct 26-27, 2015.

[E5] **T. Parkman**, D. Pánek, P. Brůža, and M. Nikl, "Time-resolved soft X-ray excited luminescence spectroscopy of solids state scintillators." 1st Workshop on Application of Laser Plasma Sources of X-rays and Extreme Ultraviolet (EUV) in Technology and Science, Warsaw, Poland, July 6-9, 2015.

[E6] **T. Parkman**, S. Vondrová, M. Nevrkla, P. Brůža, and M. Vrbová, "Comparison of Laser Produced Plasma and Discharge Produced Plasma as a Source for Soft X-Ray Microscopy." 2014 International Workshop on EUV and Soft X-Ray Sources, Dublin, Ireland, Nov 3-6, 2014.

References

[1] T. G. Rochow and P. A. Tucker, *Introduction to Microscopy by Means of Light, Electrons, X Rays, or Acoustics*. Springer Science & Business Media, July 1994.

[2] William J Croft, *Under The Microscope: A Brief History Of Microscopy*. No. v. 5 in Series in Popular Science, Hackensack, NJ: World Scientific, 2006.

[3] A. Hughes, "The Father of Microscopy," *Nature*, vol. 188, pp. 812–812, Dec. 1960.

[4] "Micrographia by Robert Hooke, 1665." https://www.bl.uk/collection-items/micrographia-by-robert-hooke-1665.

[5] A. van Leeuwenhoek, *The Select Works of Antony Van Leeuwenhoek: Containing His Microscopical Discoveries in Many of the Works of Nature*. G. Sidney, 1800.

[6] B. Amos, "Lessons from the history of light microscopy," *Nature cell biology*, vol. 2, pp. E151–E152, Aug. 2000.

[7] E. Abbe, "Beiträge zur Theorie des Mikroskops und der mikroskopischen Wahrnehmung," vol. 1873, no. 9, pp. 413–468.

[8] B. R. Masters, *Superresolution Optical Microscopy: The Quest for Enhanced Resolution and Contrast*. Springer Nature, Mar. 2020.

[9] J. Hunter, "A New Method of Illumination for Photomicrography," *The Veterinary Journal and Annals of Comparative Pathology*, vol. 41, pp. 240–243, Oct. 1895.

[10] M. Saxena, G. Eluru, and S. S. Gorthi, "Structured illumination microscopy," *Advances in Optics and Photonics*, vol. 7, pp. 241–275, June 2015.

[11] F. Zernike, "Phase contrast, a new method for the microscopic observation of transparent objects," *Physica*, vol. 9, pp. 686–698, July 1942.

[12] A. Diaspro, P. Bianchini, F. Cella Zanacchi, L. Lanzanò, G. Vicidomini, M. Oneto, L. Pesce, and I. Cainero, "Fluorescence Microscopy," in *Springer*

Handbook of Microscopy (P. W. Hawkes and J. C. H. Spence, eds.), Springer Handbooks, pp. 2–2, Cham: Springer International Publishing, 2019.

[13] S. W. Hell and J. Wichmann, "Breaking the diffraction resolution limit by stimulated emission: Stimulated-emission-depletion fluorescence microscopy," *Optics Letters*, vol. 19, pp. 780–782, June 1994.

[14] S. W. Hell, "Far-Field Optical Nanoscopy," *Science*, vol. 316, pp. 1153–1158, May 2007.

[15] R. Sharma, M. Singh, and R. Sharma, "Recent advances in STED and RESOLFT super-resolution imaging techniques," *Spectrochimica Acta Part A: Molecular and Biomolecular Spectroscopy*, vol. 231, p. 117715, Apr. 2020.

[16] E. Betzig, G. Patterson, R. Sougrat, O. Lindwasser, S. Olenych, J. Bonifacino, M. Davidson, J. Lippincott-Schwartz, and H. Hess, "Imaging intracellular fluorescent proteins at nanometer resolution," *Science*, vol. 313, no. 5793, pp. 1642–1645, 2006.

[17] M. Rust, M. Bates, and X. Zhuang, "Sub-diffraction-limit imaging by stochastic optical reconstruction microscopy (STORM)," *Nature Methods*, vol. 3, no. 10, pp. 793–795, 2006.

[18] L. Cao and Z. Liu, "Introduction to the virtual special issue on super-resolution imaging techniques," *Optics Communications*, vol. 404, pp. 1–4, Dec. 2017.

[19] F. Haguenau, P. W. Hawkes, J. L. Hutchison, B. Satiat-Jeunemaitre, G. T. Simon, and D. B. Williams, "Key events in the history of electron microscopy," *Microscopy and Microanalysis*, vol. 9, pp. 96–138, Apr. 2003.

[20] X. Benjin and L. Ling, "Developments, applications, and prospects of cryo-electron microscopy," *Protein Science*, vol. 29, pp. 872–882, Apr. 2020.

[21] C. Kisielowski, B. Freitag, M. Bischoff, H. van Lin, S. Lazar, G. Knippels, P. Tiemeijer, M. van der Stam, S. von Harrach, M. Stekelenburg, M. Haider, S. Uhlemann, H. Müller, P. Hartel, B. Kabius, D. Miller, I. Petrov, E. A. Olson, T. Donchev, E. A. Kenik, A. R. Lupini, J. Bentley, S. J. Pennycook, I. M. Anderson, A. M. Minor, A. K. Schmid, T. Duden, V. Radmilovic, Q. M. Ramasse, M. Watanabe, R. Erni, E. A. Stach, P. Denes, and U. Dahmen, "Detection of single atoms and buried defects in three dimensions by aberration-corrected electron microscope with 0.5-A information limit," *Microscopy and Microanalysis: The Official Journal of Microscopy Society of America, Microbeam Analysis Society, Microscopical Society of Canada*, vol. 14, pp. 469–477, Oct. 2008.

[22] "On a New Kind of Rays," *Nature*, vol. 53, pp. 274–276, Jan. 1896.

[23] J. Kirz and C. Jacobsen, "The history and future of X-ray microscopy," *Journal of Physics: Conference Series*, vol. 186, p. 012001, Sept. 2009.

[24] B. Niemann, D. Rudolph, and G. Schmahl, "X-ray microscopy with synchrotron radiation," *Applied Optics*, vol. 15, pp. 1883–1884, Aug. 1976.

[25] H. Rarback, J. M. Kenney, J. Kirz, M. R. Howells, P. Chang, P. J. Coane, R. Feder, P. J. Houzego, D. P. Kern, and D. Sayre, "Recent Results from the Stony Brook Scanning Microscope," in *X-Ray Microscopy* (G. Schmahl and D. Rudolph, eds.), Springer Series in Optical Sciences, (Berlin, Heidelberg), pp. 203–216, Springer, 1984.

[26] W. Chao, P. Fischer, T. Tyliszczak, S. Rekawa, E. Anderson, and P. Naulleau, "Real space soft x-ray imaging at 10 nm spatial resolution," *Optics Express*, vol. 20, pp. 9777–9783, Apr. 2012.

[27] C. A. Larabell and K. A. Nugent, "Imaging cellular architecture with x-rays," *Current Opinion in Structural Biology*, vol. 20, no. 5, pp. 623 – 631, 2010.

[28] D. Attwood, *Soft X-Rays and Extreme Ultraviolet Radiation: Principles and Applications*. Cambridge University Press, 2007.

[29] G. McDermott, M. A. L. Gros, C. G. Knoechel, M. Uchida, and C. A. Larabell, "Soft x-ray tomography and cryogenic light microscopy: the cool combination in cellular imaging," *Trends in Cell Biology*, vol. 19, no. 11, pp. 587 – 595, 2009. Special Issue – Imaging Cell Biology.

[30] J. Guo and C. A. Larabell, "Soft X-ray tomography: Virtual sculptures from cell cultures," *Current Opinion in Structural Biology*, vol. 58, pp. 324–332, Oct. 2019.

[31] G. A. Johansson, A. Holmberg, H. M. Hertz, and M. Berglund, "Design and performance of a laser-plasma-based compact soft x-ray microscope," *Review of Scientific Instruments*, vol. 73, no. 3, pp. 1193–1197, 2002.

[32] H. Hertz, O. von Hofsten, M. Bertilson, U. Vogt, A. Holmberg, J. Reinspach, D. Martz, M. Selin, A. Christakou, J. Jerlström-Hultqvist, and S. Svärd, "Laboratory cryo soft x-ray microscopy," *Journal of Structural Biology*, vol. 177, no. 2, pp. 267 – 272, 2012.

[33] H. Legall, G. Blobel, H. Stiel, W. Sandner, C. Seim, P. Takman, D. H. Martz, M. Selin, U. Vogt, H. M. Hertz, D. Esser, H. Sipma, J. Luttmann, M. Höfer, H. D. Hoffmann, S. Yulin, T. Feigl, S. Rehbein, P. Guttmann, G. Schneider, U. Wiesemann, M. Wirtz, and W. Diete, "Compact x-ray microscope for the

water window based on a high brightness laser plasma source," *Opt. Express*, vol. 20, pp. 18362–18369, Jul 2012.

[34] M. Muller, T. Mey, J. Niemyer, and K. Mann, "Table-top soft x-ray microscope using laser-induced plasma from a pulsed gas jet," *Opt. Express*, vol. 22, pp. 23489–23495, Sep 2014.

[35] M. Mueller and K. Mann, "Laboratory-Scale Soft X-ray Source for Microscopy and Absorption Spectroscopy," in *Nanoscale Photonic Imaging* (T. Salditt, A. Egner, and D. R. Luke, eds.), vol. 134, pp. 549–559, Cham: Springer International Publishing Ag, 2020.

[36] P. W. Wachulak, A. Torrisi, A. Bartnik, D. Adjei, J. Kostecki, L. Wegrzynski, R. Jarocki, M. Szczurek, and H. Fiedorowicz, "Desktop water window microscope using a double-stream gas puff target source," *Applied Physics B*, vol. 118, no. 4, pp. 573–578, 2015.

[37] P. W. Wachulak, A. Torrisi, A. Bartnik, Ł. Wegrzyński, T. Fok, and H. Fiedorowicz, "A desktop extreme ultraviolet microscope based on a compact laser-plasma light source," *Applied Physics B*, vol. 123, p. 25, Dec. 2016.

[38] P. W. Wachulak, A. Torrisi, W. Krauze, A. Bartnik, J. Kostecki, M. Maisano, A. M. Sciortino, and H. Fiedorowicz, "A "water window" tomography based on a laser-plasma double-stream gas-puff target soft X-ray source," *Applied Physics B*, vol. 125, p. 70, Apr. 2019.

[39] M. Kishimoto, M. Kado, M. Ishino, S. Tamotsu, K. Yasuda, and K. Shinohara, "Development of single shot soft x-ray contact microscopy system for nanoscale dynamics measurement of living biological specimen," *AIP Conference Proceedings*, vol. 1465, no. 1, pp. 43–47, 2012.

[40] D. Schafer, M. Benk, K. Bergmann, T. Nisius, U. Wiesemann, and T. Wilhein, "Optical setup for tabletop soft x-ray microscopy using electrical discharge sources," *Journal of Physics: Conference Series*, vol. 186, no. 1, p. 012033, 2009.

[41] S. F. Horne, J. Silterra, and W. Holber, "A compact soft x-ray microscope using an electrode-less z-pinch source," *Journal of Physics: Conference Series*, vol. 186, no. 1, p. 012028, 2009.

[42] D. B. Carlson, J. Gelb, V. Palshin, and J. E. Evans, "Laboratory-based cryogenic soft x-ray tomography with correlative cryo-light and electron microscopy," *Microscopy and Microanalysis*, vol. 19, pp. 22–29, 2 2013.

[43] M. F. Nawaz, M. Nevrkla, A. Jancarek, A. Torrisi, T. Parkman, J. Turnova, L. Stolcova, M. Vrbova, J. Limpouch, L. Pina, and P. Wachulak, "Table-top water-window soft X-ray microscope using a Z-pinching capillary discharge source," *Journal of Instrumentation*, vol. 11, pp. P07002–P07002, July 2016.

[44] T. Parkman, M. Nevrkla, A. Jančárek, J. Turňová, D. Pánek, and M. Vrbová, "Table-top water-window microscope using a capillary discharge plasma source with spatial resolution 75 nm," *Applied Sciences*, vol. 10, no. 18, 2020.

[45] T. Mey, M. Rein, P. Großmann, and K. Mann, "Brilliance improvement of laser-produced soft x-ray plasma by a barrel shock," *New Journal of Physics*, vol. 14, p. 073045, July 2012.

[46] M. Kado, M. Kishimoto, K. Shinohara, and T. Ejima, "Increase of the emission of laser-produced plasmas under N2 gas atmosphere in the 2.9–6 nm region," *Applied Physics Letters*, vol. 111, p. 054102, July 2017.

[47] C. John, M. Kishimoto, T. Johzaki, T. Higashiguchi, N. Kakunaka, Y. Matsumoto, N. Hasegawa, M. Nishikino, T. Ejima, A. Sunahara, T. Endo, and S. Namba, "Enhancement of water-window soft x-ray emission from laser-produced Au plasma under low-pressure nitrogen atmosphere," *Optics Letters*, vol. 44, pp. 1439–1442, Mar. 2019.

[48] T. Helk, M. Zuerch, and C. Spielmann, "Perspective: Towards single shot time-resolved microscopy using short wavelength table-top light sources," *Structural Dynamics-Us*, vol. 6, p. 010902, Jan. 2019.

[49] S. Amelinckx, *Handbook of Microscopy: Applications.* Handbook of Microscopy: Applications in Materials Science, Solid-state Physics, and Chemistry, VCH, 1997.

[50] J. P. Langmore and M. F. Smith, "Quantitative energy-filtered electron microscopy of biological molecules in ice," *Ultramicroscopy*, vol. 46, no. 1, pp. 349 – 373, 1992.

[51] B. Henke, E. Gullikson, and J. Davis, "X-ray interactions: photoabsorption, scattering, transmission, and reflection at e=50-30000 ev, z=1-92," *Atomic Data and Nuclear Data Tables*, vol. 54, pp. 181–342, July 1993.

[52] J. Kirz, C. Jacobsen, and M. Howells, "Soft x-ray microscopes and their biological applications," *Quarterly Reviews of Biophysics*, vol. 28, no. 1, p. 33–130, 1995.

[53] M. Howells, C. Jacobsen, T. Warwick, and A. Van den Bos, "Principles and Applications of Zone Plate X-Ray Microscopes," in *Science of Microscopy*

(P. W. Hawkes and J. C. H. Spence, eds.), pp. 835–926, New York, NY: Springer, 2007.

[54] R. de L. Kronig, "On the theory of dispersion of x-rays," *J. Opt. Soc. Am.*, vol. 12, pp. 547–557, Jun 1926.

[55] M. Bertilson, *Laboratory Soft X-Ray Microscopy and Tomography*. PhD thesis, Royal Institute of Technology, Stockholm, Sweden, 2011.

[56] D. Sayre, J. Kirz, R. Feder, D. Kim, and E. Spiller, "Transmission microscopy of unmodified biological materials. comparative radiation dosages with electrons and ultrasoft x-ray photons," *Ultramicroscopy*, vol. 2, pp. 337–49, 09 1977.

[57] C. T. Chantler, "Detailed tabulation of atomic form factors, photoelectric absorption and scattering cross section, and mass attenuation coefficients in the vicinity of absorption edges in the soft x-ray (z = 30–36, z = 60–89, e = 0.1–10kev) – addressing convergence issues of earlier work," *Journal of Synchrotron Radiation*, vol. 8, no. 4, pp. 1124–1124.

[58] P. Bruza, *Pulsed Plasma Soft X-Ray Source in Biomedical Research*. PhD thesis, Czech Technical University in Prague, Kladno, Czech Republic, 2014.

[59] P. Instruments, "The absorption length for soft x-rays," 2016. [on-line] [20.1.2016] http://www.princetoninstruments.com/applications/soft-xray-microscopy.

[60] C. Nave, "A comparison of absorption and phase contrast for X-ray imaging of biological cells," *Journal of Synchrotron Radiation*, vol. 25, pp. 1490–1504, Sep 2018.

[61] A. E. Burgess, "The rose model, revisited," *J. Opt. Soc. Am. A*, vol. 16, pp. 633–646, Mar 1999.

[62] D. Sayre, J. Kirz, R. Feder, D. Kim, and E. Spiller, "Potential operating region for ultrasoft x-ray microscopy of biological materials," *Science*, vol. 196, no. 4296, pp. 1339–1340, 1977.

[63] M. Howells, T. Beetz, H. Chapman, C. Cui, J. Holton, C. Jacobsen, J. Kirz, E. Lima, S. Marchesini, H. Miao, D. Sayre, D. Shapiro, J. Spence, and D. Starodub, "An assessment of the resolution limitation due to radiation-damage in x-ray diffraction microscopy," *Journal of Electron Spectroscopy and Related Phenomena*, vol. 170, no. 1, pp. 4 – 12, 2009. Radiation Damage.

[64] G. Schneider, "Cryo x-ray microscopy with high spatial resolution in amplitude and phase contrast," *Ultramicroscopy*, vol. 75, no. 2, pp. 85 – 104, 1998.

[65] G. Schneider, B. Niemann, P. Guttmann, D. Rudolph, and G. Schmahl, "Cryo x-ray microscopy," *Synchrotron Radiation News*, vol. 8, no. 3, pp. 19–28, 1995.

[66] A. Gianoncelli, L. Vaccari, G. Kourousias, D. Cassese, D. E. Bedolla, S. Kenig, P. Storici, M. Lazzarino, and M. Kiskinova, "Soft X-Ray Microscopy Radiation Damage On Fixed Cells Investigated With Synchrotron Radiation FTIR Microscopy," *Scientific Reports*, vol. 5, May 2015.

[67] M. Kördel, M. Kördel, A. Dehlinger, A. Dehlinger, A. Dehlinger, C. Seim, C. Seim, U. Vogt, E. Fogelqvist, E. Fogelqvist, J. A. Sellberg, H. Stiel, H. Stiel, and H. M. Hertz, "Laboratory water-window x-ray microscopy," *Optica*, vol. 7, pp. 658–674, June 2020. Publisher: Optical Society of America.

[68] A. Hofmann, *The Physics of Synchrotron Radiation.* No. Vol. 20 in Cambridge Monographs on Particle Physics, Nuclear Physics, and Cosmology, Cambridge University Press, 2004.

[69] F. R. Elder, A. M. Gurewitsch, R. V. Langmuir, and H. C. Pollock, "Radiation from electrons in a synchrotron," *Phys. Rev.*, vol. 71, pp. 829–830, Jun 1947.

[70] I. H. Munro, "Synchrotron Radiation Research in the UK," *Journal of Synchrotron Radiation*, vol. 4, pp. 344–358, Nov 1997.

[71] E. Duke, K. Dent, M. Razi, and L. M. Collinson, "Biological applications of cryo-soft x-ray tomography," *Journal of Microscopy*, vol. 255, no. 2, pp. 65–70, 2014.

[72] J. M. J. Madey, "Stimulated emission of bremsstrahlung in a periodic magnetic field," *Journal of Applied Physics*, vol. 42, no. 5, pp. 1906–1913, 1971.

[73] D. A. G. Deacon, L. R. Elias, J. M. J. Madey, G. J. Ramian, H. A. Schwettman, and T. I. Smith, "First operation of a free-electron laser," *Phys. Rev. Lett.*, vol. 38, pp. 892–894, Apr 1977.

[74] W. Ackermann, G. Asova, V. Ayvazyan, A. Azima, N. Baboi, J. Bähr, V. Balandin, B. Beutner, A. Brandt, A. Bolzmann, R. Brinkmann, O. I. Brovko, M. Castellano, P. Castro, L. Catani, E. Chiadroni, S. Choroba, A. Cianchi, J. T. Costello, D. Cubaynes, J. Dardis, W. Decking, H. Delsim-Hashemi, A. Delserieys, G. Di Pirro, M. Dohlus, S. Düsterer, A. Eckhardt, H. T. Edwards, B. Faatz, J. Feldhaus, K. Flöttmann, J. Frisch, L. Fröhlich, T. Garvey, U. Gensch, C. Gerth, M. Görler, N. Golubeva, H.-J. Grabosch, M. Grecki, O. Grimm, K. Hacker, U. Hahn, J. H. Han, K. Honkavaara, T. Hott, M. Hüning, Y. Ivanisenko, E. Jaeschke, W. Jalmuzna, T. Jezynski, R. Kammering, V. Katalev, K. Kavanagh, E. T. Kennedy, S. Khodyachykh, K. Klose, V. Kocharyan, M. Körfer, M. Kollewe, W. Koprek, S. Korepanov, D. Kostin,

M. Krassilnikov, G. Kube, M. Kuhlmann, C. L. S. Lewis, L. Lilje, T. Limberg, D. Lipka, F. Löhl, H. Luna, M. Luong, M. Martins, M. Meyer, P. Michelato, V. Miltchev, W. D. Möller, L. Monaco, W. F. O. Müller, O. Napieralski, O. Napoly, P. Nicolosi, D. Nölle, T. Nuñez, A. Oppelt, C. Pagani, R. Paparella, N. Pchalek, J. Pedregosa-Gutierrez, B. Petersen, B. Petrosyan, G. Petrosyan, L. Petrosyan, J. Pflüger, E. Plönjes, L. Poletto, K. Pozniak, E. Prat, D. Proch, P. Pucyk, P. Radcliffe, H. Redlin, K. Rehlich, M. Richter, M. Roehrs, J. Roensch, R. Romaniuk, M. Ross, J. Rossbach, V. Rybnikov, M. Sachwitz, E. L. Saldin, W. Sandner, H. Schlarb, B. Schmidt, M. Schmitz, P. Schmüser, J. R. Schneider, E. A. Schneidmiller, S. Schnepp, S. Schreiber, M. Seidel, D. Sertore, A. V. Shabunov, C. Simon, S. Simrock, E. Sombrowski, A. A. Sorokin, P. Spanknebel, R. Spesyvtsev, L. Staykov, B. Steffen, F. Stephan, F. Stulle, H. Thom, K. Tiedtke, M. Tischer, S. Toleikis, R. Treusch, D. Trines, I. Tsakov, E. Vogel, T. Weiland, H. Weise, M. Wellhöfer, M. Wendt, I. Will, A. Winter, K. Wittenburg, W. Wurth, P. Yeates, M. V. Yurkov, I. Zagorodnov, and K. Zapfe, "Operation of a free-electron laser from the extreme ultraviolet to the water window," *Nature Photonics*, vol. 1, pp. 336–342, June 2007. Number: 6 Publisher: Nature Publishing Group.

[75] E. Allaria, R. Appio, L. Badano, W. A. Barletta, S. Bassanese, S. G. Biedron, A. Borga, E. Busetto, D. Castronovo, P. Cinquegrana, S. Cleva, D. Cocco, M. Cornacchia, P. Craievich, I. Cudin, G. D'Auria, M. Dal Forno, M. B. Danailov, R. De Monte, G. De Ninno, P. Delgiusto, A. Demidovich, S. Di Mitri, B. Diviacco, A. Fabris, R. Fabris, W. Fawley, M. Ferianis, E. Ferrari, S. Ferry, L. Froehlich, P. Furlan, G. Gaio, F. Gelmetti, L. Giannessi, M. Giannini, R. Gobessi, R. Ivanov, E. Karantzoulis, M. Lonza, A. Lutman, B. Mahieu, M. Milloch, S. V. Milton, M. Musardo, I. Nikolov, S. Noe, F. Parmigiani, G. Penco, M. Petronio, L. Pivetta, M. Predonzani, F. Rossi, L. Rumiz, A. Salom, C. Scafuri, C. Serpico, P. Sigalotti, S. Spampinati, C. Spezzani, M. Svandrlik, C. Svetina, S. Tazzari, M. Trovo, R. Umer, A. Vascotto, M. Veronese, R. Visintini, M. Zaccaria, D. Zangrando, and M. Zangrando, "Highly coherent and stable pulses from the FERMI seeded free-electron laser in the extreme ultraviolet," *Nature Photonics*, vol. 6, pp. 699–704, Oct. 2012. Number: 10 Publisher: Nature Publishing Group.

[76] International Atomic Energy Agency, "Synchrotrons." [on-line] Available: https://www.iaea.org/topics/nuclear-science/nuclear-research/accelerators/synchrotrons [2020, April 5], 2016.

[77] D. Philip, *Synchrotron Radiation : Production and Properties*. No. Vol. 3 in Oxford Science Publications, OUP Oxford, 2000.

[78] U. Bergmann, V. Yachandra, and J. Yano, eds., *X-Ray Free Electron Lasers*. Energy and Environment Series, The Royal Society of Chemistry, 2017.

[79] G. Geloni, Z. Huang, and C. Pellegrini, "Chapter 1 the physics and status of x-ray free-electron lasers," in *X-Ray Free Electron Lasers: Applications in Materials, Chemistry and Biology*, pp. 1–44, The Royal Society of Chemistry, 2017.

[80] S. Carbajo, "Single-shot flash imaging using a compact soft x-ray microscope," Master's thesis, Colorado State University, 2012.

[81] D. W. Workie, "Basic physical processes and principles of free electron lasers (fels)." [online], November 2001.

[82] Z. Huang and K.-J. Kim, "Review of x-ray free-electron laser theory," *Phys. Rev. ST Accel. Beams*, vol. 10, p. 034801, Mar 2007.

[83] Z. Huang, "Brightness and Coherence of Synchrotron Radiation and FELs," in *4th International Particle Accelerator Conference*, p. MOYCB101, 2013.

[84] M. Hoshino and S. Aoki, "Laser plasma soft x-ray microscope with wolter mirrors for observation of biological specimens in air," *Japanese Journal of Applied Physics*, vol. 45, pp. 989–994, feb 2006.

[85] J. Sheil, P. Dunne, T. Higashiguchi, D. Kos, E. Long, T. Miyazaki, F. O'Reilly, G. O'Sullivan, P. Sheridan, C. Suzuki, E. Sokell, E. White, and D. Kilbane, "Analysis of soft x-ray emission spectra of laser-produced dysprosium, erbium and thulium plasmas," *Journal of Physics B: Atomic, Molecular and Optical Physics*, vol. 50, p. 065006, mar 2017.

[86] A. G. Michette, I. C. E. Turcu, M. S. Schulz, M. T. Browne, G. R. Morrison, P. Fluck, C. J. Buckley, and G. F. Foster, "Scanning x-ray microscopy using a laser-plasma source," *Review of Scientific Instruments*, vol. 64, no. 6, pp. 1478–1482, 1993.

[87] K. W. Kim, Y. Kwon, K.-Y. Nam, J.-H. Lim, K.-G. Kim, K. S. Chon, B. H. Kim, D. E. Kim, J. Kim, B. N. Ahn, H. J. Shin, S. Rah, K.-H. Kim, J. S. Chae, D. G. Gweon, D. W. Kang, S. H. Kang, J. Y. Min, K.-S. Choi, S. E. Yoon, E.-A. Kim, Y. Namba, and K.-H. Yoon, "Compact soft x-ray transmission microscopy with sub-50 nm spatial resolution," *Physics in Medicine and Biology*, vol. 51, pp. N99–N107, feb 2006.

[88] P. Wachulak, A. Bartnik, H. Fiedorowicz, P. Rudawski, R. Jarocki, J. Kostecki, and M. Szczurek, ""water window" compact, table-top laser plasma soft x-ray sources based on a gas puff target," *Nuclear Instruments and Methods*

in Physics Research Section B: Beam Interactions with Materials and Atoms, vol. 268, no. 10, pp. 1692 – 1700, 2010.

[89] A. Bayer, F. Barkusky, S. Döring, P. Großmann, and K. Mann, "Applications of compact laser-driven euv/xuv plasma sources," *X-Ray Optics and Instrumentation*, vol. 2010, 05 2009.

[90] P. Brůža, V. Fidler, and M. Nikl, "Table-top instrumentation for time-resolved luminescence spectroscopy of solids excited by nanosecond pulse of soft x-ray source and/or UV laser," *Journal of Instrumentation*, vol. 6, pp. P09007–P09007, sep 2011.

[91] M. Muller, F.-C. Kuhl, P. Grossmann, P. Vrba, and K. Mann, "Emission properties of ns and ps laser-induced soft x-ray sources using pulsed gas jets," *Opt. Express*, vol. 21, pp. 12831–12842, May 2013.

[92] D. Attwood and A. Sakdinawat, *Physics of Hot Dense Plasmas*, p. 315–402. Cambridge University Press, 2 ed., 2017.

[93] R. Fabbro, J. Fournier, P. Ballard, D. Devaux, and J. Virmont, "Physical study of laser-produced plasma in confined geometry," *Journal of Applied Physics*, vol. 68, pp. 775–784, July 1990.

[94] P. Vrba, M. Vrbova, S. Zakharov, V. Zakharov, A. Jancarek, and M. Nevrkla, "Nitrogen capillary plasma as a source of intense monochromatic radiation at 2.88 nm," *Journal of Electron Spectroscopy and Related Phenomena*, vol. 196, 10 2014.

[95] M. Kado, M. Kishimoto, S. Tamotsu, K. Yasuda, and K. Shinohara, "In situ observation of cellular organelles with a contact x-ray microscope," *Journal of Physics: Conference Series*, vol. 463, no. 1, p. 012056, 2013.

[96] E. Fogelqvist, M. Kördel, M. Selin, and H. M. Hertz, "Stability of liquid-nitrogen-jet laser-plasma targets," *Journal of Applied Physics*, vol. 118, no. 17, p. 174902, 2015.

[97] J. Rocca, V. Shlyaptsev, F. Tomasel, O. Cortázar, D. Hartshorn, and J. Chilla, "Demonstration of a discharge pumped table-top soft-x-ray laser," *Physical review letters*, vol. 73, pp. 2192–2195, 11 1994.

[98] K. Powell, G. Duffy, P. Choi, R. Aliaga-Rossel, O. Benali, H. Keles, B. Lebert, O. Sarroukh, L. Tantart, C. Zaepffel, and A. Michette, "The development of a tabletop soft x-ray in vitromicroscope," *AIP Conference Proceedings*, vol. 1365, no. 1, pp. 128–131, 2011.

[99] E. Wyndham, M. Favre, M. Valdivia, and J. Valenzuela, "Considerations of a high repitition capillary discharge operated in nitrogen as a water-window x-ray microscope source," in *Pulsed Power Conference, 2009. PPC '09. IEEE*, pp. 688–692, June 2009.

[100] P. Vrba, S. Zakharov, A. Jancarek, M. Vrbova, M. Nevrkla, and P. Kolar, "Pinching capillary discharge as a water window radiation source," *Journal of Electron Spectroscopy and Related Phenomena*, vol. 184, no. 3–6, pp. 335 – 337, 2011.

[101] K. Bergmann, F. Küpper, and M. Benk, "Soft x-ray emission from a pulsed gas discharge in a pseudosparklike electrode geometry," *Journal of Applied Physics*, vol. 103, no. 12, p. 123304, 2008.

[102] S. Ohsuka, A. Ohba, S. Onoda, K. Nakamoto, T. Nakano, M. Miyoshi, K. Soda, and T. Hamakubo, "Laboratory-size three-dimensional x-ray microscope with wolter type i mirror optics and an electron-impact water window x-ray source," *Review of Scientific Instruments*, vol. 85, no. 9, p. 093701, 2014.

[103] P. Skoglund, U. Lundström, U. Vogt, P. Takman, and H. M. Hertz, "Electron-impact water-jet microfocus source for water-window microscopy," *AIP Conference Proceedings*, vol. 1365, no. 1, pp. 152–155, 2011.

[104] P. Skoglund, U. Lundström, U. Vogt, and H. M. Hertz, "High-brightness water-window electron-impact liquid-jet microfocus source," *Applied Physics Letters*, vol. 96, no. 8, p. 084103, 2010.

[105] A. G. Michette, "Applications of Soft X-Ray Focusing Systems," in *Optical Systems for Soft X Rays* (A. G. Michette, ed.), pp. 243–282, Boston, MA: Springer US, 1986.

[106] E. Spiller, *Soft X-Ray Optics*. 1000 20th Street, Bellingham, WA 98227-0010 USA: SPIE, Aug. 1994.

[107] M. Born, E. Wolf, A. B. Bhatia, P. C. Clemmow, D. Gabor, A. R. Stokes, A. M. Taylor, P. A. Wayman, and W. L. Wilcock, *Principles of Optics: Electromagnetic Theory of Propagation, Interference and Diffraction of Light*. Cambridge University Press, 7 ed., 1999.

[108] P. Wachulak, A. Torrisi, M. F. Nawaz, A. Bartnik, D. Adjei, S. Vondrova, J. Turnova, A. Jancarek, J. Limpouch, M. Vrbova, and H. Fiedorowicz, "A compact "water window" microscope with 60 nm spatial resolution for applications in biology and nanotechnology," *Microscopy and Microanalysis*, vol. 21, pp. 1214–1223, Oct 2015.

[109] M. F. Nawaz, A. Jancarek, M. Nevrkla, P. Wachulak, J. Limpouch, and L. Pina, "Focusing and photon flux measurements of the 2.88-nm radiation at the sample plane of the soft x-ray microscope, based on capillary discharge source," vol. 9510, pp. 951014–951014–7, 2015.

[110] P. Kirkpatrick and A. V. Beaz, "Formation of optical images by x-rays," *J. Optical Soc. Am.*, vol. 38, pp. 766–774, 1948.

[111] P. W. Wachulak, A. Bartnik, L. Wegrzynski, J. Kostecki, R. Jarocki, T. Fok, M. Szczurek, and H. Fiedorowicz, "Sub 1-um resolution "water-window" microscopy using a compact, laser-plasma {SXR} source based on a double stream gas-puff target," *Nuclear Instruments and Methods in Physics Research Section B: Beam Interactions with Materials and Atoms*, vol. 311, pp. 42 – 46, 2013.

[112] *X-ray data booklet.* Lawrence Berkeley National Laboratory, University of California, October 2009.

[113] M. M. Barysheva, A. E. Pestov, N. N. Salashchenko, M. N. Toropov, and N. I. Chkhalo, "Precision imaging multilayer optics for soft x-rays and extreme ultraviolet bands," *Physics-Uspekhi*, vol. 55, pp. 681–699, jul 2012.

[114] S. Bajt, J. B. Alameda, T. W. B. Jr., W. M. Clift, J. A. Folta, B. B. Kaufmann, and E. A. Spiller, "Improved reflectance and stability of Mo/Si multilayers," in *Soft X-Ray and EUV Imaging Systems II* (D. A. Tichenor and J. A. Folta, eds.), vol. 4506, pp. 65 – 75, International Society for Optics and Photonics, SPIE, 2001.

[115] M. Bibishkin, Y. A. Vainer, A. Pestov, K. Prokhorov, N. Salashchenko, A. Fraerman, and N. Chkhalo, "Investigation of characteristics of multilayer x-ray mirrors with ultrashort periods d= 0.7-2.4 nm," *Bulletin of the Russian Academy of Sciences: Physics*, vol. 69, no. 2, pp. 217–225, 2005.

[116] T. Kuhlmann, S. Yulin, T. Feigl, N. Kaiser, T. Gorelik, U. Kaiser, and W. Richter, "Chromium–scandium multilayer mirrors for the nitrogen k α line in the water window region," *Appl. Opt.*, vol. 41, pp. 2048–2052, Apr 2002.

[117] I. A. Artyukov, Y. Bugayev, O. Y. Devizenko, R. M. Feschenko, Y. S. Kasyanov, V. V. Kondratenko, S. A. Romanova, S. V. Saveliev, F. Schäfers, T. Feigl, *et al.*, "Carbon window soft x-ray imaging using multilayer optics," in *Soft X-Ray Lasers and Applications VI*, vol. 5919, p. 59190E, International Society for Optics and Photonics, 2005.

[118] S. Andreev, A. Akhsakhalyan, M. Bibishkin, N. Chkhalo, S. Gaponov, S. Gusev, E. Kluenkov, K. Prokhorov, N. Salashchenko, F. Schafers, *et al.*, "Multilayer optics for xuv spectral region: technology fabrication and applications," *Central European Journal of Physics*, vol. 1, no. 1, pp. 191–209, 2003.

[119] E. Fogelqvist, M. Kördel, V. Carannante, B. Önfelt, and H. M. Hertz, "Laboratory cryo x-ray microscopy for 3D cell imaging," *Scientific Reports*, vol. 7, p. 13433, Oct. 2017.

[120] A. Dehlinger, J. Braenzel, D. Groetzsch, T. Feigl, R. Jung, B. KanngieBer, S. Rehbein, C. Seim, and H. Stiel, "Towards high performance soft x-ray cryotomography in the laboratory," *Microscopy and Microanalysis*, vol. 24, no. S2, p. 248–249, 2018.

[121] H. Schnopper, L. Speybroeck, J. Delvaille, A. Epstein, E. Rachlew, R. Bachrach, J. Dijkstra, and L. Lantward, "Diffraction grating transmission efficiencies for xuv and soft x rays," *Applied Optics*, vol. 16, 05 1977.

[122] C. Jacobsen, M. Howells, and T. Warwick, "Zone-Plate X-Ray Microscopy," in *Springer Handbook of Microscopy* (P. W. Hawkes and J. C. H. Spence, eds.), Springer Handbooks, pp. 1145–1204, Cham: Springer International Publishing, 2019.

[123] A. Ekman, V. Weinhardt, J.-H. Chen, G. McDermott, M. A. Le Gros, and C. Larabell, "Psf correction in soft x-ray tomography," *Journal of Structural Biology*, vol. 204, no. 1, pp. 9 – 18, 2018.

[124] P. A. C. Takman, H. Stollberg, G. A. Johansson, A. Holmberg, M. Lindblom, and H. M. Hertz, "High-resolution compact x-ray microscopy," *Journal of Microscopy*, vol. 226, no. 2, pp. 175–181, 2007.

[125] O. von Hofsten, M. Bertilson, J. Reinspach, A. Holmberg, H. M. Hertz, and U. Vogt, "Sub-25-nm laboratory x-ray microscopy using a compound fresnel zone plate," *Opt. Lett.*, vol. 34, pp. 2631–2633, Sep 2009.

[126] J.-F. Adam, J.-P. Moy, and J. Susini, "Table-top water window transmission x-ray microscopy: Review of the key issues, and conceptual design of an instrument for biology," *Review of Scientific Instruments*, vol. 76, no. 9, p. 091301, 2005.

[127] A. G. Michette, C. J. Buckley, S. J. Pfauntsch, N. R. Arnot, J. Wilkinson, Z. Wang, N. I. Khaleque, and G. S. Dermody, "The king's college laboratory scanning x-ray microscope," *AIP Conference Proceedings*, vol. 507, no. 1, pp. 420–423, 2000.

[128] E. Spiller, R. Feder, J. Topalian, D. Eastman, W. Gudat, and D. Sayre, "X-ray microscopy of biological objects with carbon kappa and with synchrotron radiation," *Science*, vol. 191, pp. 1172–1174, Mar. 1976.

[129] M. G. Ayele, P. W. Wachulak, J. Czwartos, D. Adjei, A. Bartnik, Ł. Wegrzynski, M. Szczurek, L. Pina, and H. Fiedorowicz, "Development and characterization of a laser-plasma soft X-ray source for contact microscopy," *Nuclear Instruments and Methods in Physics Research Section B: Beam Interactions with Materials and Atoms*, vol. 411, pp. 35–43, Nov. 2017.

[130] P. Wachulak, A. Torrisi, M. Ayele, J. Czwartos, A. Bartnik, Ł. Wegrzyński, T. Fok, T. Parkman, Š. Salačová, J. Turňová, M. Odstrčil, and H. Fiedorowicz, "Bioimaging Using Full Field and Contact EUV and SXR Microscopes with Nanometer Spatial Resolution," *Applied Sciences*, vol. 7, p. 548, June 2017.

[131] T. Ejima, M. Kado, M. Aoyama, K. Yasuda, and S. Tamotsu, "Organelle Distribution in a Hydrated Bio-cell by Correlation between Soft X-ray and Fluorescence Images," *Journal of Physics: Conference Series*, vol. 849, p. 012009, June 2017.

[132] S. Perrin and P. Montgomery, "Fourier optics: basic concepts," June 2018.

[133] J. W. Goodman, *Introduction to Fourier Optics*. New York : W.H. Freeman, Macmillan Learning, 2017.

[134] C. Jacobsen, *Imaging Physics*, p. 71–198. Advances in Microscopy and Microanalysis, Cambridge University Press, 2019.

[135] O. von Hofsten, P. A. Takman, and U. Vogt, "Simulation of partially coherent image formation in a compact soft X-ray microscope," *Ultramicroscopy*, vol. 107, no. 8, pp. 604–609, 2007.

[136] M. Bertilson, O. von Hofsten, H. M. Hertz, and U. Vogt, "Numerical model for tomographic image formation in transmission x-ray microscopy," *Opt. Express*, vol. 19, pp. 11578–11583, Jun 2011.

[137] M. Selin, E. Fogelqvist, A. Holmberg, P. Guttmann, U. Vogt, and H. M. Hertz, "3d simulation of the image formation in soft x-ray microscopes," *Opt. Express*, vol. 22, pp. 30756–30768, Dec 2014.

[138] H. Rarback, D. Shu, S. C. Feng, H. Ade, J. Kirz, I. McNulty, D. P. Kern, T. H. P. Chang, Y. Vladimirsky, N. Iskander, D. Attwood, K. McQuaid, and S. Rothman, "Scanning x-ray microscope with 75-nm resolution," *Review of Scientific Instruments*, vol. 59, no. 1, pp. 52–59, 1988.

[139] A. Sakdinawat and D. Attwood, "Nanoscale x-ray imaging," *Nature Photonics*, vol. 4, pp. 840–848, Nov 2010.

[140] S. Vitta, "Soft x-ray microscope: A new biological tool," *Current Science*, 1997.

[141] C. Jacobsen, "Soft x-ray microscopy," *Trends in Cell Biology*, vol. 9, no. 2, pp. 44 – 47, 1999.

[142] V. Cardin, B. E. Schimdt, N. Thiré, S. Beaulieu, V. Wanie, M. Negro, C. Vozzi, V. Tosa, and F. Légaré, "Self-channelled high harmonic generation of water window soft x-rays," *Journal of Physics B: Atomic, Molecular and Optical Physics*, vol. 51, p. 174004, aug 2018.

[143] G. J. Stein, P. D. Keathley, P. Krogen, H. Liang, J. P. Siqueira, C.-L. Chang, C.-J. Lai, K.-H. Hong, G. M. Laurent, and F. X. Kärtner, "Water-window soft x-ray high-harmonic generation up to the nitrogen k-edge driven by a kHz, 2.1m OPCPA source," *Journal of Physics B: Atomic, Molecular and Optical Physics*, vol. 49, p. 155601, jul 2016.

[144] Y. Fu, K. Nishimura, R. Shao, A. Suda, K. Midorikawa, P. Lan, and E. J. Takahashi, "High efficiency ultrafast water-window harmonic generation for single-shot soft X-ray spectroscopy," *Communications Physics*, vol. 3, pp. 1–10, May 2020.

[145] J. E. Evans, P. Blackborow, S. F. Horne, and J. Gelb, "Affordable x-ray microscopy with nanoscale resolution," *Bio Optics World*, 2013.

[146] A. Dehlinger, C. Seim, H. Stiel, S. Twamley, A. Ludwig, M. Kördel, D. Grötzsch, S. Rehbein, and B. Kanngießer, "Laboratory soft x-ray microscopy with an integrated visible-light microscope—correlative workflow for faster 3d cell imaging," *Microscopy and Microanalysis*, vol. 26, no. 6, p. 1124–1132, 2020.

[147] M. Harkiolaki, M. C. Darrow, M. C. Spink, E. Kosior, K. Dent, and E. Duke, "Cryo-soft X-ray tomography: Using soft X-rays to explore the ultrastructure of whole cells," *Emerging Topics in Life Sciences*, vol. 2, pp. 81–92, Mar. 2018.

[148] M. Do, S. A. Isaacson, G. McDermott, M. A. L. Gros, and C. A. Larabell, "Imaging and characterizing cells using tomography," *Archives of Biochemistry and Biophysics*, vol. 581, pp. 111 – 121, 2015.

[149] C. Seim, K. Reineke, S. Werner, A. Dehlinger, H. Legall, H. Stiel, and B. Kanngießer, "High pressure treated bacillus subtilis spores — structural analysis by means of synchrotron and laboratory based soft x-ray microscopy," *Innovative Food Science and Emerging Technologies*, vol. 29, pp. 134 – 142, 2015.

[150] D. H. Martz, M. Selin, O. von Hofsten, E. Fogelqvist, A. Holmberg, U. Vogt, H. Legall, G. Blobel, C. Seim, H. Stiel, and H. M. Hertz, "High average brightness water window source for short-exposure cryomicroscopy," *Opt. Lett.*, vol. 37, pp. 4425–4427, Nov 2012.

[151] M. Kördel, E. Fogelqvist, V. Carannante, B. Önfelt, H. Reddy, M. Svenda, J. Sellberg, K. Arsana, U. Vogt, and H. Hertz, "Biological laboratory x-ray microscopy," vol. 11112, 2019.

[152] P. W. Wachulak, A. Bartnik, H. Fiedorowicz, D. Panek, and P. Bruza, "Imaging of nanostructures with sub-100 nm spatial resolution using a desktop euv microscope," *Applied Physics B*, vol. 109, no. 1, pp. 105–111, 2012.

[153] A. Torrisi, P. W. Wachulak, A. Bartnik, u. Wegrzyński, T. Fok, and H. Fiedorowicz, "Biological applications of short wavelength microscopy based on compact, laser-produced gas-puff plasma source," *Applied Sciences*, vol. 10, no. 23, 2020.

[154] M. Müller and K. Mann, "Laboratory-scale soft x-ray source for microscopy and absorption spectroscopy," in *Nanoscale Photonic Imaging* (T. Salditt, A. Egner, and D. R. Luke, eds.), pp. 549–559, Cham: Springer International Publishing, 2020.

[155] M. P. Valdivia, E. S. Wyndham, E. Ramos-Moore, P. Ferrari, and M. Favre, "Observations of soft x-ray emission and wall ablation in a fast low-energy pulsed capillary discharge," *Journal of Physics D: Applied Physics*, vol. 46, no. 31, p. 315201, 2013.

[156] M. P. Valdivia, J. C. Valenzuela, E. S. Wyndham, M. Favre, H. Chuaqui, and H. Bhuyan, "Soft x-ray emission analysis of a pulsed capillary discharge operated in nitrogen," *Journal of Physics: Conference Series*, vol. 511, no. 1, p. 012022, 2014.

[157] M. Benk, K. Bergmann, A. Q. Fernandez, S. Srivastava, N. A. Kotov, D. Schaefer, and T. Wilhein, "Soft x-ray microscopic investigation on self assembling nanocrystals," *AIP Conference Proceedings*, vol. 1365, no. 1, pp. 433–436, 2011.

[158] M. Nevrkla, J. Novak, A. Jancarek, P. Vrba, and M. Vrbova, "Characterization of capillary discharge water-window radiation source," in *2012 Inetrnational Workwhop on EUV and Soft X-Ray Sources*, Oct 2012.

[159] T. Parkman, S. Vondrova, M. Nevrkla, P. Bruza, and M. Vrbova, "Comparison of laser produced plasma and discharge produced plasma as a source for soft

x-ray microscopy," in *2014 Inetrnational Workshop on EUV and Soft X-Ray Sources*, Nov 2014.

[160] N. Firouzi Farrashbandi and M. Eslami-Kalantari, "Inverse bremsstrahlung absorption in laser-fusion plasma," *Journal of Theoretical and Applied Physics*, vol. 14, no. 3, pp. 261–264, 2020.

[161] M. Nevrkla, P. Kolar, P. Prsanec, M. Tamas, A. Jancarek, P. Vrba, M. Vrbova, and J. Novak, "Capillary discharge water-window radiation spectra measurement," tech. rep., Prague, 2009. Project.

[162] A. Kramida, Yu. Ralchenko, J. Reader, and and NIST ASD Team. NIST Atomic Spectra Database (ver. 5.8), [Online]. Available: `https://physics.nist.gov/asd` [2020, October 28]. National Institute of Standards and Technology, Gaithersburg, MD., 2020.

[163] M. Nevrkla, A. Jančárek, F. Nawaz, T. Parkman, and M. Vrbová, "Time-resolved euv spectra from nitrogen z-pinching capillary discharge," in *Proceedings of SPIE - The International Society for Optical Engineering*, vol. 9510, 2015.

[164] J. Novak, M. Nevrkla, A. Jancarek, M. Vrbova, and P. Vrba, "Measurement of spectra in "water-window" wavelength region," in *2012 Inetrnational Workwhop on EUV and Soft X-Ray Sources*, Oct 2012.

[165] T. Parkman, "Optimization of capillary discharge as XUV radiation source," Master's thesis, Czech Technical University in Prague, 2013.

[166] M. F. Nawaz, *Laboratory soft X-ray microscope based on incoherent capillary discharge source*. PhD thesis, Czech Technical University in Prague, Prague, Czech Republic, 2016.

[167] J. Thong, K. Sim, and J. Phang, "Single-image signal-to-noise ratio estimation," *Scanning*, vol. 23, no. 5, pp. 328–336, 2001.

[168] A. Torrisi, P. Wachulak, M. Nawaz, A. Bartnik, L. Wegrzynski, A. Jancarek, and H. Fiedorowicz, "Characterization and optimization of images acquired by a compact soft x-ray microscope based on a double stream gas-puff target source," *Journal of Instrumentation*, vol. 11, no. 4, 2016.